Standard Model Higgs boson analysis via associated top production and hadronic decay using the ATLAS detector at the CERN LHC

Christian Alexander Shaw

Department of Physics and Astronomy
University of Glasgow

Thesis submitted for the degree of
Doctor of Philosophy

June 2007

Abstract

A search for the Higgs boson using the ATLAS detector at the Large Hadron Collider is outlined. The channel is associated Higgs boson production $t\bar{t}H$ and subsequent decay via $H \rightarrow b\bar{b}$ for a Higgs mass of 110 - 130 GeV. The major backgrounds $t\bar{t}b\bar{b}$ and $t\bar{t}jj$ are simulated with matrix element generators, at leading order and next to leading order respectively. A cuts based analysis is used to maximise significance, however K-factors are not used. A comparison is also made between results from the cone (with radius 0.4) and k_T (with R parameter 0.45) jet reconstruction algorithms. For the cone algorithm, significances of 2.4, 1.5 and 1.0 were found for Higgs masses 110, 120 and 130 GeV, respectively. For the k_T algorithm, significances of 2.4, 1.6 and 1.1 were found for Higgs masses 110, 120 and 130 GeV, respectively. The quoted significances are for an integrated luminosity of 30 fb^{-1}.

Acknowledgements

There are many people who I'd like to thank for their help throughout my PhD. Firstly my supervisor Prof. David Saxon who initially offered me my place and whose advice and positivity have been immensely helpful over the years. My second supervisor Dr. Richard Bates also ablely took over the responsibility for my general development, whilst I was on attachment at CERN. Particular praise is reserved for those who adopted the supervisory role on the analysis front; Dr. John Kennedy who introduced me to the Higgs 'bug' and Dr. Christopher Collins-Tooth who went well beyond that which his job required in assisting me. Without his encouragement and patience over the last few years, this work would never have been completed.

I'd like to thank PPARC, firstly for granting the studentship itself and then for their support of my LTA at CERN. The 18 months I spent in Geneva were invaluable professionally - I think the proximity to experts in your field and just the overall academic atmosphere of CERN were key in my work. From a personal point of view I enjoyed my time in Switzerland and would thank the UK Liaison office for making the students' lives so easy.

There are of course numerous others who have helped me both at CERN and within the department but any list would be too short or exhaustive! I hope they know who they are and that I appreciate all their efforts.

Author's Declaration

This thesis represents work performed from 2002 - 2007 in the Experimental Particle Physics group in the Department of Physics and Astronomy at the University of Glasgow. The software described in Chapter 5 is developed by the ATLAS software community, of which I was generally a user with some development work. The EventView framework was conceived by A.Farbin (with later development by ATLAS devlopers), which I privately extended for the purpose of my analysis. The analysis and results presented in Chapter 6 are my own work.

Contents

List of Figures

List of Tables

Chapter 1

Introduction

The Standard Model of particle physics has proved to be one of the most accurate and successful theories ever devised in terms of experimental agreement with theoretical predictions. One component of the Standard Model is a field which interacts with other Standard Model fields, resulting in some of the particles acquiring mass. This field is known as the Higgs field and has an associated observable particle, the Higgs boson. This particle is the only constituent particle in the Standard Model which has yet to be observed, but unfortunately its mass is not predicted. Theoretical and experimental constraints have narrowed the region for this mass to between 114.4 and several hundred GeV/c^2. This thesis describes a search channel using the ATLAS detector at the Large Hadron Collider (LHC), which is currently under construction at CERN and is expected to start taking data in 2008.

ATLAS is a general purpose physics detector, one of four detectors (CMS, LHCb and ALICE being the others) on the LHC accelerator ring. The LHC is primarily a proton-proton collider with beams of energy 7 TeV and centre-of-mass energy 14 TeV. Within the lower constraints of the mass region, one of the most promising search channels is $t\bar{t}H$ because it has a reasonable cross-section, but also a sufficiently distinct final state that can be differentiated from large QCD backgrounds. For a Higgs mass below 130 GeV/c^2 the dominant decay mode is $H \rightarrow b\bar{b}$, therefore this is the final

state searched for in this work. Below is a breakdown of the content of this thesis.

Chapter 2 introduces the Standard Model as a gauge theory and the Higgs mechanism for electro-weak symmetry breaking. Then the properties of Standard Model Higgs boson are described together with the theoretical and experimental constraints currently placed on the Higgs boson mass. Some discussion is also made of the Supersymmetric extension to the Standard Model. Chapter 3 describes the Large Hadron Collider, the detectors due to run on the accelerator ring and the physics motivation for its construction. Chapter 4 describes the ATLAS detector starting from the co-ordinate system, then each of the detector sections, before an outline of the data acquisition and trigger system.

Chapter 5 details the ATLAS software environment for Monte-Carlo event simulation, reconstruction and analysis. Additionally, a description is made of the two jet reconstruction algorithms, cone and k_T. Chapter 6 is the analysis chapter. Firstly it describes the Monte Carlo data samples for the signal and major backgrounds and the properties of the final state particles therein. A step by step reconstruction of the signal hard process is detailed, at each stage attempting to maximise acceptance. As the final step, the Higgs boson candidates are reconstructed and the significance for 30 fb^{-1} calculated. A comparison is also made between results from the cone and k_T jet reconstruction algorithms. At the end of the chapter discussion of systematic errors is made and a comparison with the results from other similar studies. Chapter 7 is a conclusion of the work presented, with reference to how the channel might be improved in the future.

Chapter 2

The Standard Model

2.1 Standard Model Particles and Interactions

The Standard Model (SM) [1–5] is the name given to the theory describing our current understanding of fundamental particles and their interactions. Of the four fundamental forces of nature, (electromagnetism, weak interactions, strong interactions and gravity), three are described by the Standard Model. Quantum Electro-Dynamics (QED) is the oldest and describes electromagnetic interactions and later was unified with the weak nuclear force in the electroweak theory. Quantum Chromo-Dynamics (QCD) is the theory of the strong nuclear force, whilst the final force, gravity, has no clear (quantum) model as yet. Within the Standard Model there are two types of fundamental (which is to say point-like and indivisible) particles: fermions and bosons. Fermions have $\frac{1}{2}$ integer spin and comprise the matter in the universe. Bosons have integer spin and are responsible for interactions between particles, being mediators of the forces. The fermions are further split into two families: quarks and leptons. Quarks are found naturally in the protons and neutrons and carry charges associated with all the fundamental forces. Leptons, on the other hand, do not carry any colour charge which means they are not affected by the strong nuclear force. The quarks and leptons are grouped into families, of which three have been identified. In

actuality lower limits are placed on the masses of any fourth generation within the Standard Model and Z-boson decay measurements at LEP [6, 7] indicate there must be exactly three. The groupings and general properties of these particles is shown in table. 2.1 (properties taken from Particle Data Group review 2006, see [8]). It is only the first generation which comprises ordinary matter (i.e. valence quarks), whilst the second and third generations are generally only produced in accelerator experiments and high energy cosmic events and decay rapidly.

Generation	Name	Mass	Charge
First	up quark (u)	1.5 - 3.0 MeV	$\frac{2}{3}e$
	down quark (d)	3 - 7 MeV	$-\frac{1}{3}e$
	electron (e)	≈ 0.511 MeV	$-e$
	electron neutrino (ν_e)	< 2 eV at 95% CL	0
Second	charm quark (c)	1.25 ± 0.09 GeV	$\frac{2}{3}e$
	strange quark (s)	95 ± 25 MeV	$-\frac{1}{3}e$
	muon (μ)	≈ 105.698 MeV	$-e$
	muon neutrino (ν_μ)	< 0.19 MeV at 90% CL	0
Third	top quark (t)	174.2 ± 3.3 GeV	$\frac{2}{3}e$
	bottom quark (b)	4.2 ± 0.07 GeV	$-\frac{1}{3}e$
	tau (τ)	$1776.99^{+0.29}_{-0.26}$ MeV	$-e$
	tau neutrino (ν_τ)	< 18.2 MeV at 95% CL	0

Table 2.1: *Properties of the fundamental spin-$\frac{1}{2}$ fermions. Values are taken from Particle Data Group review 2006.*

As mentioned above, bosons are the carriers of the fundamental forces. The photon is the massless particle exchanged in electromagnetism and is of course observed on a daily basis. The heavy W and Z^0 gauge bosons carry the weak charge, though due to their large mass they are short-ranged. The W is responsible, for example,

for β-decay whilst the Z^0 interferes with the photon resulting in parity violation in atoms. In QCD, the mediating particle is called the gluon and is responsible for colour exchange between quarks. Like the photon it is massless; however like quarks they are only seen confined in bound states (called hadrons) in nature because the strong force increases with distance. The properties of these bosons, together with the hypothesised gravitation force carrier, the graviton, and the as yet unobserved Higgs boson are described in table. 2.2

Force	Name	Mass	Charge	Spin
electromagnetism	photon (γ)	$< 6 \times 10^{-17}$ eV	0	1
weak nuclear	W-boson	80.403 ± 0.029 GeV	± 1	1
	Z-boson	91.1876 ± 0.0021 GeV	0	1
strong nuclear	gluon (g)	0	0	1
gravity	graviton (G)	0	0	2
	Higgs boson (H)	$114.4 < m_H < 200$ GeV	0	0

Table 2.2: *Properties of the fundamental integer spin bosons*

2.2 Gauge Theories

The Standard Model is a *gauge theory*; this is to say that the Lagrangian of the theory is locally as well as globally invariant. The Lagrangian describes the equations of motion of a system and invariance of this under local transformations gives rise to conserved quantities. It is also a quantised theory in that the mechanics of quantum theory can be used to create commutation relationships for continuous fields. The SM is actually comprised of three separate quantum field theories, one for each of the fundamental forces (except gravity). The first of these formulated was QED, where initially one writes the Lagrangian of a spin-$\frac{1}{2}$ (fermion) field ψ:

$$Ł = \bar{\psi}(i\gamma^{\mu}\partial_{\mu} - m)\psi \tag{2.1}$$

under the U(1) phase transformation of the fermion field of the form:

$$\psi \rightarrow e^{iw}\psi \tag{2.2}$$

the Lagrangian density is unchanged because the conjugate $\bar{\psi}$ transforms as

$$\bar{\psi} \rightarrow e^{-iw}\bar{\psi} \tag{2.3}$$

However, if one allows the parameter w to vary in space-time such that $w \rightarrow w(x)$ i.e. local transformations, one discovers that the Lagrangian density is no longer unchanged. This is because the partial derivative in Eqn. 2.1 will act on the $w(x)$ term. To remedy this a term corresponding to a vector field A_{μ} is assumed to interact with the fermion field so that a term is added to the Lagrangian

$$Ł = \bar{\psi}(i\gamma^{\mu}(\partial_{\mu} + ieA_{\mu}) - m)\psi \tag{2.4}$$

This new term cancels out the change in the Lagrangian density introduced to allow space-time dependence, restoring invariance. One can understand this new field A_{μ} in physical terms as the photon field and e as the electrical charge of the fermion. One also adds a kinetic term for A_{μ} corresponding to the field strength, written as $F_{\mu\nu}$ which is also invariant under gauge transformations. The final Lagrangian is

$$Ł_{QED} = \bar{\psi}(i\gamma^{\mu}(\partial_{\mu} + ieA_{\mu}) - m)\psi - \frac{1}{4}F_{\mu\nu}F^{\mu\nu} \tag{2.5}$$

In order to extend this theory to non-Abelian gauge theories i.e. where group elements do not commute, it is convenient to define the covariant derivative as

$$D_{\mu} = \partial_{\mu} + ieA_{\mu} \tag{2.6}$$

and rewrite the Lagrangian as

$$Ł_{QED} = \bar{\psi}(i\gamma^\mu D_\mu - m)\psi - \frac{1}{4}F_{\mu\nu}F^{\mu\nu} \tag{2.7}$$

If one now considers an isodoublet undergoing an isospin transformation, which form the group SU(2), the Lagrangian density can be written as

$$Ł = \bar{\psi}^i(i\gamma^\mu \partial_\mu - m)\psi_i \tag{2.8}$$

The isospin transformation for ψ_i is written as

$$\psi_i \rightarrow (e^{iw^a T^a})^j_i \psi_j \tag{2.9}$$

where $a = 1 \ldots 3$ because three parameters are required for a general isospin transformation (as there are three independent generators in SU(2)). Here the generators, T^a are the Pauli spin matrices. Again if one wishes to allow space-time dependence such that $w^a \rightarrow w^a(x)$ one finds that the Lagrangian is no longer invariant. This is remedied by adding three vector boson fields A^a_μ one for each degree of freedom, with which the fermion isodoublet is then assumed to interact

$$Ł = \bar{\psi}^i(i\gamma^\mu D_\mu - mI)^j_i \psi_j \tag{2.10}$$

where the partial derivative is replaced by a covariant derivative, which is now a 2×2 matrix

$$D_\mu = \partial_\mu I + ig\,T^a A^a_\mu \tag{2.11}$$

again a kinetic term is added of the form

$$-\frac{1}{4}F^a_{\mu\nu}F^{a\ \mu\nu} \tag{2.12}$$

with one difference to the Abelian case being that cross terms appear in the derivative, indicating that the new vector boson fields are self-interacting. Using the above as a foundation, efforts were made to combine the electromagnetic and weak sectors into a single electroweak model known as the Glashow-Weinberg-Salam (GWS) model [1–3].

2.3 GWS Model

Immediate problems arise when trying to combine $U(1)_{EM}$ and SU(2) because neutrinos have no electric charge and none of the field components can be identified with the photon. When unifying the groups SU(2) $\otimes$ U(1), a different Abelian group is used with corresponding boson B_μ. Mixing of the two groups leads to the $W^\pm$, Z^0 and γ observed experimentally. At this time a new quantum number, weak hypercharge, Y, is postulated, which relates to electric charge via

$$Q = Y + I_W^3 \tag{2.13}$$

where I_W^3 is the third component of weak isospin. The covariant derivative of a weak (left-handed) isodoublet is now

$$D_\mu = \partial_\mu + ig\,T^a W_\mu^a + ig_W \tan\theta_W Y B_\mu \tag{2.14}$$

where the three vector boson fields are now represented by W_μ^a. Note that this allows a (left-handed) neutral neutrino to interact with the B_μ field even though it does not interact with photons. For an isosinglet (such as the right-handed component of the electron) the derivative is

$$D_\mu = \partial_\mu + ig_W \tan\theta_W Y B_\mu \tag{2.15}$$

which simply means they do not interact weakly. The term $\tan\theta_W$ refers to the weak mixing angle, which is a measure of the relative strengths of the SU(2) gauge coupling g_W and U(1) coupling $g_W^{'}$

$$g_W^{'} = g_W \tan\theta_W \tag{2.16}$$

the charged bosons are identified as

$$W_\mu^\pm = \frac{1}{\sqrt{2}}(W_\mu^1 \pm iW_\mu^2) \tag{2.17}$$

and the Z^0 and photon arise from

$$\begin{pmatrix} Z_\mu \\ A_\mu \end{pmatrix} = \begin{pmatrix} \cos\theta_W & -\sin\theta_W \\ \sin\theta_W & \cos\theta_W \end{pmatrix} \begin{pmatrix} W_\mu^3 \\ B_\mu \end{pmatrix} \tag{2.18}$$

Although this now describes a locally invariant field theory with the appropriate force-mediating particles, there are obvious omissions. Firstly there are no mass terms for fermions within the unified theory, because of the different behaviour of the right and left-handed components. Additionally none of the gauge bosons is predicted to be massive, which, while correct for the photon is known to be false for the carriers of the weak charge. If one tries to introduce mass terms explicitly, the Lagrangian will no longer be invariant and the the theory will no longer be renormalizable. To solve this problem a new scalar doublet field was postulated, which would preserve invariance in SU(2) $\otimes$ U(1) at some scale, but give mass at some lower energy. This process is called spontaneous symmetry breaking.

2.4 The Higgs Mechanism

Spontaneous symmetry breaking [9, 10] occurs when the Lagrangian of a system is invariant under the symmetry group, but the ground state (or vacuum) breaks the symmetry. To achieve this one introduces a complex scalar field. The field will be required to couple to the gauge fields, so must have non-zero weak hypercharge and isospin. However the electric charge must be zero to preserve $U(1)_{EM}$. Additionally there must be enough degrees of freedom to give mass naturally to the fermions and gauge bosons. A simple representation of this field is

$$\Phi = \begin{pmatrix} \Phi^+ \\ \Phi^0 \end{pmatrix} = \begin{pmatrix} \Phi_3 + i\Phi_4 \\ \Phi_1 + i\Phi_2 \end{pmatrix} \tag{2.19}$$

with Y = 1 and $I_W = \frac{1}{2}$. The Lagrangian of this field is

$$Ł = \partial_\mu \Phi^* \partial^\mu \Phi - V(\Phi) \tag{2.20}$$

$V(\Phi)$ is a potential defined by

$$V(\Phi) = -\mu^2 \Phi^* \Phi + \lambda |\Phi^* \Phi|^2 \tag{2.21}$$

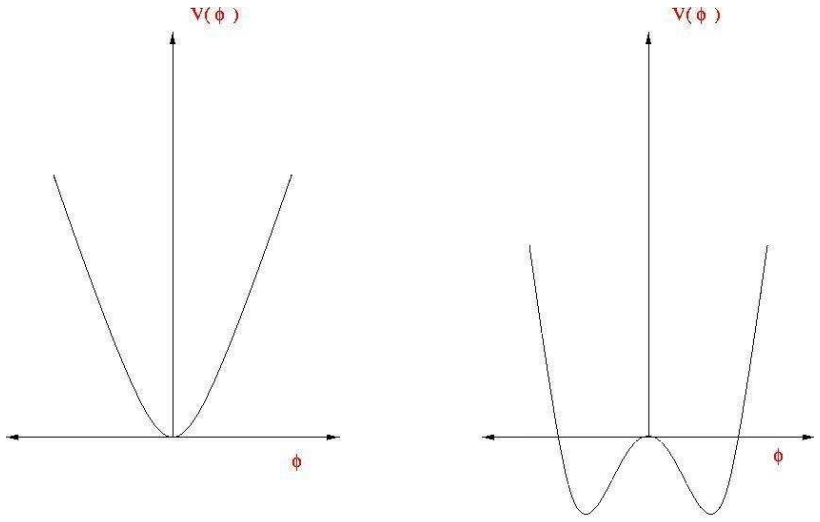

Figure 2.1: *2D representation for the complex scalar potential, for a zero (left-hand side) and non-zero (right-hand side) vacuum expectation value.*

There are two possiblilites for the values of μ^2 and λ. For λ, the value must always be positive or the potential will be unbounded. For a negative μ^2 (corresponding to an overall positive first term in the potential), the potential minimum will uniquely be at 0. This is known as the vacuum and such a solution is said to have zero vacuum expectation value (*vev*). If however μ^2 is positive, (corresponding to an overall negative first term in the potential) the solution is not at zero and is also no longer unique. The solution for the location of the minimum, Φ^{min}, is now satisfied by

$$\Phi^{min} = e^{i\theta}\sqrt{\frac{-\mu^2}{2\lambda}} \tag{2.22}$$

where $0 \leq \theta \leq 2\pi$, see fig. 2.1. One sees the *vev* has an infinite number of degenerate states so convention defines the vacuum at $\theta = 0$. It is this choice which 'breaks' the symmetry.

$$\Phi^{vac} = \sqrt{\frac{-\mu^2}{2\lambda}} = \frac{v}{\sqrt{2}} \tag{2.23}$$

However one consequence of this is that there are 'excitations' which are degenerate with the vacuum. The only way to add zero energy is to introduce additional fields with zero expectation value.

$$\Phi = \frac{1}{\sqrt{2}}(\frac{\mu}{\sqrt{\lambda}} + H + i\phi) \tag{2.24}$$

If one inserts Eqn. 2.24 into Eqn. 2.21 one now gets

$$V(\Phi) = \mu^2 H + \mu\sqrt{\lambda}(H^3 + \phi^2 H) + \frac{\lambda}{4}(H^4 + \phi^4 + 2H^2\phi^2) + \frac{\mu^4}{4\lambda} \tag{2.25}$$

The key points of Eqn. 2.25 are that the first term means the field H has a massive boson associated with it, whilst ϕ has no mass term and is associated with a massless particle called a *Goldstone boson*. Unfortunately, because choosing the vacuum is equivalent to choosing a gauge, these Goldstone bosons introduce a problem as they allow one to move into other gauges. This is unphysical, but fortunately there is a solution. This comes from the fact that a massless boson has two degrees of freedom whereas a massive boson has three. The interaction of the field Φ with the gauge bosons of SU(2) $\otimes$ U(1) not only gives them mass, but also provides the extra degree of freedom needed, via the Goldstone boson (this is said to be 'eaten' by the gauge boson).

If one rewrites the Lagrangian as

$$\mathrm{L} = |D\Phi|^2 - V(\Phi) - \frac{1}{4}F^a_{\mu\nu}F^{a\ \mu\nu} \tag{2.26}$$

where D is now the covariant derivative given in Eqn. 2.14 and the usual interaction has been added. Expansion of the $|D\Phi|^2$ produces many terms, some of which are quadratic in W_μ corresponding to mass terms. For the fermion masses, one must add terms to the Lagrangian 'by hand' vis Yukawa couplings, λ_f, to the Higgs boson. The masses of the fundamental particles are propotional to the *vev* of the Higgs field:

$$\begin{aligned} m_{W^\pm} &= v\frac{g}{2} \\ m_{Z^0} &= v\frac{\sqrt{g^2+g'^2}}{2} \\ m_f &= v\frac{\lambda_f}{\sqrt{2}} \\ m_{H^0} &= v\sqrt{2\lambda} = \sqrt{2}\mu \end{aligned} \tag{2.27}$$

where g and $g^{'}$ are the gauge couplings and λ_f are the couplings of the fermions to the Higgs boson. The *vev* is related to Fermi's constant:

$$\frac{G_F}{\sqrt{2}} = \frac{1}{2v^2} \rightarrow v = (\sqrt{2}G_F)^{\frac{-1}{2}} \approx 246 \text{ GeV} \tag{2.28}$$

The Higgs mechanism thus provides a satisfactory method of providing mass for the gauge bosons and fundamental fermions. The Higgs boson arises as a natural consequence of the mechanism and in fact all its properties are predicted except for its mass. In the next section, the expected properties and constraints on the mass are discussed.

2.5 Higgs Boson Physics

2.5.1 Higgs Boson Decays

At first order the decay width from the Higgs boson to a pair of fermions is given by

$$\Gamma(H^0 \rightarrow \bar{f}f) = \frac{N_C G_F}{4\pi\sqrt{2}} m_f^2 m_{H^0} \beta_f^3 \tag{2.29}$$

where N_C is a colour factor which is 1 for leptons and 3 for quarks and $\beta_f^3 = \sqrt{1 - \frac{4m_f^2}{m_{H^0}^2}}$ (there are higher order corrections to this [11]). One sees this favours higher fermion masses, assuming the Higgs boson is of greater mass than the fermions (necessary to be kinematically possible anyway). For the weak gauge bosons the decay width is given by

$$\Gamma(H^0 \to VV) = \delta_V \frac{G_F}{16\sqrt{2}\pi} m_{H^0}^3 (1 - 4x + 12x^2)\beta_V \tag{2.30}$$

where $x = \frac{m_V^2}{m_{H^0}^2}$, $\delta_V = 2$ for W-bosons and 1 for the Z^0 and β_V is a phase space term. For photons and gluons decays occur via heavy quark or W loops and for $m_{H^0} << m_{top}$, the partial decay width is approximately

$$\begin{aligned} \Gamma(H^0 \to gg) &= \frac{G_F}{16\sqrt{2}\pi} m_{H^0}^3 (1 + (\frac{95}{4} - \frac{7N_f}{6})\frac{\alpha_s}{\pi}) \\ \Gamma(H^0 \to \gamma\gamma) &= \frac{G_F}{128\sqrt{2}\pi^3} m_{H^0}^3 |\frac{4}{3} N_C e_t^2 - 7|^2 \end{aligned} \tag{2.31}$$

For masses over 200 GeV/c^2, the total Higgs boson width is given by [12]

$$\Gamma(H_{total}^0) = \frac{3G_F}{16\pi\sqrt{2}} m_{H^o}^3 \approx 0.5 TeV^{-2} m_{H^0}^3 \tag{2.32}$$

One can see for a Higgs mass of around 1.4 TeV the width would equal the mass. Even for a mass of few hundred GeV/c^2 the width can be over 10 GeV/c^2. For lower masses (less than 140 GeV/c^2), the formula above would indicate width of around 0.5 GeV/c^2. In fact at this scale fermion decays dominate and the width is only about 10 MeV. If one looks at these these decay widths in terms of branching ratios (see fig. 2.2), one sees that for low mass Higgs boson ($m_{H^0} < 130$ GeV/c^2) not only is $\bar{b}b$ the dominant fermionic decay channel, it is by far the most dominant channel of all at low masses. The decay fraction to $\bar{b}b$ is nearly 90% until 100 GeV/c^2 where it falls gradually, then steeply above 130 GeV/c^2. An order of magnitude lower than this is $\tau^+\tau^-$ which tails off in a similar manner. gg decay is the next most probable in this region, though as this is a difficult signature, of more interest is $\gamma\gamma$. Once their

decay processes become kinematically possible, the (initially off-shell) gauge bosons become the dominant decays. Obviously this occurs first for the W-boson and this crosses over $\bar{b}b$ to become the most probable decay at around 140 GeV/c^2. However, even though the W is always dominant over the Z^0, the latter is the one preferred in analyses in the higher mass region, as it provides a very clean signature.

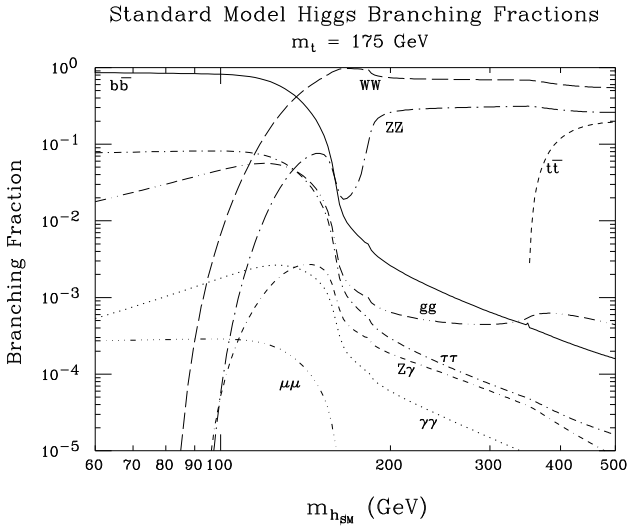

Figure 2.2: *Branching ratio of the Standard Model Higgs boson over a range of possible Higgs masses (figure from [13]).*

2.5.2 Higgs Mass Constraints

2.5.2.1 Unitarity

One motivation for introducing a new scalar field as a mechanism for introducing mass, is to deal with divergences in W-boson scattering at high energies [14]. If the W-boson were massless, the s-wave scattering amplitude summation converges, however introducing mass means they are divergent. The Higgs boson introduces higher order correction loops which may remove the divergence, but only for certain values of Higgs mass. The relevant amplitude calculation gives

$$m_{H^0}^2 \leq \frac{2\pi\sqrt{2}}{G_F} (\approx (850 \text{ GeV/c}^2)^2) \tag{2.33}$$

2.5.2.2 Triviality and Vacuum Stability

Triviality [15] applies an upper limit on the Higgs mass, by requiring that the Higgs boson self coupling does not reach a *Landau pole*. The energy dependence of the self coupling λ is approximately

$$\lambda(Q^2) = \frac{\lambda(v^2)}{1 - \frac{3\lambda(v^2)}{8\pi^2} ln \frac{Q^2}{v^2}} \tag{2.34}$$

as $\lambda(v^2) = m_{H^0}^2/v^2$ one sees a pole is approached as the mass increases and one would need to set $\lambda v = 0$ (implying a non-interacting theory). However if we assume that at some energy scale $Q = \Lambda$, new physics will become apparent, we can set requirements so that the Standard Model as presented is valid until this scale is reached. Therefore

$$m_{H^0}^2 \leq \frac{8\pi v^2}{3 ln \frac{\Lambda^2}{v^2}} \tag{2.35}$$

Eqn. 2.35 depends to some extent on the top mass, because of loop corrections, and on other higher order corrections. However, it provides the upper limit in fig. 2.3.

A lower bound can also be set, again varying depending on the scale of Λ. For small values of the self coupling, λ, the large t-quark Yukawa coupling would yield negative vacuum values and the Higgs potential would not be stable [16]. Thus a further constraint is placed on Eqn. 2.34 (via the Higgs mass) that $\lambda(Q^2) > 0$ for all Q up to the scale of new physics. The combination of these two bounds provides a band of possible Higgs mass values, which narrows as the new physics scale increases (see fig. 2.3).

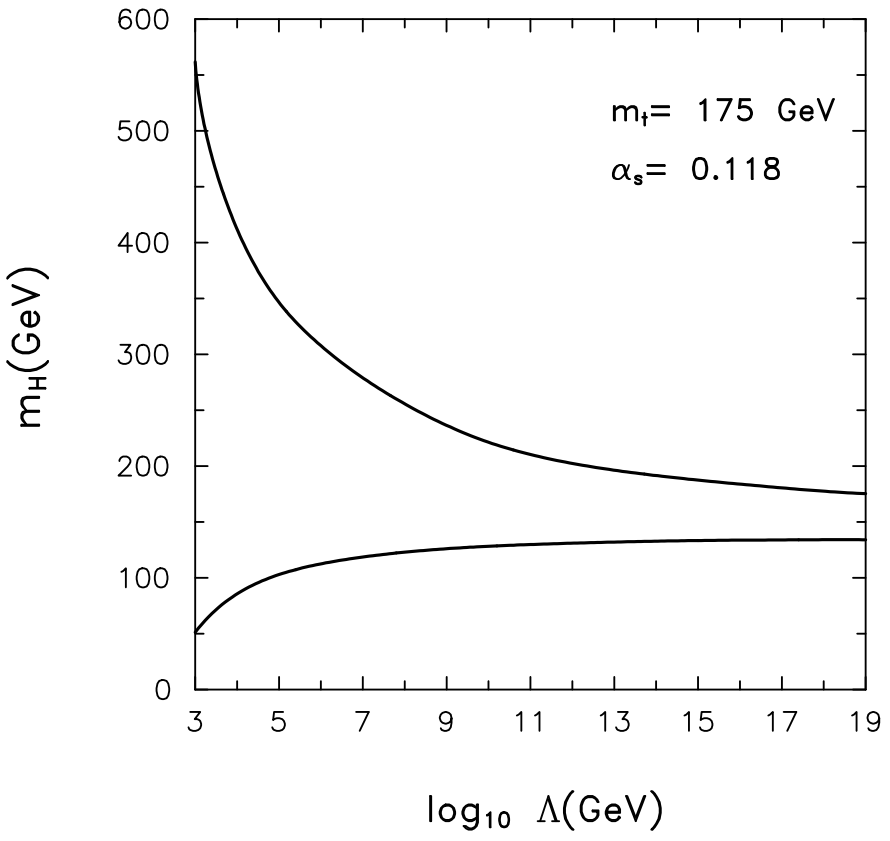

Figure 2.3: *Constraints on the Higgs mass from triviality (upper) and vacuum stability (lower), over a range of possible energies at which 'new physics' will become apparent (figure from [13]).*

2.5.3 Precision Measurements

Although theoretical constraints placed initial bounds on the Higgs mass, recently tighter constraints have come from experimental results. Indirect measurements come from precise electroweak measurements which rely on the radiative corrections which must be made to various quantities. Because many of these quantities (e.g. m_W, m_Z) are experimentally very well determined, one might have thought this would place tight bounds on the mass. Unfortunately the dependence is only logarithmic (or is gauge coupling supressed) due to SU(2) symmetries known as Veltman's screening theorem [17] and predictions have large errors on them. m_{H^0} is also highly sensitive

to the t-quark mass, which is not known to such a degree of accuracy as other values, but is continually improved upon. The best values for m_W and m_t to date (June 2007) come from the Tevatron Run II data. These are $m_W = 80413 \pm 34(stat) \pm 34(sys)$ MeV/c^2 [18] and $m_t = 170.9 \pm 1.8$ GeV/c^2 [19]. When these new values are used, much tighter constraints are set on the Higgs mass than were set by the LEP experiments (see fig. 2.4). One sees from the left hand plot that very tight upper bounds have now been placed on the mass. The right hand plot shows the difference from minimum best fit chi squared for all the electroweak data and the conclusion is that the most probable value for the Higgs mass is 80^{+36}_{-26} GeV/c^2. Shown also in the right hand plot is the region excluded by direct searches at LEP (see §2.5.4), which have excluded any mass below 114.4 GeV/c^2 with 95% CL (hence the reason this number is used as a reference in the indirect search plots). In fact the latest precision data only just borders this region at the 1σ level such that the probability of m_{H^0} being greater than 114.4 GeV/c^2 is only 19% and $m_{H^0} < 156$ GeV/c^2 at 95% CL [20].

2.5.4 Direct Searches

As mentioned in the previous section, direct searches have been made for the Higgs boson at previous experiments and as of June 2007 the best constraint comes from LEP. The result is $m_{H^0} > 114.4$ GeV/c^2 at 95% CL [22]. In fact the ALEPH experiment observed evidence at nearly 3σ level for a Higgs boson with mass 115 GeV/c^2 [23], though this was not seen by all the LEP experiments. LEP had a centre of mass energy of slightly over 200 GeV/c^2, but as it was an electron-positron collider all this energy was available for possible Higgs boson production processes. Obviously direct production i.e. $e^+e^- \rightarrow h^0$ would be possible at energies below this maximum (assuming the Higgs mass is indeed smaller than 200 GeV/c^2). However, because the coupling of fermions to the Higgs boson is proportional to the fermion's mass squared, the cross-section for the above process is very small. Instead, associated production or

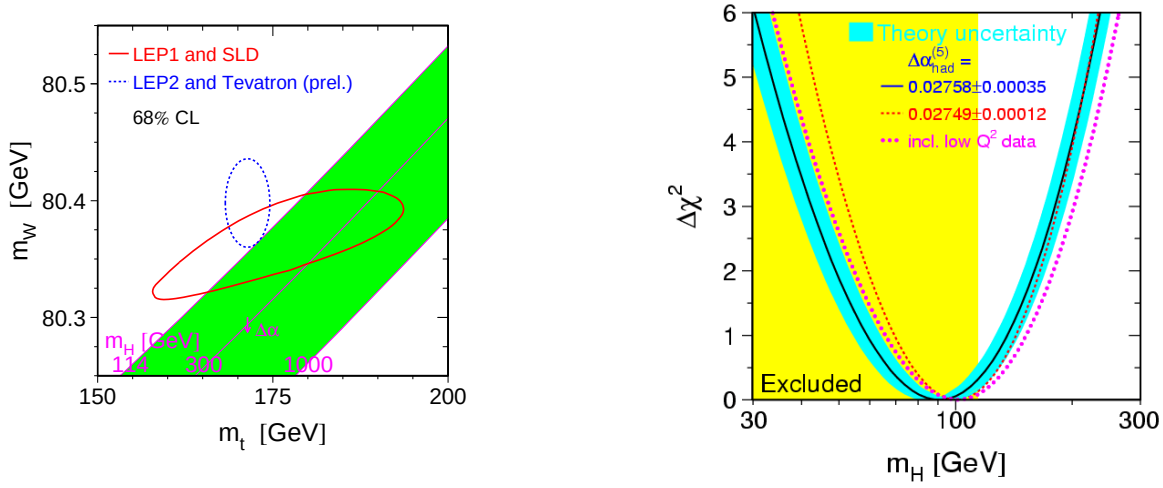

Figure 2.4: *Constraints on the SM Higgs mass based on latest (March 2007) measurements of the top mass and precision electroweak measurements [21]. Shown on the left is the* 1σ *region compatible with the new* m_t *and* m_W *compared to that previously possible. On the right is the* $\Delta\chi^2$ *for the precision electroweak measurements, showing the most probable mass (the region excluded by direct LEP searches is also shown).*

'Higgsstrahlung' is a more viable search channel. Here a Z^0 gauge boson is produced and the Higgs boson is then radiated from this. All the decay modes of the bosons are typically analysed, with the 'interesting' events which were observed, occurring in the channel where the Z radiates the Higgs boson and four jets result from the subsequent decays.

At hadron colliders the situation is somewhat different. The situation is 'messier' because a) one does not know the exact parton energies creating the hard event (parton distribution) b) there are remnants of the broken hadrons constituting an underlying event and pile-up when (for example) more than one collision is observed in the same bunch crossing. At the Tevatron experiment, with centre-of-mass energy 1.96 TeV, the Higgs boson production cross-section is shown in fig. 2.5. Because of large cross-section QCD backgrounds, it is very difficult to look for the most obvious signature of $gg \rightarrow H \rightarrow \bar{b}b$ in the lower mass region. Therefore searches at the

Tevatron concentrate on the associated production channels WH and ZH and, where kinematically allowed, the gluon fusion process with vector boson decays $gg \to H \to W^+W^-$. As of Summer 2006, the Tevatron had produced enough data ($\leq 1\text{fb}^{-1}$) to come within an order of magnitude of excluding the entire region from $100 - 200$ GeV/c^2 at 95 % CL (see fig. 2.6). The sensitivity is best in the higher mass region $130 \leq m_{H^0} \leq 170$ GeV/c^2 where the accumulated luminosity is within a factor of 4 of that required (for 95 % CL exclusion). By 2008 enough data should be accumulated to make this exclusion (or alternatively observe deviations which would hint at a Higgs boson in this region). However, the low mass region is more difficult and at best the Tevatron could expect to see 3σ evidence for a 115 GeV/c^2 Higgs mass by 2009.

The LHC is a proton-proton collider with a centre of mass of 14 TeV, many times that of the Tevatron. Therefore whilst the broad situation is somewhat similar to the Tevatron, cross-sections will be much higher (see lower fig. 2.5). However, two additional production mechanisms will become viable. Vector Boson Fusion (VBF), where two gauge bosons are radiated and annihilate to form the Higgs boson, will be the second most dominant production mechanism. Typically then one looks for decays to τ pairs or WW^*, depending on the mass range (the obvious $H \to \bar{b}b$ is again swamped by background). Of interest in the low mass region is the $\bar{t}tH$ channel, where one can look for the favoured $H \to \bar{b}b$ decay because of the other components expected in the decay. Out of favour are the associated production modes WH and ZH, because their final states are not complex enough to be seen over the massive W+X and Z+X backgrounds. One final interesting channel in the low mass region is $gg \to H \to \gamma\gamma$ because, although the branching ratio for $H \to \gamma\gamma$ is very small, the large cross-section makes it viable if one has good knowledge of the background. The LHC is expected to begin operation in 2008 and after 3 complete years of data taking should have 30 fb^{-1} of data. At this point the ATLAS experiment expects to be able to claim discovery across the entire (non-excluded) mass range, see fig. 2.7. However

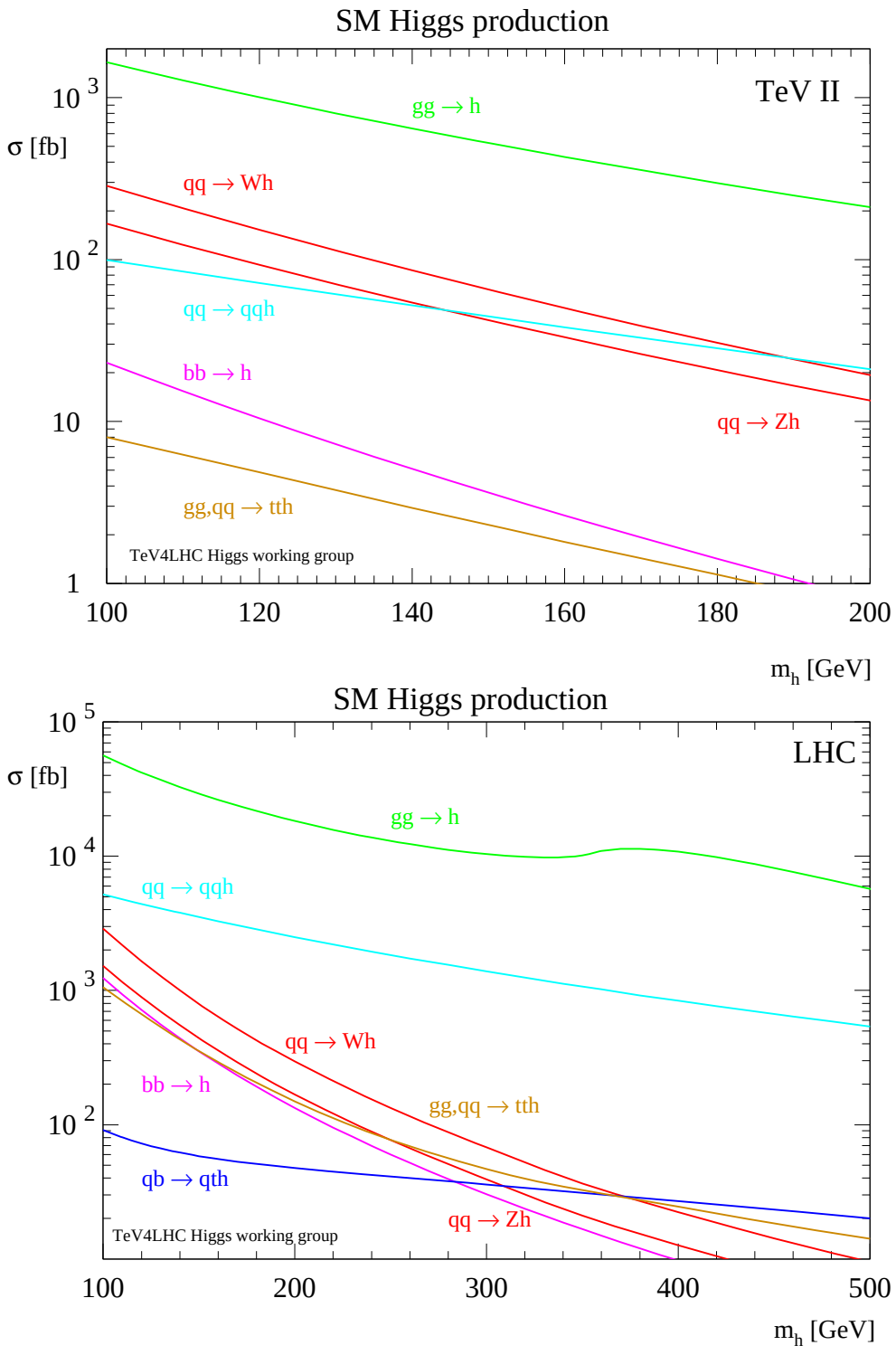

Figure 2.5: *SM Higgs boson production cross sections over a range of masses at the Tevatron and LHC [24].*

one sees that low mass region is the most difficult, which is exactly the region the recent indirect searches have pointed to. In this region it will be necessary to add the significance of independent channels and optimising each channel is even more important.

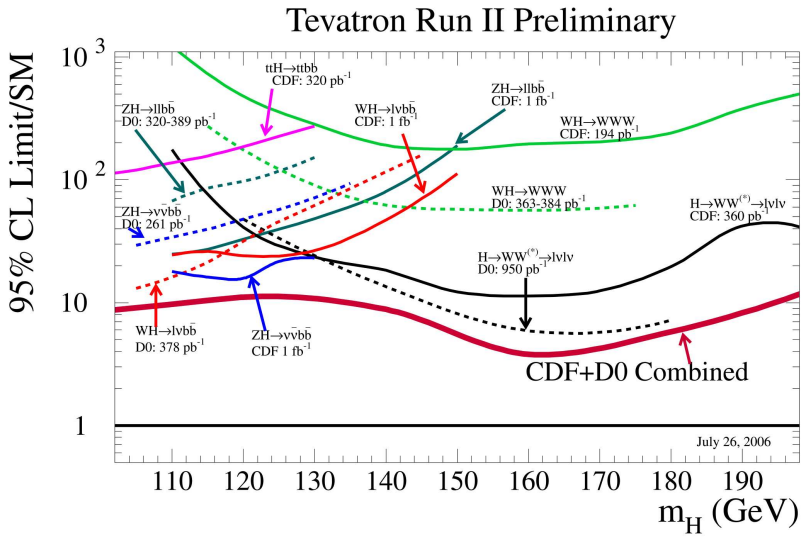

Figure 2.6: *Ratio of accumulated luminosity to that required to exclude SM Higgs boson production at 95% CL over a range of masses at the Tevatron (Summer 2006, [20]).*

2.6 Beyond the Standard Model

Although no data to date have directly contradicted the Standard Model and its predictions (in fact some quantities are the most precisely predicted and measured in nature), there are a number of problems. Aside from failing to describe the gravitational force, two main issues are the hierarchy problem and gauge coupling unification. The hierarchy problem [26–28] is essentially that the Higgs mass is as small as predicted. The Standard Model is expected to be valid up to a very high energy scale,

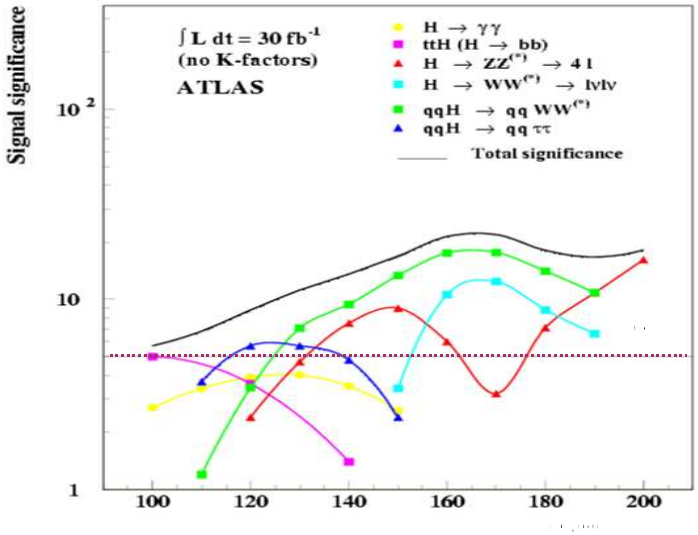

Figure 2.7: *Combined significance expected by ATLAS after accumulating 30* fb^{-1} *of data (figure from [25]).*

$\Lambda_{NP} \approx 10^{16}$ GeV, at which point some new physics will become apparent. Because there are quadratically divergent contributions to the Higgs mass, the natural value would be of the order of this new physics. The only way (within the Standard Model) the hierarchy problem could be solved is if loop corrections are of the precise order required to almost exactly cancel the divergent terms. Because of the difference in magnitude, this 'fine tuning' would have to be of the order of 10^{-26}, which is unnatural. Gauge coupling unification is the desire that at some scale (usually near the scale Λ_{NP} above), the couplings become equal. This would allow one to unify the strong, weak and electromagnetic force in some Grand Unified Theory (GUT). It is already known that the couplings vary depending on the energy one looks at, but within the Standard Model extrapolation of these 'running' couplings does not feature an intersection for all three couplings at the same energy scale.

One of the most common solutions to these problems is supersymmetry (SUSY) [29, 30]. The basic premise is that every fermion has as a boson partner and every boson has a fermion partner. The superparticle would be expected to have the same mass

as its Standard Model partner - which would hold as true for the Higgs boson as any other. Because this 'Higgsino' partner is a fermion, its mass is stable (one can think of supersymmetric loop diagram cancelling out each divergent Standard Model one). These partners have not yet been observed, so SUSY cannot be an exact symmetry and must be broken at some scale. This scale is expected to be near the *vev* of the Higgs field and should therefore be observable at the current generation of collider experiments. An additional benefit of supersymmetry being on the order of the TeV scale is that the running coupling constants change their behaviour and could possibly all intersect at one point. This is considered a strong point in favour of SUSY, but conclusive evidence needs direct detection of the superpartners. In fact there are other ways to solve the aforementioned problems and also more than one flavour of SUSY; the next section will consider the Minimal Suspersymmetric Standard Model (MSSM) and concentrate on the Higgs sector.

Although for most particles in the Standard Model it is perfectly adequate to add one superpartner, if one does this for the Higgs boson one finds this introduces a gauge anomaly. If, however, one has two Higgsinos this is resolved. Of course one must then have an additional scalar Higgs doublet for symmetry. There are many of these two Higgs Doublet Models (2HDM's [31]) but the one used in the MSSM, type 2, predicts five Higgs bosons. Two are CP-even and neutral (h^0 and H^0), one is CP-odd and neutral (A^0) and the other two charged (H^+ and H^-). One expects that one of the CP-even states will be light (the mass should not be greater than $\approx 130\text{GeV/c}^2$) and Standard Model-like in its behaviour. The other CP-even state should be degenerate with the CP-odd state, A^0. Because there are now two Higgs doublets there are two *vev*'s, v_1 and v_2. Two parameters are typically used to describe the Higgs sector; one is the mass of the CP-odd Higgs boson A^0 and the ratio of the *vev*'s

$$\tan\beta = \frac{v_2}{v_1} \tag{2.36}$$

One then postulates scenarios depending on the size of these values and what one expects to be able to observe. At the LHC at least one Higgs boson should be visible across the entire parameter space. For example, with 30 fb^{-1} of data in the no mixing model, the situation is as shown in fig. 2.8. One sees that at least one type of Higgs boson is generally visible at low m_A for all $\tan\beta$. For m_A above 150 GeV/c^2 a gap region appears at medium $\tan\beta$ ($\approx$ 10), increasing in area as m_A increases. Fig. 2.9 shows that once 300 fb^{-1} has been accumulated, this gap is closed largely by the associated production Wh and $\bar{t}th$ channels, with $h \to \bar{b}b$ and $h \to \gamma\gamma$ decays. Searching for Supersymmetry is particularly important because the latest precision electroweak data favours supersymmetry with a low mass Higgs boson (see fig 2.10, an alternative view to the left-hand side plot in fig. 2.4).

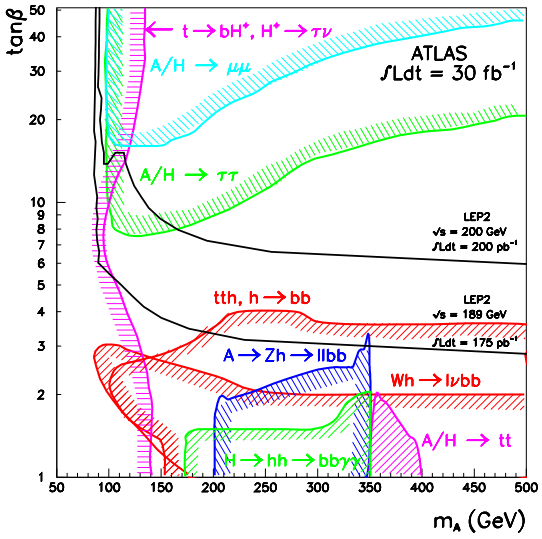

Figure 2.8: *Observability of various MSSM Higgs bosons in the no mixing model, over the MSSM parameter space for 30* fb^{-1} *of data accumulated by ATLAS. The shaded areas indicate the observable (5σ) region and the area below the black line are excluded at 95 % CL by notional LEP predictions.*

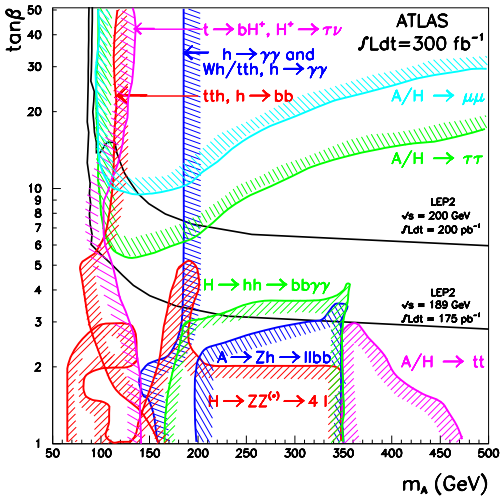

Figure 2.9: *Observability of various MSSM Higgs bosons in the no mixing model, over the MSSM parameter space for 300* fb^{-1} *of data accumulated by ATLAS. The shaded areas indicate the observable* (5σ) *region and the area below the black line are excluded at 95 % CL by notional LEP predictions.*

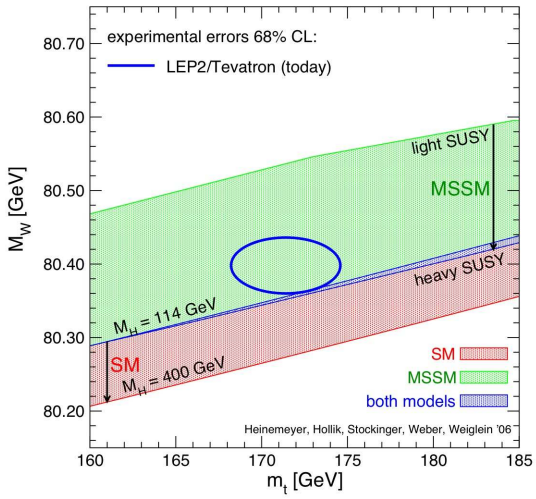

Figure 2.10: *Constraints on the Higgs mass based on latest (March 2007) measurements of the top mass and precision electroweak measurements. Shown is the* 1σ *region compatible with the new* m_t *and* m_W*. The region lies in the SUSY domain suggesting this may be the correct model to search for.*

Chapter 3

The Large Hadron Collider

This chapter introduces the Large Hadron Collider (LHC) project, describing the collider itself and a summary of the four experiments being run at points along the beam-line. Then the main physics studies to be investigated are described, with reference to previous experiments and theoretical predictions.

3.1 Accelerator Design

The LHC [32] will primarily be a proton-proton ring collider with a centre of mass energy of 14 TeV, which will also be capable of heavy ion acceleration. It is being built at CERN within the 27 km long tunnel previously used in the LEP experiment. Aside from the main collider, smaller accelerators are used to boost the protons' energy to a level suitable for injection into the LHC (see fig. 3.1). The protons are produced in a linear accelerator at 50 MeV and are then boosted to 1.4 GeV in the proton synchrotron booster. This feeds into the Proton Synchrotron (PS) proper which accelerates them to $\approx$25 GeV, before passing on to Super Proton Synchrotron (SPS). The energy for injection into the LHC from the SPS will be 450 GeV. The LHC beam-pipe is held entirely under vacuum and is cooled in places to temperatures as low as 1.9 K in order for the superconducting magnet system to operate. These

niobium-titanium magnets are of a type capable of producing magnetic fields strong enough (≈8 Tesla) to steer the 7 TeV beams. The Radio Frequency (RF) cavities are also superconducting and are responsible for accelerating and maintaining the 7 TeV beams in bunches, at 25 ns intervals with each bunch containing around 10^{11} protons. The design luminosity is 10^{34} cm^{-2}s^{-1}, though this will only be achieved after several years running, from a starting point of 10^{33} cm^{-2}s^{-1}. When the design luminosity is reached around twenty-four simultaneous interactions are expected at each bunch crossing, which act as a simultaneous background (or pile-up) to any 'interesting' events.

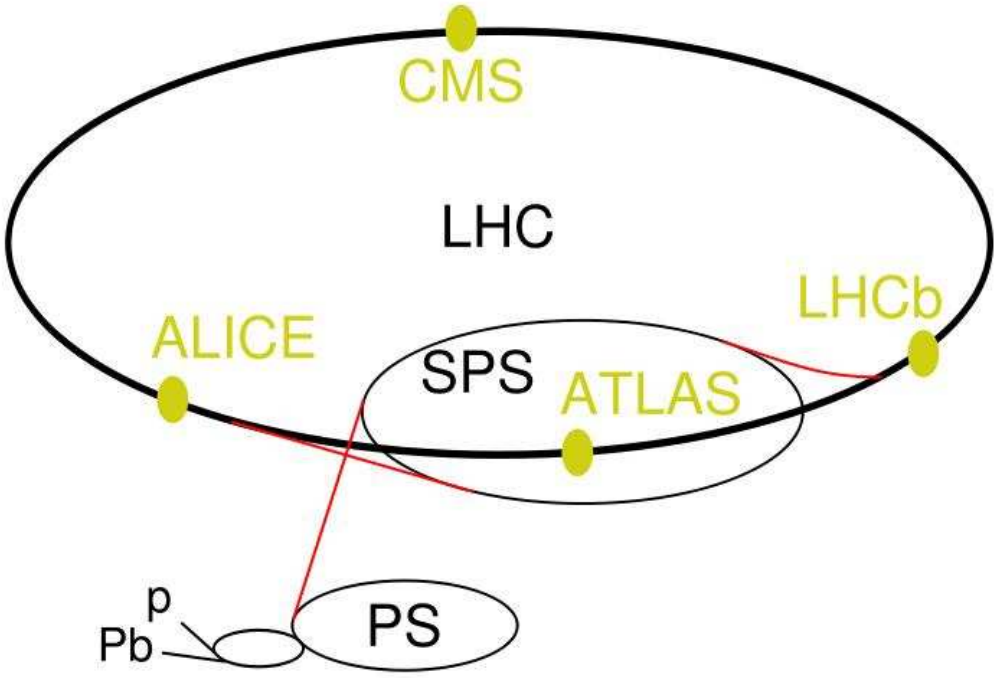

Figure 3.1: *Accelerators at the LHC. A linear accelerator feeds the PS (via the PS booster), which in turn feeds the SPS. The SPS provides the final boost before injection to the LHC.*

3.2 LHC Experiments

There are four experiments being run on the LHC beam-line, the proton beams being steered such that the bunches cross at four interaction points (see fig. 3.2). Two of these experiments are general purpose detectors, designed to look at many different types of physics. These are ATLAS [33] (A Toroidal LHC ApparatuS) and CMS [34] (Compact Muon Solenoid). The LHCb [35] experiment is different in that it is designed solely to look at b-physics, whilst the final detector ALICE [36] (An LHC Ion Collider Experiment) is different again in that it looks at heavy ion collisions (which will use approximately 10% of beam-time).

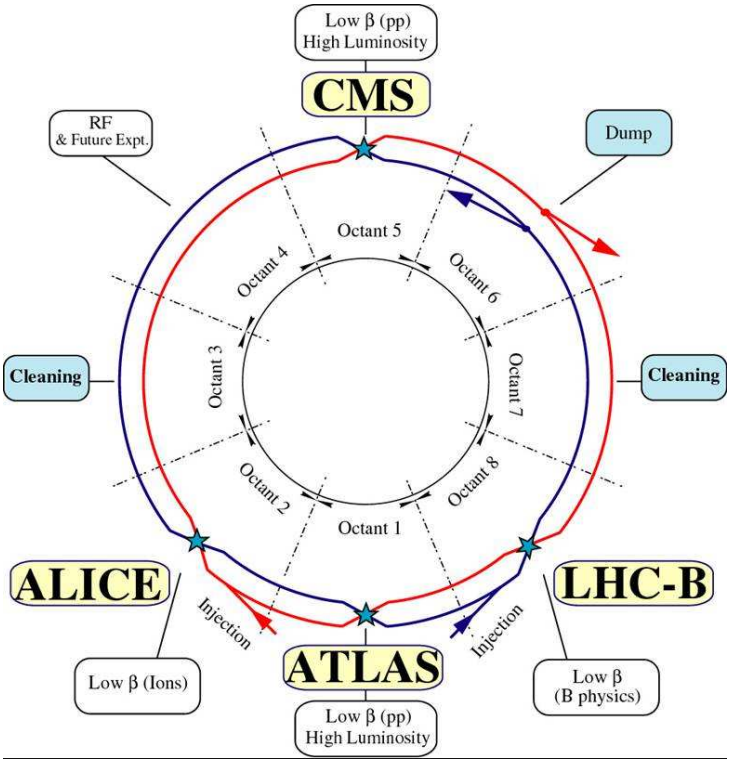

Figure 3.2: *The four experiments at the LHC and their relative position in the ring.*

3.3 Physics Motivation

3.3.1 Standard Model Measurements

A large part of the physics program is dedicated to measuring parameters of the Standard Model either to higher accuracy (due to larger cross-sections) or unmeasured parameters (at energies previously inaccessible). In the case of CMS and ATLAS these include W mass measurements, gauge boson triple coupling (e.g. WWZ) and particularly the mass, coupling and decay properties of the t-quark. LHCb will measure many of the properties of B-mesons, producing more accurate measurements (particularly of Charge-Parity (CP) violation) than were previously possible.

3.3.2 Higgs Boson

A huge motivation for building the LHC is to attempt to discover the Higgs boson, not least because measurements at LEP suggested it may not be far from the operating reach of that machine. ATLAS and CMS both have very extensive Higgs boson search programmes, covering a large mass range (from 114.4 GeV/c^2, excluded at 95% confidence level by LEP [22], to several hundred GeV/c^2, beyond which theoretical predictions become restrictive [37]) and many different production and decay modes. If and when discovery is made, these experiments will also attempt to measure some of the key properties of the Higgs boson, such as its coupling to other particles.

3.3.3 Beyond the Standard Model

Searches for new physics at the LHC are expected by many to prove fruitful, because some discrepancies exist in the established Standard Model. For instance the Hierarchy Problem [26–28] (why the Higgs mass is so much smaller than the Planck mass) may be solved by Supersymmetry (SUSY) [29, 30], discussed further in §2.6. If these partners exist they should be within reach of the LHC and detectable by ATLAS and

CMS. Another clue to new physics would be in CP violation in the B-meson system, if it is found that measurements are not compatible with a single unitarity triangle. LHCb will be the main detector in this search though the general purpose detectors will also be involved. A final mention is due to the heavy ion program which it is hoped will produce energies and densities high enough to resemble the very early universe. ALICE will investigate the quark-gluon plasma phase of matter, to test the validity of certain cosmological models [38].

Chapter 4

The ATLAS Detector

4.1 Overview

The ATLAS detector will be the largest and most complex detector ever built, with much of the hardware already installed as of early 2007. Measurements involving transverse energy require the detector to be hermetic in the pseudorapidity range $[-5, 5]$. Therefore ATLAS is cylindrical in shape, with a diameter of 22 m and length of 42 m. A cross-sectional view along its axis is shown in fig. 4.1. The number of particles, especially at high luminosity running, requires excellent tracking from the inner detector, whilst the outer sections must achieve excellent energy resolution of the outgoing particles. What follows is a breakdown of each of the detector subsystems, as defined in [39], though the initial layout will differ slightly (see §4.8).

4.2 Co-ordinate System

The Cartesian co-ordinate system used by ATLAS is as follows: The origin is the nominal interaction point; the x-axis is roughly horizontal and points from the origin to the centre of the ring; the z-axis points along the anti-clockwise beam direction (as viewed from above); the y-axis points upwards with respect to the x and z axes

(This is slightly off local geological vertical) to complete the system. These can then be converted to spherical co-ordinates, with the polar angle (θ) measured from the beam axis in the $z-y$ plane and the azimuthal angle (ϕ) measured around the beam axis in the $x-y$ plane (see Eqns. 4.1, 4.2). For ATLAS, ϕ is measured from the $+x$-axis (positive values being anti-clockwise) and θ measured from the $+z$-axis, positive values being in the positive z-direction. Convention in particle physics is to use another quantity, pseudorapidity (η) defined in Eqn. 4.3, because particle production is more uniform when viewed in this system and vitally particle separation in η-space is Lorentz invariant. The size of objects and their separation can now be measured in this pseudorapidity-azimuthal phase space and we define a distance parameter ΔR in Eqn. 4.4.

$$\phi = tan^{-1}\left(\frac{y}{x}\right) \tag{4.1}$$

$$\theta = cos^{-1}\left(\frac{z}{\sqrt{x^2+y^2+z^2}}\right) \tag{4.2}$$

$$\eta = -ln\left(tan\left(\frac{\theta}{2}\right)\right) \tag{4.3}$$

$$\Delta R = \sqrt{(\Delta\eta)^2 + (\Delta\phi)^2} \tag{4.4}$$

4.3 Magnet System

ATLAS uses a superconducting magnet system, consisting of a central solenoid surrounding the Inner Detector (see §4.4) and three air-filled toroids outside the calorimeter. The inner solenoid is unusual in that it is closer to the beam than the calorimetry systems, to maximise field strength and uniformity (of 2 T). However the drawback is that the material causes showering to begin before the calorimeter is reached, so compromises on the solenoid design are made (such as sharing the same cryostat as the Electromagnetic Calorimeter). The air-core toroids (one barrel plus two end-caps) each consists of eight flat coils assembled radially and symmetrically around the beam

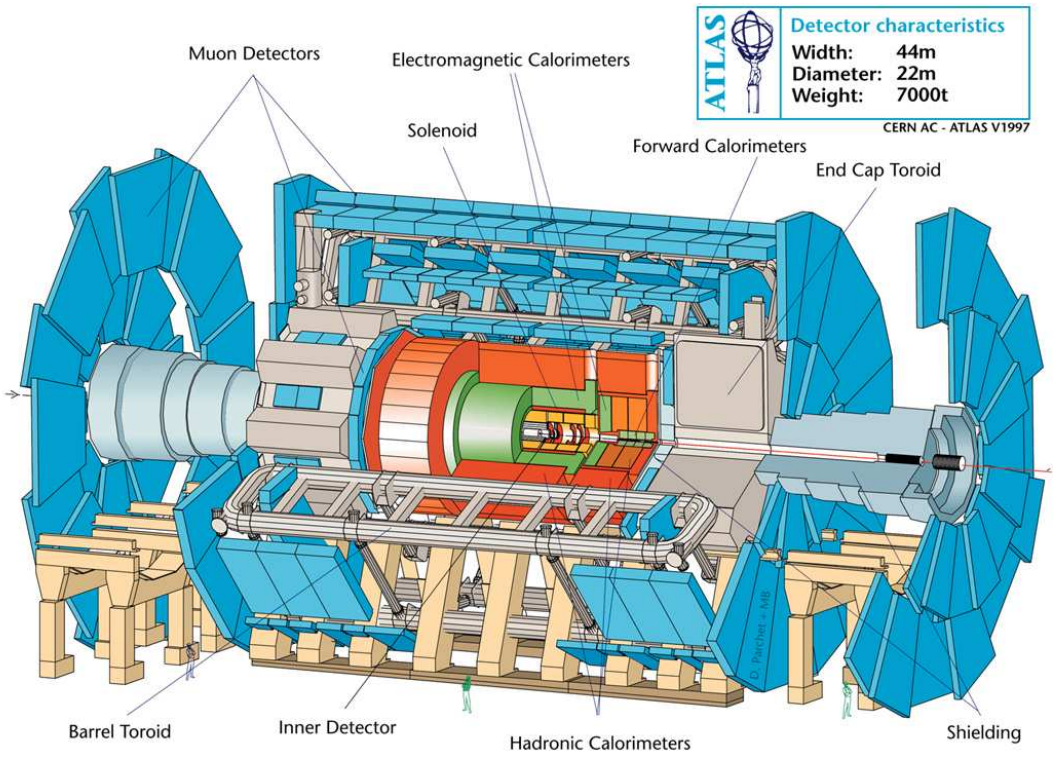

Figure 4.1: *The ATLAS Detector*

axis, outside the calorimetry system. The open system reduces multiple scattering effects on momentum resolution, as well as the overall detector weight, whilst creating a toroidal field perpendicular to the outgoing particles' direction. Field strength is 2 T in the central region and 4 T in the end-caps.

4.4 Inner Detector

The Inner Detector (ID) reconstructs tracks of charged particles and measures their momentum, based on their curvature in the 2 T solenoid field. As the name suggests it is the innermost part of the detector measuring just 1.15 m in radius and 6.9 m in length, with an acceptance region of $|\eta| < 2.5$. At initial low luminosity it should be capable of reconstruction of charged tracks with $p_T > 0.5$ GeV/c from primary

and secondary decay vertices, with $> 95\%$ efficiency over the full coverage. This is made possible by three subsystems: the pixel detector; semiconductor tracker (SCT) and transition radiation tracker (TRT) (see fig. 4.2). The first two of these provide outstanding resolution (with a correspondingly large number of readout channels), but relatively few hits per track, whereas the TRT provides many more hits, but at the cost of much lower resolution.

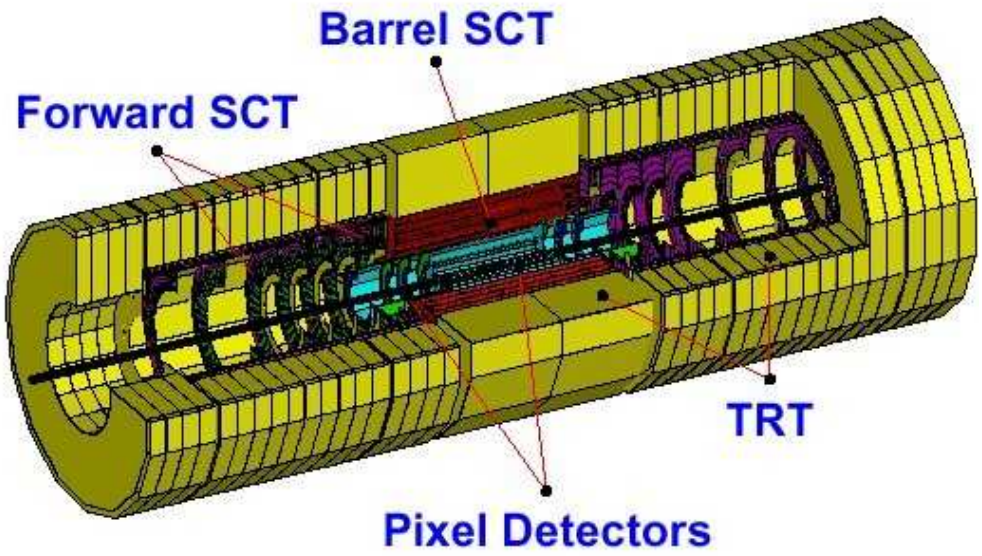

Figure 4.2: *The ATLAS Inner Detector*

4.4.1 Pixel Detector

The pixel detector is the closest to the beam-pipe. It can measure positions very accurately, which is vital for secondary decay identification. Precise knowledge of impact parameters is key when identifying B-hadrons and thus tagging b-flavoured jets. Each pixel is 50 μm in ϕ and 400 μm in z, with a total active detector area of 2.3 m^2. If a charged particle passes through a cell, ionisation in the silicon substrate is collected and read out directly via one of the millions of dedicated channels. The pixel

modules are arranged in three layers at radii (from the interaction point) of 5.05 cm, 8.85 cm and 12.25 cm. The innermost of these (the 'B' layer) will be subject to the harshest radiation environment and has therefore been designed to be upgradeable.

4.4.2 Semiconductor Tracker

The Semiconductor Tracker (SCT) is based on silicon microstrip technology, with n-type bulk as it is the most radiation resistant [40]. In the barrel region ($|\eta| < 1.4$) there are four layers allowing for four measurements of track points, at radii of 30 to 52 cm. Each layer consists of two modules with a pitch of 80 μm glued back-to-back, with a slight offset of 40 mrad. The first module is aligned with the beam-pipe and allows measurement of ϕ, whilst the second measures the z-coordinate. In each end-cap region there are nine disks covering a similar radial distance as the barrel region (from 26 to 56 cm), in the $|\eta|$ region 1.4 - 2.5. In both barrel and end-caps the expected resolution is 16 μm in ϕ and 580 μm in z (barrel) or r (end-cap).

4.4.3 Transition Radiation Tracker

The Transition Radiation Tracker (TRT) uses proportional counters known as straws, filled with a Xe-CO_2-CF_4 gas mix. A gold-plated W-Re wire in each straw acts as the anode, with a mean electronic drift time of 40 ns. On average an outgoing particle will hit 36 tubes which, despite providing relatively poor accuracy compared to the silicon detectors, is vital in determining the momentum of tracks and plays a major part in electron identification. The barrel region ($|\eta| < 0.7$) extends over radii 56 to 107 cm, with the straws placed in 73 layers parallel to the beam axis. In each end-cap region ($0.7 < |\eta| < 2.5$) there are 18 'wheels' with radially mounted straws, the different orientations maximising the number of straws a particle will pass through.

4.5 Calorimetry

Calorimeters measure energy deposition from electrons, photons and hadrons. Because of the different way these particles interact, it is customary to divide the calorimetry into electromagnetic and hadronic sections. In the case of ATLAS (see fig. 4.3), there is an electromagnic calorimeter covering the pseudorapidity region $|\eta| < 3.2$, a hadronic barrel calorimeter covering the region $|\eta| < 1.7$, hadronic end-caps covering $1.5 < |\eta| < 3.2$ and forward calorimeters covering $3.1 < |\eta| < 4.9$.

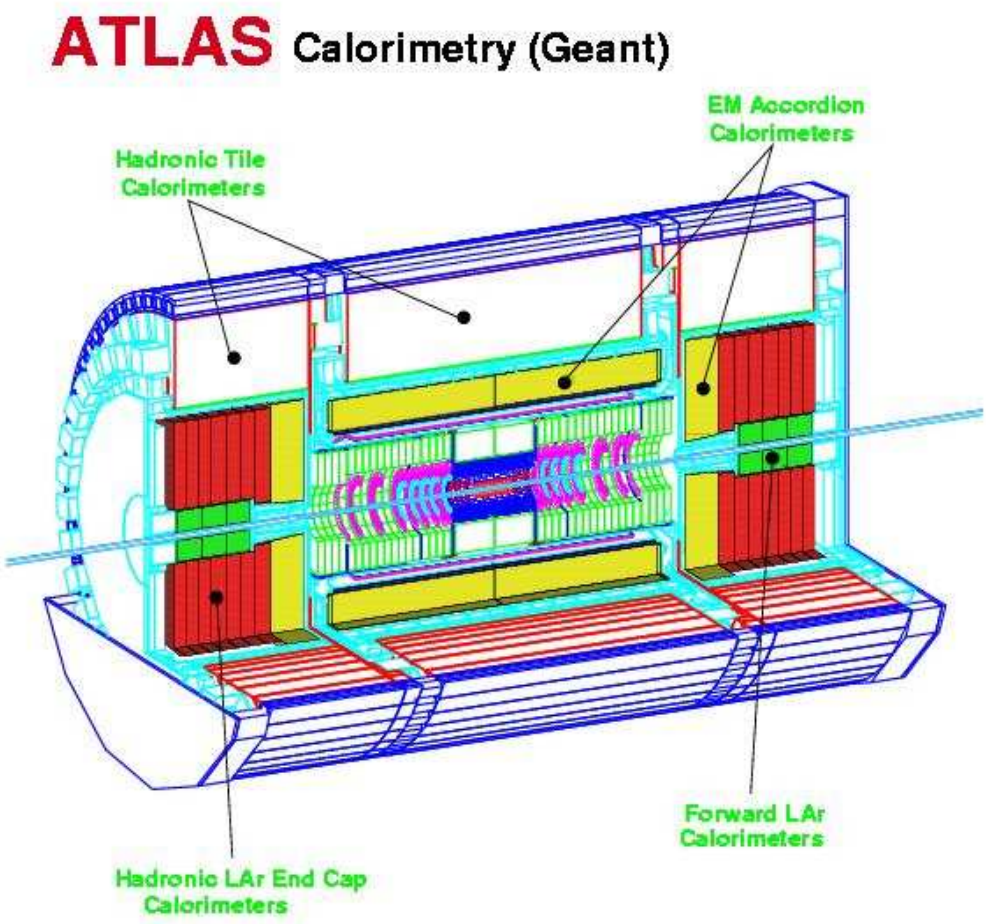

Figure 4.3: *The ATLAS Calorimeters*

4.5.1 Electromagnetic Calorimeter

The ATLAS Electromagnetic (EM) Calorimeter (Cal) is a sampling calorimeter, with inter-spaced layers of lead plates and liquid argon (LAr). Lead plates cause showering of electrons giving rise to bremsstrahlung photons. These then convert into $e^{\pm}$ pairs, producing secondary particles which create ionisation in the LAr gaps. A high electric field causes the ionisation electrons to drift to copper electrodes. The lead plates have an accordion geometry which allows complete azimuthal(ϕ) coverage and the detector itself is segmented into sampling regions. The Presampler is simply a thick layer of argon with no lead, covering the region $|\eta| < 1.8$, whose purpose is to correct for losses in the inner detector and solenoid. The three sampling layers after this vary in granularity (resolution) according to their pseudorapidity, the majority (energy less than 50 GeV) of EM showers in the barrel region being covered by the 2nd sampling with a resolution of $\Delta\eta \times \Delta\phi = 0.025 \times 0.025$. As the EM Cal is devoted to precision physics in the low pseudorapidity region ($|\eta| < 2.5$) it requires very good energy resolution, as shown in Eqn. 4.5 (for energy in GeV).

$$\frac{\sigma_E}{E} = \frac{0.1}{\sqrt{E}} \oplus \frac{0.3}{E} \oplus 0.01. \tag{4.5}$$

4.5.2 Hadronic Calorimeter

The ATLAS Hadronic Calorimeter in the central region ($|\eta| < 1.7$) is a sampling calorimeter which uses an iron absorber and plastic scintillating tiles as the active material. As in the LAr, the alternating structure of metal plates (to initiate showers) and detector substrate is used. The (blue) light from the scintillators is absorbed by wavelength shifting fibres, which re-emit photons of longer wavelengths suitable for photomultipliers. Because the Hadronic Calorimeter's main task is measurement of larger jets, the granularity need not be as fine as in the EM Cal. In the main these barrel calorimeters have a resolution of $\Delta\eta \times \Delta\phi = 0.1 \times 0.1$, dropping to 0.2×0.2 for $|\eta| > 2.5$. At higher pseudorapidity ($1.5 < |\eta| < 3.2$) the hadronic end-cap (HEC)

calorimeters provide the coverage. Like the EM Cal, LAr is used as it is radiation hard, though the plate material here is copper. The very forward regions ($3.1 < |\eta| < 4.9$) are also covered by LAr calorimeters, with a mixture of copper and tungsten plates. This choice of material limits the size and width of very forward jets and cuts down on background into the more central calorimeters. Due to the lower granularity, energy resolution is not expected to be as high as in the EMCal, the design being as in Eqn. 4.6 (for energy in GeV) in the region $|\eta| < 3$, the constant term increasing to 10% in the region $3.0 < |\eta| < 4.9$.

$$\frac{\sigma_E}{E} = \frac{0.5}{\sqrt{E}} \oplus 0.03. \tag{4.6}$$

4.6 Muon System

The muon system in ATLAS (see fig. 4.4) is a key component as it serves as a trigger for some of the most important search channels and a high precision muon spectrometer for measuring track momenta. For example, the 'golden' Higgs boson search channel $H \to ZZ^* \to \mu\mu\mu\mu$ should be detectable giving a Higgs mass resolution of $\approx 1\%$. The triggering is achieved by Resistive Plate Chambers (RPC's) in the barrel region ($|\eta| < 1$) and Thin Gap Chambers (TGC's) in the transition ($1.0 < |\eta| < 1.4$) and endcaps ($1.4 < |\eta| < 3.0$). The RPC's are gas-filled parallel plate capacitors which work by collecting electrons from ionisation caused by traversing muons. The TGC's work effectively like multi-wire proportion chambers and operate in the environment with higher count-rates because of their better spatial resolution. These two detector types are also used (in their respective regions above) for measuring the secondary co-ordinate (ϕ) of tracks. The precision systems used are Monitored Drift-Tube Chambers (MDT's) and Cathode Strip Chambers (CSC's) in the outer end-caps ($|\eta| > 2$) for extra coverage where higher granularity is required. MDT's consist of 3 cm diameter aluminium tubes, with a single central wire providing spatial resolution of ≈ 80 μm. CSCs are multi-wire proportional chambers capable of precise

(< 60 μm) position measurement along the anode wires, by determining the centre of gravity of the charge induced by the avalanche on one of the cathodes. As well as providing η measurement in the high pseudorapidity region, they assist the TGC's with ϕ measurement.

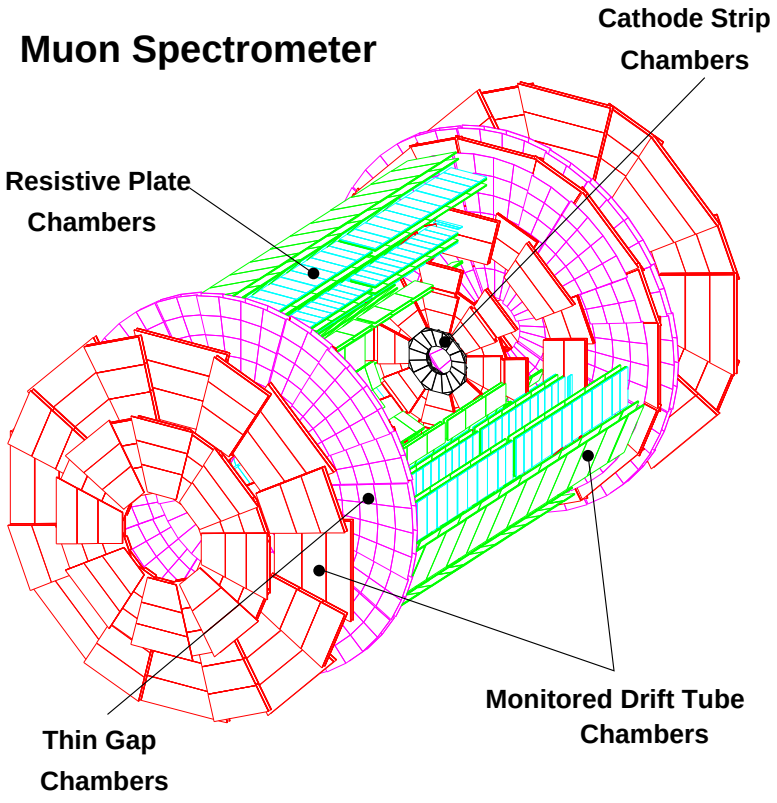

Figure 4.4: *The ATLAS Muon System*

4.7 Triggering and Data Acquisition

The ATLAS trigger and Data Acquisition (DAQ) system is based on three layers of event selection [41], [42]. Their task is to reduce the initial event rate (40 MHz at maximum luminosity), to a level manageable for both offline processing and permanent storage. Firstly, the Level-1 trigger (LVL1) reduces the rate to 75 kHz using

a series of simple triggers (e.g. an isolated electromagnetic deposit over 25 GeV, EM25I). These are chosen to meet the requirements of the majority of physics channels, but some flexibility is possible. Interesting events are stored in readout buffers for consideration by the level-2 trigger (LVL2), which applies selection algorithms to further test the desirability of an event (e.g. Secondary muons from pions and kaons, low energy muons selected due to the limited LVL1 resolution and cavern background muons must all be removed). If the event passes LVL2, the DAQ system transfers the readout buffer to the third level filter, the event filter (EF). The EF runs offline algorithms and has extra information available, such as alignment and magnetic field data. The combined output of LVL2 and the EF is the High Level Trigger (HLT) and if the event passes this final stage it is stored offline, this happening typically on the order of 100 Hz. The 100 Mb/s storage rate means total stored data will exceed 1 Pb per year, which will all be accessible to those performing physics studies. Note however that in the analysis presented here, the trigger is not simulated and is approximated by a cut throughout this study.

4.8 Staging and Deferrals

When the LHC begins operation, sections of ATLAS will not be complete (largely due to funding restrictions). Key missing sections include: the middle pixel layer; the end-cap 'C' wheels in the TRT; eight sections in the muon end-cap CSC's; half of the Digital Signal Processor boards for the LAr instrumentation and HLT+DAQ deferrals mean the LVL1 trigger rate must be 40 kHz. The two areas above most damaging to the channel presented in this study are the trigger, as threshold levels have had to be increased to achieve the new rates, and the pixel layer, because very good b-tagging of jets is highly dependent on the resolution achieved by the silicon tracking sections of the Inner Detector. This detector layout is known as the 'Initial' layout and all physics studies in this analysis use a flavour of this layout throughout (known as 'Rome-Initial', see [43]).

Chapter 5

Software

5.1 Introduction

This chapter describes the software packages used in detector simulation, object reconstruction and event reconstruction. The first section introduces Monte-Carlo event simulation and then describes the two different detector simulations (full and fast). The next section discusses the specific case of jet reconstruction, comparing the cone and k_T algorithms. The final section describes the environment for analysis, with particular reference to the EventView package.

5.2 Event and Detector Simulation

In order to understand the results when actual data is produced, it is necessary to simulate the event and its interaction with the detector. The first step is the hard process, in which two partons from the colliding protons interact. The density of partons within the protons is described by Parton Distribution Functions (PDF's), which defines the fraction of energy and flavour type of the constituents. The hard process is described by matrix elements, calculated to first order. After the hard scattering, radiation from the initial/final state partons is included. Sometimes this

Final State Radiation (FSR) is also calculated exactly, depending on whether the relevant matrix elements have been calculated. In any case, at some point evolution via Parton Showering (PS) is introduced, to provide a link between the perturbative QCD parton stage and the bound state hadrons which are observed. The lowest energy partons, together with the remnants of the colliding protons, undergo a process called hadronisation. These 'jets' of hadrons will decay to stable particles which interact with the detector.

True detector simulation requires an accurate description of the detector (in terms of geometry and material) and must be able to simulate physics events and track particles as they interact with the detector. It should cope well with all physics processes, across the anticipated energy range of the LHC. For the ATLAS software release 9.0.4 (the so called 'Rome' production) this was done by the GEANT4 package [44]. This is a version designed from the outset to handle the environment of the LHC (high energy hadronic processes) and is far more adaptable to changes in geometry than its predecessor. Nearly all the 1.5 x 10^8 active detector volumes of the real ATLAS detector are simulated, together with various dead zones and other material which may affect physics processes. Consequently simulation is a very computer intensive process. Before reconstruction can begin a secondary stage called digitisation is needed. The purpose of this is to present the data as is expected from the detector, including simulation of the front-end electronics and noise injection. The Raw Data Objects (RDO's) produced are the input to the full reconstruction, which is discussed below (or in more detail in the ATLAS Computing Technical Design Report [45]).

In full reconstruction there are two distinct reconstruction types: the tracking system and calorimeter reconstruction. The tracking system is a common framework used separately in the inner detector and muon chambers. Clusters of hits in the pixel detectors and drift circles in the muon tubes, together with space points are used to identify tracks. In the calorimeters, the basic constituents are CaloCells which are combined into towers and ultimately CaloClusters. Identification of physics objects

is achieved by combining the output of the detectors. For example, electrons are found by matching an inner detector track with an electromagnetic cluster from the calorimeter. All data from reconstruction is stored in the Event Summary Data (ESD), though this is typically slimmed to the Analysis Object Data (AOD) form.

Fast simulation and reconstruction is necessary because very large data samples are too CPU intensive to simulate fully. The package used is called ATLFAST and its strategy is somewhat different (see [46] for initial conception and [47] for the C++ implementation). Instead of simulating detector response, it simply takes the stable particle content from the Monte-Carlo. The energy and momenta are then smeared with parameters calculated from full simulation studies. Clusters in the calorimeters are created by summing all stable interacting particles in simple calorimeter cells. Clusters are then assigned to discrete Monte-Carlo particles (electrons, muons and photons), which are within a cone of the cluster. Remaining clusters are free as input to jet-finding algorithms and any remaining after this stage are used in reconstructing the event's missing energy. The output of ATLFAST can be stored in the ESD or AOD, the key being that at the AOD level one can, to first order, work with the fast simulated data in the same way as fully simulated data.

5.3 Jet Reconstruction

In either full or fast simulation one has identified energy clusters which need to be combined into jets. In ATLAS the cone algorithm has been the classical choice, though in recent years the k_T algorithm has started to attract interest as an alternative.

5.3.1 Cone Algorithm

The cone algorithm for jet finding is very intuitive and easy to understand. From the energy clusters, sometimes called a protojet or in 3D projection through the calorimeter, a tower, a starting point (or seed) is chosen. This seed is the tower with the highest E_T, provided it is above a threshold $E^{seed}_{threshold}$. Then every tower within a

cone in ΔR space drawn around the seed is attributed to that jet and its transverse energy added to the jets overall E_T^{jet}. As each tower is added to the jet it is removed from the list of protojets i.e. there is no energy sharing between jets (in the most simplistic implementation). When all towers within the cone have been added, a check is made to see if $E_T^{jet} > E_{threshold}^{jet}$, in which case the jet is kept. If this not the case all towers are returned for use in other jets and the seed is marked, so it will not beused as a seed again. The process begins again with a new seed until there are no seeds above the threshold at which time the algorithm is complete.

5.3.2 k_T Algorithm

The k_T algorithm [48] is more complicated and is an evolution rather than a simple construction. It is however more amenable to theoretical calculations. The algorithm starts by defining each protojet's transverse momentum relative to the beam:

$$D_{iB} = P_{Ti}^2 \tag{5.1}$$

then for each pair of jets, i, j :

$$d_{ij} = min(P_{Ti}^2, P_{Tj}^2)^2 \frac{R_{ij}^2}{R_{cut}^2} \tag{5.2}$$

where $R_{ij}^2 = (\eta_i - \eta_j)^2 + (\phi_i - \phi_j)^2$ i.e the separation in angular space.

The R_{cut} parameter is analogous to cone size and controls how long the algorithm will iterate (see below). The next step is to find the smallest of all d_{ij} and D_{iB}. If it is d_{ij} the two protojets are combined (usually by adding the four vectors) to create a third protojet d_k. If it is D_{iB}, this is stored as a jet. This process repeats until all protojets have been included in jets, or are sufficiently separated that further merges are not possible. Note that as the R_{cut} parameter decreases, the d_{ij}'s will increase, making further combinations less likely. Thus more jets are found, but each with lower p_T.

5.4 EventView Analysis Framework

One of the main problems of the ATLAS reconstruction mechanism is that each particle type has its own reconstruction software. Each is independent of any other and has all the base constituents (tracks, clusters etc) available for use. Therefore, when the AOD is presented to the user the same particle may be identified twice as two types (a τ-lepton and jet for example). Obviously this is inconsistent and to aid the user in resolving this, the Eventview package [49] was developed. Firstly one uses 'inserters' to create a link to particles from the AOD. The order these are implemented allows one to decide which algorithm has priority and any other objects which overlap (in ΔR space) can be excluded. Thus in one 'view' an event may contain a τ-lepton and in another, with re-ordered inserters, a jet. Another powerful feature is the ability to create multiple EventViews whenever an analysis decision is taken (This was a feature planned from the start, but a private implementation by this text's author was necessary in the interim, the official code eventually being adopted/merged). For example when there are combinatorial possibilities e.g. two leptons from a possible four to form a Z^0-boson, one may wish to keep more than one and run further analysis steps. This allows multiple 'streams' to be created and discarded at will. A final useful feature is that user defined data of multiple types (vectors, doubles etc) can be added to any EventView and its descendants. This is more elegant than e.g. storing objects in the Transient Data Store (TDS), which in effect creates a global variable as each would need a unique key.

Chapter 6

Study of the $t\bar{t}H, H \to b\bar{b}$ Search Channel

6.1 Introduction

This chapter describes the Monte-Carlo simulation and reconstruction of the $t\bar{t}H, H \to b\bar{b}$ Higgs boson search channel, with a final state as shown in fig. 6.1, and major backgrounds to this. The first section describes the generation of the Monte-Carlo samples and the properties of basic objects, for the signal and two dominant backgrounds. This continues with a reconstruction of the event at the parton level, to identify the most difficult areas. Subsequent sections step through a cuts based analysis in detail, at each stage maximising signal acceptance whilst retaining good purity. The final efficiency is calculated for a variety of masses for 30fb^{-1} of integrated luminosity. The final two sections describe the studies made on systematics and how the results compare with other studies.

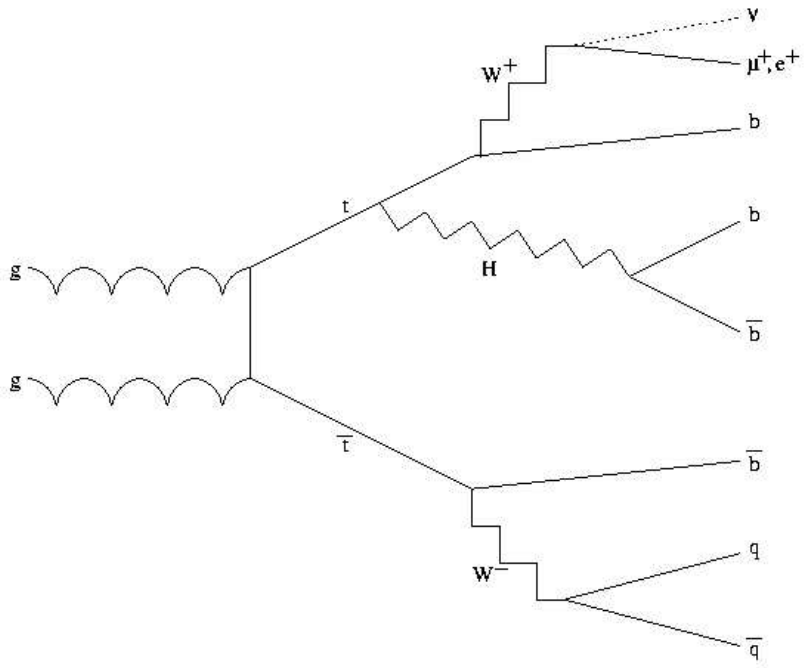

Figure 6.1: *Feynman diagram for the semi-leptonic final state of the $t\bar{t}H, H \rightarrow b\bar{b}$ channel, showing it has 4 b-jets, 2 light jets, a charged lepton and missing momentum in the form of a neutrino.*

6.2 Monte-Carlo Studies

The first step in setting up any analysis of this type is to look at the parton and hadron level information from the Monte-Carlo generator. This allows one to look at the physics process and how to reconstruct it, without adding in the complications of detector reconstruction efficiencies, noise and mismeasurements. This section first details the programs and parameters used for event generation and the calculation of cross-sections and branching ratios in the signal and main background processes. Some of the basic physics properties are then investigated with a view to identify key quantities which will be most useful in distinguishing signal and background. A study is then made on the evolution from quark to reconstructed jet, jets being the most important part of this channel.

6.2.1 Monte-Carlo Sample Generation

The $t\bar{t}H, H \to b\bar{b}$ channel is a Higgs boson search channel which is most viable in the lower reaches of the predicted mass range (100-130 GeV/c^2). The samples generated for this analysis are therefore produced with Higgs masses of 100, 110, 120 and 130 GeV/c^2. The $t\bar{t}H, H \to b\bar{b}$ channel has a complicated final state and thus there are very few background processes which can mimic it successfully. The most obvious is the $t\bar{t}b\bar{b}$ process, where the the extra b-quarks originate from Initial and Final State gluon Radiation(ISR/FSR). This is known as a "semi-irreducible" background because the final state composition is genuinely identical to the signal (there are also electroweak contributions which produce this final state, but the cross-section for these processes is much lower). The other background of main concern is $t\bar{t}jj$ which is known as a "reducible" background. In this case the final state is not identical to the signal, the difference being that the additional jets are light. However, these can be mis-tagged as b-jets during reconstruction (albeit with a low probability) and a very large cross-section makes this channel a danger. Other large cross-section processes, such as W+jets, are also greatly rejected by the b-tagging and the full event reconstruction which is employed. Because both of the major background processes both essentially depend on $t\bar{t}$ production rates, knowledge of the reliability of these predictions is desirable. Recent results at CDF [50] have measured the $t\bar{t}$ cross-section and found it to be within the Monte-Carlo prediction.

To produce the signal events the PYTHIA program [51], version 6.221, was used. PYTHIA is a full Monte-Carlo generator for high energy colliders which deals with the entire chain i.e. hard interactions, parton distributions, initial and final state parton showers, multiple interactions, fragmentation and decay. For the $t\bar{t}b\bar{b}$ background the ACERMC package [52], version 2.3, is used in conjunction with PYTHIA. ACERMC is an exact order Matrix Element (ME) event generator, which generates the Feynman diagrams for the required channel (this is the hard interaction part above). This is then further processed by a complete generator, PYTHIA in this case, for the

parton showering and subsequent steps. The $t\bar{t}jj$ background was generated with the MC@NLO program [53,54], version 2.31, which is a fusion of a Monte-Carlo generator (HERWIG is used) with Next-to-Leading-Order calculations for physics processes. Note that the flavour of the additional jets is not defined and it is necessary to remove at generator level events where b-quarks are produced, to avoid double counting with the ACERMC sample. For all the samples some forcing of decays has been done, in order to minimise expensive computation time at later stages. In the case of the signal and $t\bar{t}b\bar{b}$ background, the W-bosons from the t-quarks are made to decay so that one decays to light leptons (electron or muon, with corresponding neutrino) and the other to a quark pair (these are referred to as the leptonic and hadronic W respectively). This reduces the cross-sections to around 28% of their initial size. In the case of the $t\bar{t}jj$ background at least one W-boson must decay to leptons (as before and additionally taus are possible) and the other is left free to decay as normal. This produces a sample with the same final event partons as the $t\bar{t}H$ and $t\bar{t}b\bar{b}$ in $\approx$56% of cases but the additional events are not a cause for concern, as they were only removed from the other samples due to computational constraints (due to the expected large rejection factors in mis-tagging b-jets, the $t\bar{t}jj$ sample was only ever expected to be run in the fast detector simulation). An additional cut has been placed on the $t\bar{t}H$ and $t\bar{t}b\bar{b}$ samples at generator level, which requires at least one lepton with $p_T \geq 10$ GeV/c. Again this is purely due to computational limitations, the reasoning being that events which fail this cut will most likely not be selected by the trigger. Details of these samples can be found below in table 6.1, showing the generator used in each case, branching ratios and cross-sections (the σ_{scale} is the inclusive cross-section multiplied by branching ratios for any forced decays).

6.2.2 Sample Characteristics

For this channel there are several parameters which are key, both in imposing limitations on the identification of signal events and distinguishing these from background

Process	Generator	Size	$H \to b\bar{b}$	$\sigma_{incl}(pb)$	$\sigma_{scale}(pb)$
$t\bar{t}H(100GeV)$	PYTHIA (6.221)	20k	0.802	0.907	0.212
$t\bar{t}H(110GeV)$	PYTHIA (6.221)	20k	0.756	0.685	0.152
$t\bar{t}H(120GeV)$	PYTHIA (6.221)	20k	0.657	0.526	0.101
$t\bar{t}H(130GeV)$	PYTHIA (6.221)	20k	0.497	0.409	0.06
$gg \to t\bar{t}b\bar{b}$	ACERMC (2.3)	50k	N/A	8.08	2.37
$t\bar{t}j\bar{j}$	MC@NLO (2.31)	2M	N/A	759	345

Table 6.1: *Monte-Carlo sample sizes and cross-sections*

events, even before detector and reconstruction efficiencies are taken into account. Some of these are shown in fig. 6.2, for the samples described above. Firstly the channel must pass a High Level Trigger (HLT) set under guidelines [42] whose purpose is to reduce the event rate to a level manageable by the offline facilities. The trigger is approximated in this analysis by a threshold cut, which requires an isolated energetic lepton ($p_T \geq$ 20GeV/c muon or $p_T \geq$ 25GeV/c electron) within the central region ($|\eta| < 2.5$). These requirements are more stringent than set out in the ATLAS Physics Technical Design Report (TDR) [39], where the cuts were 6 GeV/c and 20 GeV/c for the muon and electron respectively. If one looks at the shape of the lepton transverse momentum in fig.6.2(a), it is apparent that the raising of threshold levels since publication of the TDR will cut an additional 5-10% of signal events. In total (given that 5% of events are cut at generator level from the plots in fig.6.2) it is estimated that ≈20% of signal events will be missed by the trigger. The pseudorapidity cut will likely have a negligible additional effect, given that those events with $|\eta| >$ 2.5 are very much in the tails of the pseudorapidity plot (see fig.6.2(b)) and most of these will likely be of low transverse momentum anyway. If one now looks at the background plots for the lepton, one sees broadly similar shapes compared to the signal. The semi-irreducible $t\bar{t}b\bar{b}$ background is slightly softer in transverse momentum

and has roughly the same pseudorapidity distribution. Interestingly, the reducible $t\bar{t}jj$ plots show it is harder in transverse momentum, yet wider in pseudorapidity. This is a change from studies such as [55] which have shown similar results to the $t\bar{t}b\bar{b}$ plots, the difference in this analysis being the use of MC@NLO which tends to predict harder event systems.

Looking now at the plots for b-quarks originating from t-quarks in fig.6.2(c, d), one sees the signal is harder in transverse momentum than both backgrounds, with the pseudorapidity plots being very similar. However the differences observed are generally only in the moderately high p_T regions, so standard jet energy cuts will not differentiate between signal and background processes. However, moving on to b-quarks from the Higgs boson or from gluon radiation in the $t\bar{t}b\bar{b}$ background (there is no analogue in the $t\bar{t}jj$ channel) in fig. 6.2(e, f), one sees marked differences. Those in the signal have a very similar p_T distribution to the b-quarks from the t-quarks, this being one of the major problems in the combinatorical background which is seen in signal events. However one sees the background has a much softer transverse momentum spectrum and wider pseudorapidity spectrum, which will be helpful in signal/background separation.

6.2.3 Parton Level Results

One of the best ways of finding both the efficiency of a given analysis and the limitations of any analysis on a physics channel, is to take the final state partons as input. One can change these into reconstructed objects in order to see which area is having the biggest effect on efficiency. This is done for the series of plots in fig. 6.3 for the 130 GeV/c^2 Higgs boson signal sample. The process of reconstruction is described in detail in subsequent sections, but to summarise:

- One identifies a trigger lepton, (at least) two light jets and (at least) four b-jets
- Using the missing energy and the W mass as a constraint the leptonic W-

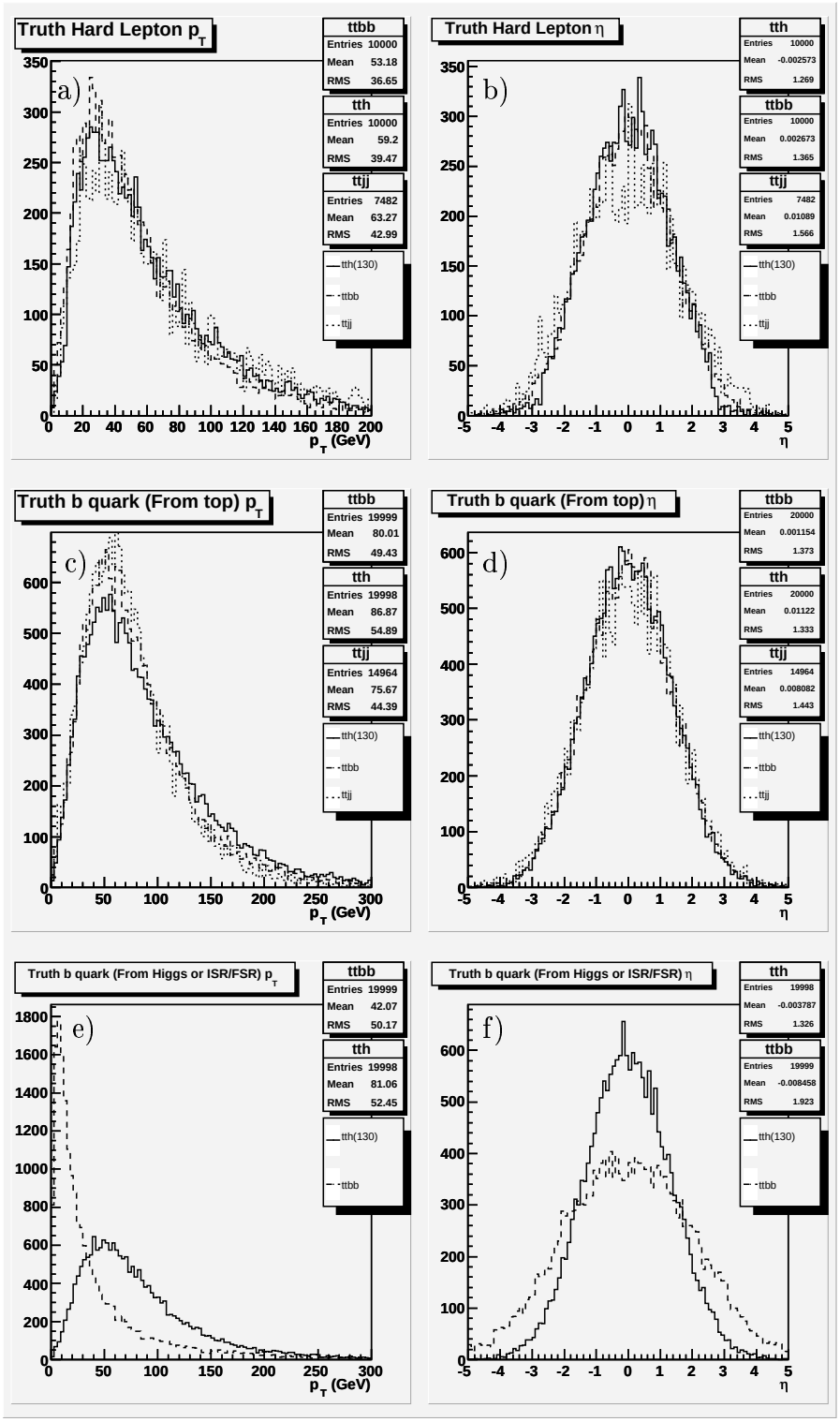

Figure 6.2: *Parton-level truth quantities for signal and background. a) and b) show the truth lepton p_T and η, c) and d) the p_T and η of b-quarks from t-quark decay and e) and f) the p_T and η of b-quarks from Higgs boson decay.*

boson is reconstructed

- A second W-boson is reconstructed from two light jets
- One analyses combinations of the two W-bosons with the b-jets to identify the best $t\bar{t}$ pair
- The two (or two best if there are more) remaining b-jets are combined to form the Higgs boson candidate

Initially for this parton level study, one uses input entirely from truth level, then reconstruction objects are gradually added until all objects are from reconstruction. Looking at fig. 6.3(a) containing only truth objects, the most striking feature is not the delta function mass peak but that a significant percentage $\approx$6% is not in this peak. This essentially means the product of one of the W-bosons with one of the Higgs boson b-quarks, is closer to the t-quark pole mass than using the correct b-quark, an immediate limitation. If one now looks at the result of using reconstructed W-bosons in fig. 6.3(b, c, d) one sees a marked loss in efficiency. This is because the reconstructed object is sometimes mis-measured to the extent that no t-quark could be reconstructed with it (even using the true b-quarks). The effect is more pronounced when using the reconstructed hadronic W, suggesting this is not reconstructed as well as the leptonic W. Finally, when real b-jets are used instead of quarks in fig. 6.3(e, f), one sees that mis-measurement of b-jet energy has the largest effect on efficiency and give rise to a broad Higgs mass peak. It does not seem to matter whether the true (fig. 6.3(e)) or reconstructed(fig. 6.3(f)) W-bosons are used, suggesting the choice of the correct combination is dominated by the b-jets.

6.2.4 Parton→Jet Reconstruction

As a first step to reconstructing the quarks in an event, one can look at the truth level jets. These are jets comprised of the true hadrons which are the output of the

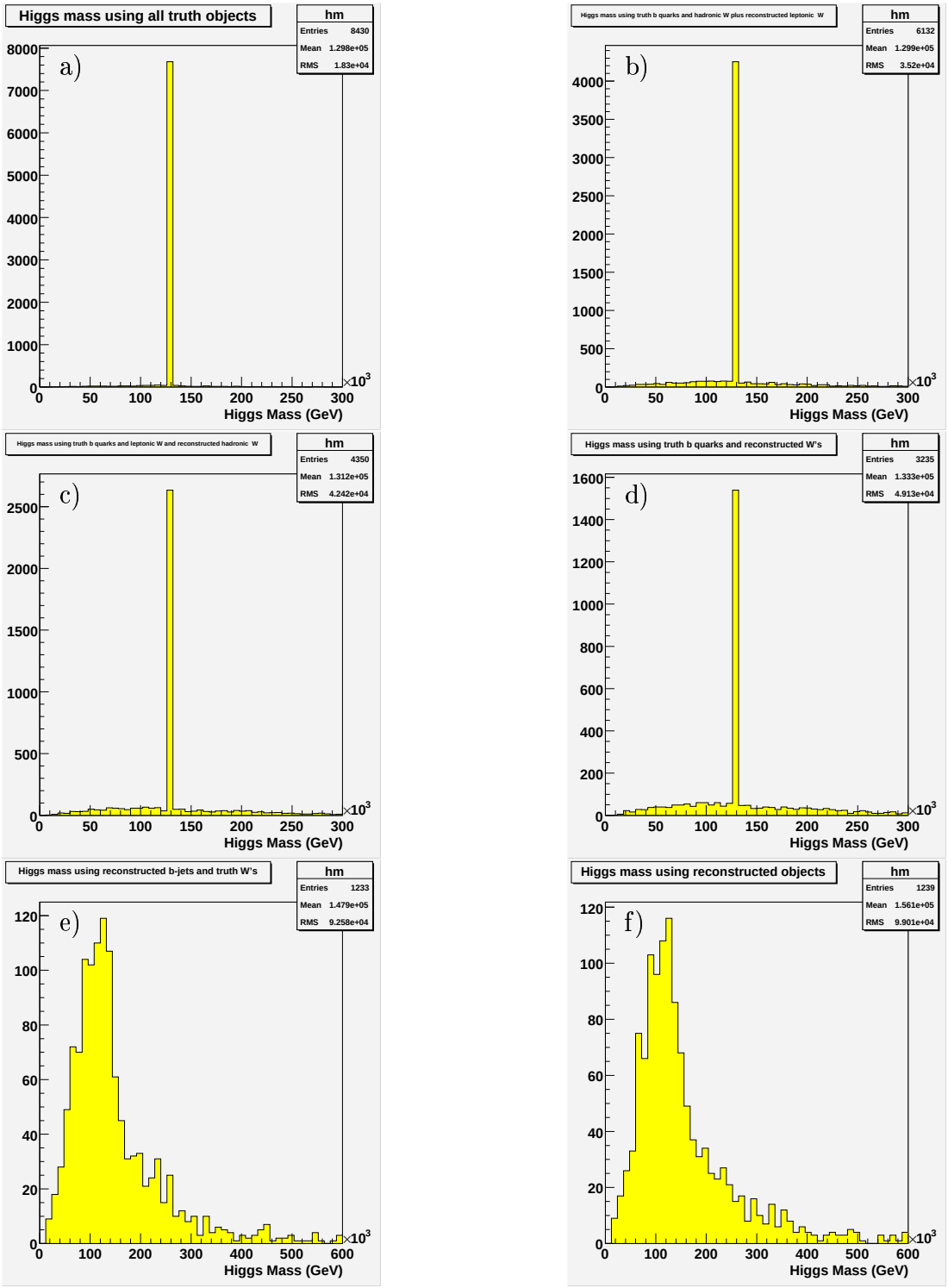

Figure 6.3: *Higgs mass using combinations of truth and reconstructed objects as input to the analysis. a) uses objects (2 W-bosons and 4 b-quarks) entirely from truth, b) uses the reconstructed leptonically decayed W-boson and remainder truth, c) uses the reconstructed hadronically decayed W-boson and remainder truth, d) uses both reconstructed W-bosons and the true b-quarks, e) uses the true W-bosons and reconstructed b-jets and f) uses entirely reconstructed objects.*

Monte-Carlo generator after the hadronisation and final state radiation (FSR) stages, but before detector effects. One would expect the level of degradation in resolution (with respect to the initial parton), to depend on these physical characteristics and also one's choice of jet reconstruction algorithm and relevant parameters. Fig. 6.4 shows the ratio of the energy of the jet (truth level) to the energy of a matched quark, for three choices of jet clustering: cone algorithm with $\Delta\mathrm{R}_{\mathrm{cone}} = 0.7$; cone algorithm with $\Delta\mathrm{R}_{\mathrm{cone}} = 0.4$ and k_T algorithm with R_{cut} parameter 0.45. The matching criteria requires a ΔR_{match} separation between jet and quark of no greater then 0.4. Looking at fig. 6.4(a,c,e) one sees that there is generally a low tail regardless of the choice of algorithm or jet size. The right hand side plots, fig. 6.4(b,d,f), are 'cleaned' in that there is a requirement that there be no neutrinos inside the jet. This reduces the low side tail in all cases and any remainder is likely due to the FSR i.e. hard gluon emission far from the jet centre. This is borne out by the largest cone, with $\Delta\mathrm{R}_{\mathrm{cone}} = 0.7$, having virtually no remaining low-side tail as the cone is large enough to capture these emissions. However this size of cone does have a larger high side tail, as it has a tendency to combine closely separated partons into the same jet. This leads not only to poor resolution, but also low jet multiplicity which makes the cone algorithm with $\Delta\mathrm{R}_{\mathrm{cone}} = 0.7$ unsuitable for reconstruction of this process. Henceforth, whenever the cone algorithm is used in analysis it is with $\Delta\mathrm{R}_{\mathrm{cone}} = 0.4$ unless explicitly stated.

If one now compares the output of the cone algorithm with $\Delta\mathrm{R}_{\mathrm{cone}} = 0.4$ and the k_T algorithm (which has been run with a R parameter of 0.45) in fig. 6.4, one sees broadly similar results. As this is based on the same event sample, the number of entries are directly comparable. One can see the k_T algorithm generally has higher jet multiplicity, around 5% under the quark matched criteria of fig. 6.4. However the peak is sharper when the cone algorithm is used, indicating it is usually better equipped to measure the jet energy. There is also some worth in comparing separately the light and heavier b-quark flavours, shown in figs. 6.5, 6.6. Note the quark matching here is

much stricter, requiring a ΔR_{match} separation of no greater than 0.1,in order to make sure the correct flavour is assigned to the jet. The most obvious aspect of these plots is that losses in b-jets are almost entirely due to neutrinos, whereas light flavours are only marginally affected by these. This is because a b-quark decays semi-leptonically $\approx$30% of the time and is thus far more likely to produce a high energy neutrino than a light flavoured quark.

6.3 Signal Reconstruction

6.3.1 Signal Topology

The final state topology for the $t\bar{t}H, H \rightarrow b\bar{b}$ channel can be multi-fold. Firstly it should be emphasised that it is vital to reconstruct the entire final state. One benefit is that if one can correctly assign the b-jets to their respective t-quarks, the two left over will be the ones from the Higgs boson (one does not know *a priori* the Higgs mass being searched for). Additionally, there are many potential backgrounds one can reject by requiring correctly reconstructed W-bosons and t-quarks (indeed this is why direct Higgs boson production is impossibly difficult to isolate). Of the $t\bar{t}H, H \rightarrow b\bar{b}$ final states possible, the most likely (based on decay branching ratios) would be an eight jet final state with four b-jets and four light-flavoured jets. However, aside from the difficulty in constructing a trigger that will select events such as these (in fact it is unlikely one will exist), this would be a difficult final state to reconstruct. This is because even if one could isolate the signal events from multi-jet QCD backgrounds, there would be a huge number of combinations of W-bosons and t-quarks possible, making it harder to make the correct assignments. A second final state one could analyse is the 'di-lepton' state, where both W-bosons decay to light leptons (muons or electrons and their corresponding neutrino). This would certainly be easier to construct a trigger for, as two isolated leptons is a relatively rare occurrence. However

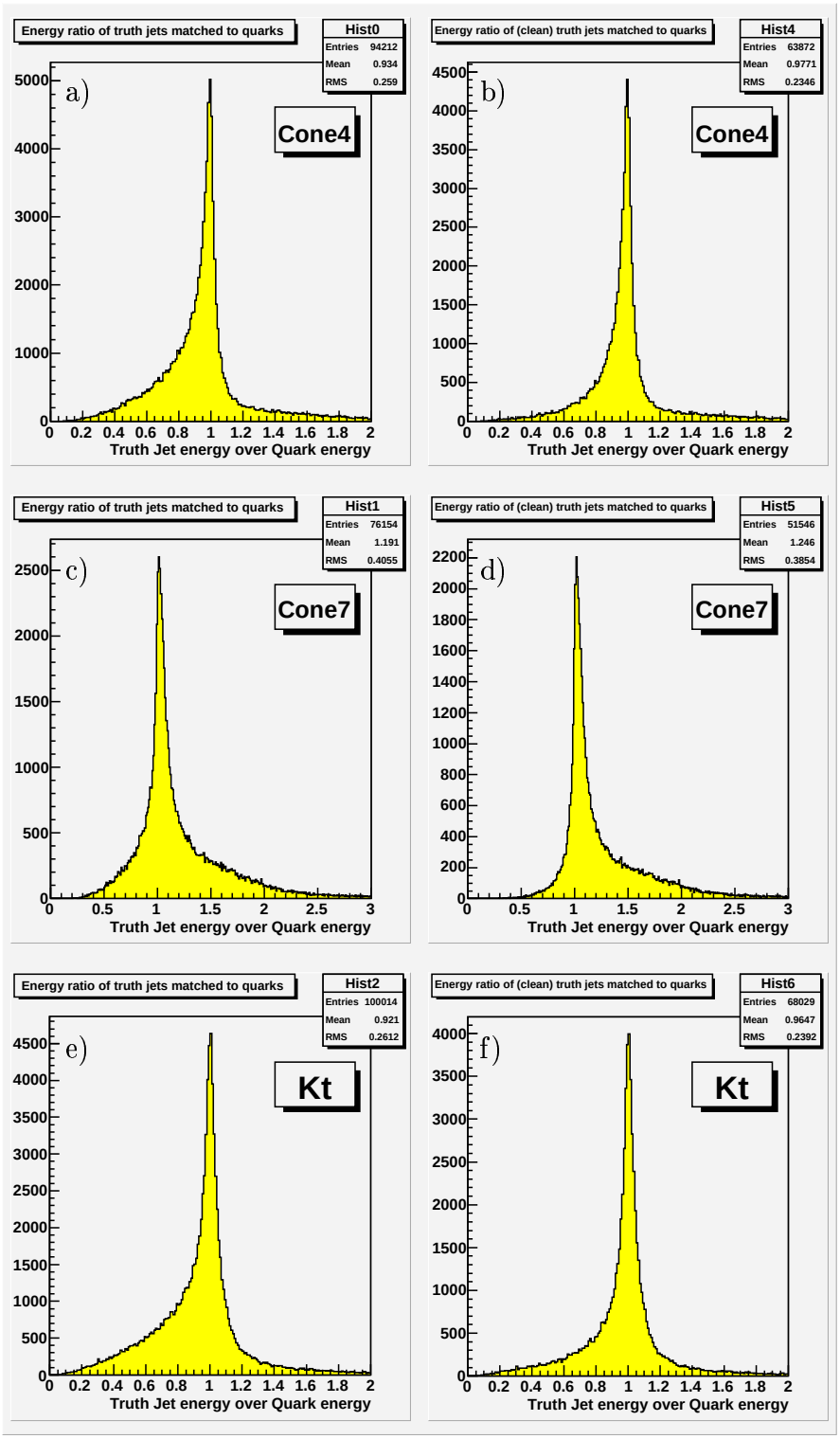

Figure 6.4: *Ratio of the energy of a jet (truth level) to the energy of a quark matched in a 0.4* ΔR_{match} *cone. Three choices of jet clustering are shown: cone algorithm with* $\Delta R_{cone} = 0.7$*; cone algorithm with* $\Delta R_{cone} = 0.4$ *and* k_T *algorithm with* R_{cut} *parameter 0.45. The right-hand side plots have additionally been 'cleaned' in that no neutrino may be contained in the jet.*

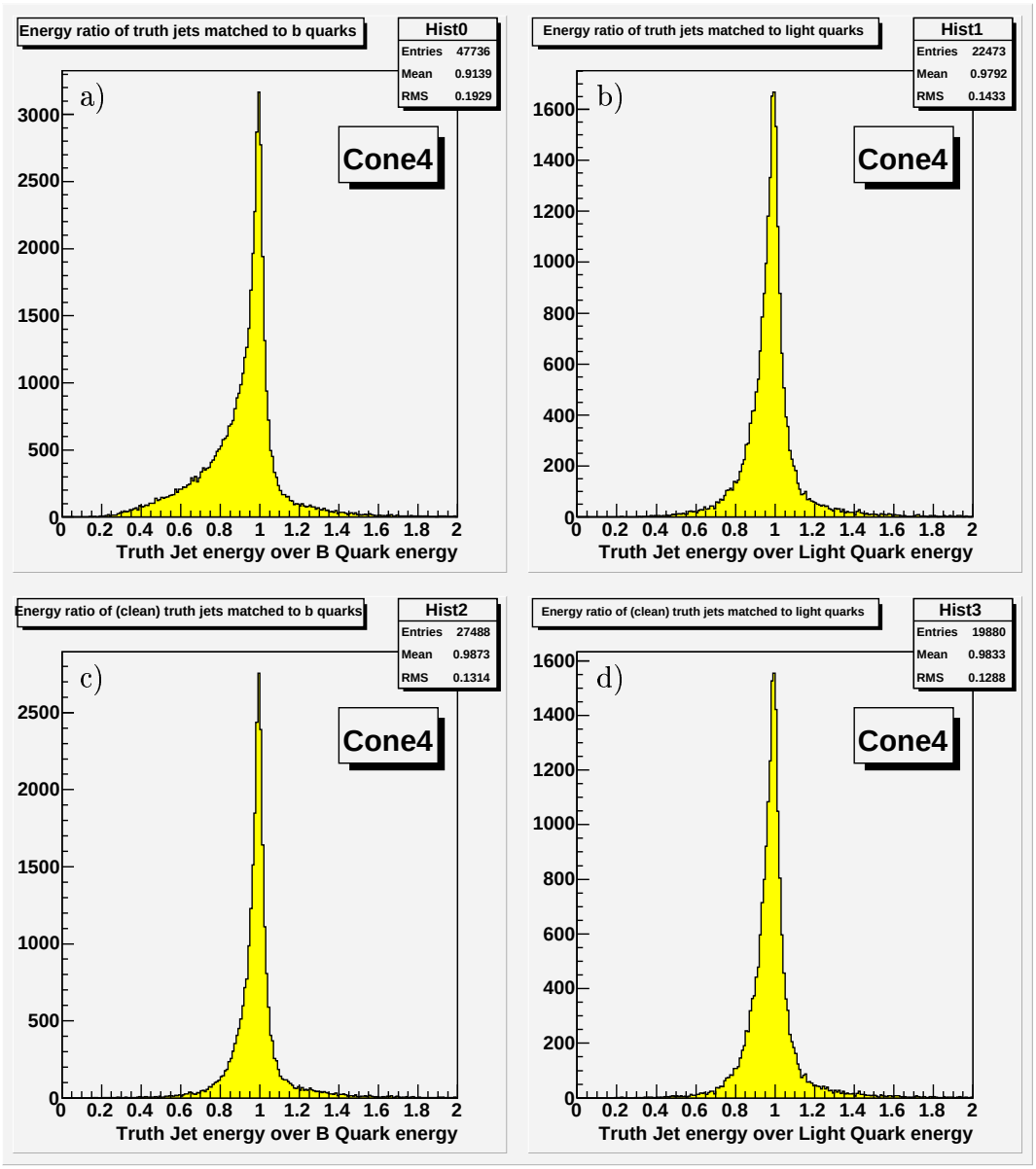

Figure 6.5: *Ratio of the energy of a jet (truth level) to the energy of a quark matched in a 0.1* ΔR_{match} *cone. The cone algorithm is used throughout and the lower plots have an additional requirement that the jet contains no neutrinos. The plots on the left-hand side are for jets matched to b-quarks and the plots on the right-hand side are for jets matched to light quarks.*

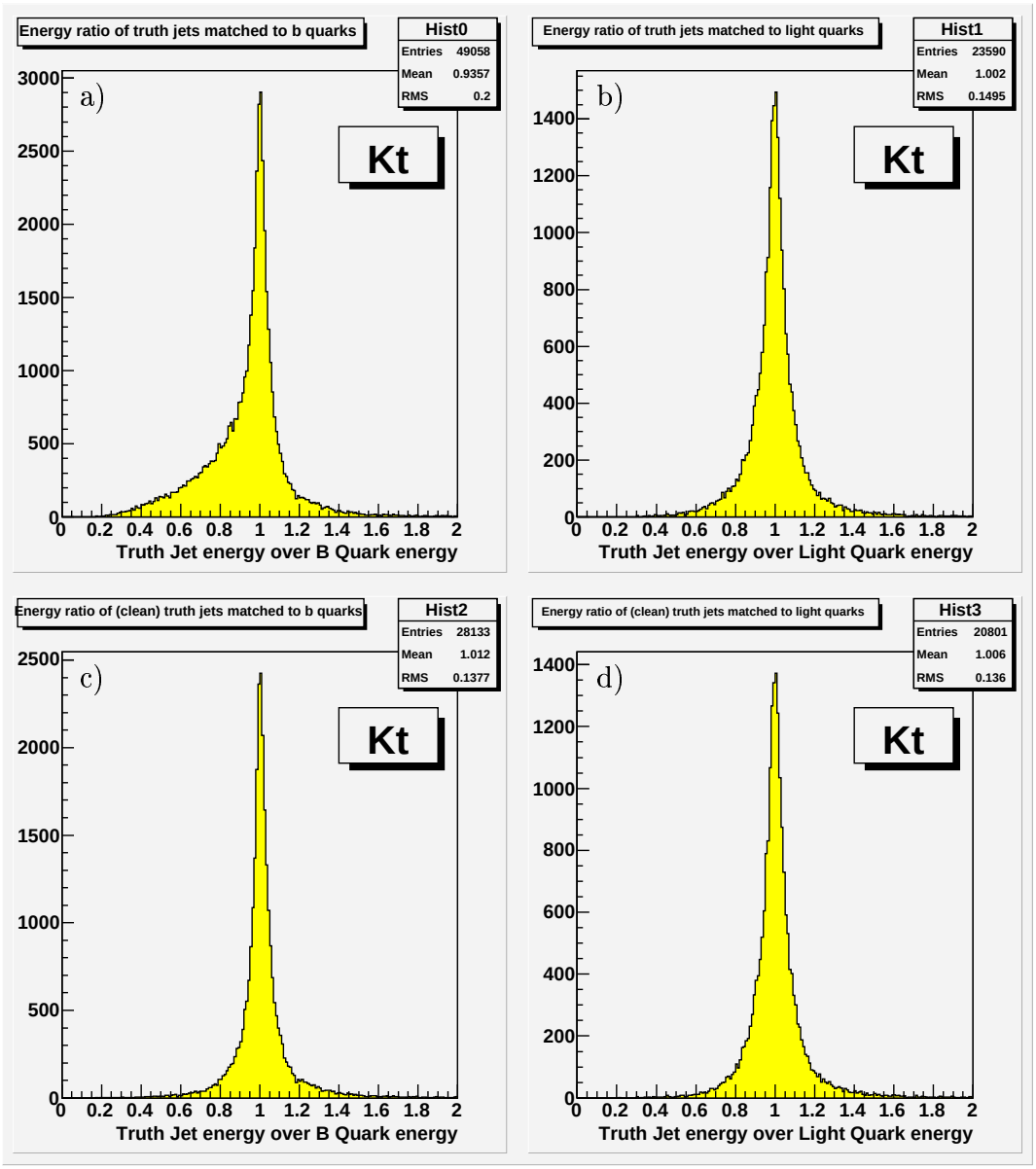

Figure 6.6: *Ratio of the energy of a jet (truth level) to the energy of a quark matched in a 0.1* $\Delta \mathrm{R}_{\mathrm{match}}$ *cone. The* k_T *algorithm is used throughout and the lower plots have an additional requirement that the jet contains no neutrinos. The plots on the left-hand side are for jets matched to b-quarks and the plots on the right-hand side are for jets matched to light quarks.*

this final state has its own problems. Firstly, the probability of this final state is only $\approx 4\%$ which reduces a channel with an already small cross-section even further. Secondly, the final state contains two neutrinos which means that the 4-momentum cannot be unambiguously calculated from the missing transverse momentum. Again this would make the subsequent reconstructions difficult. Taking the above into account, the most promising final state is the 'semi-leptonic' state (see fig. 6.1) which contains four b-jets (two from the Higgs boson and one from each t-quark), two light jets (from one W-boson decay) and one light lepton and corresponding neutrino (from the other W-boson decay).

Final State	1st W decay	Prob.	2nd W decay	Prob.	Total prob.
$b\bar{b}b\bar{b}jjjj$	$W \to q\bar{q}$	0.676	$W \to q\bar{q}$	0.676	45.7%
$b\bar{b}b\bar{b}jjl\nu$	$W \to e\nu_e, \mu\nu_\mu$	0.216	$W \to q\bar{q}$	0.676	29.2%
$b\bar{b}b\bar{b}jj\tau\nu$	$W \to \tau\nu_\tau$	0.108	$W \to q\bar{q}$	0.676	14.6%
$b\bar{b}b\bar{b}l\nu l\nu$	$W \to e\nu_e, \mu\nu_\mu$	0.216	$W \to e\nu_e, \mu\nu_\mu$	0.216	4.5%
$b\bar{b}b\bar{b}l\nu\tau\nu$	$W \to e\nu_e, \mu\nu_\mu$	0.216	$W \to \tau\nu_\tau$	0.108	4.5%
$b\bar{b}b\bar{b}\tau\nu\tau\nu$	$W \to \tau\nu_\tau$	0.108	$W \to \tau\nu_\tau$	0.108	1.1%

Table 6.2: *Probability of the possible final states of $t\bar{t}H, H \to b\bar{b}$.*

6.3.2 Pre-Selection

For the semi-leptonic decay mode, one first requires an isolated high-p_T lepton, which will be the trigger during operation. The output of the reconstruction algorithms will contain many leptons and it is important (for later parts of the reconstruction) to identify the correct one. The average number of final state electrons found is around 25 per event as seen in table 6.3, which shows the overall all results for about 19000 events. This number is first reduced by kinematic cuts, which requires the electron to have reconstructed $p_T \geq 25$ GeV/c, this being the approximate cut-off trigger

threshold. The next cut is an 'author' cut; there are two ways of reconstructing electrons and an author package for each of these methods. EGAMMA [56] takes identified clusters of electromagnetic energy in the calorimeter and tries to find a track which suggests that deposit was left by an electron. SOFTE [57] takes an inner detector track and looks for energy clusters in the calorimeter which match that track. In general, a high energy lepton would be found by both of these packages (but the EGAMMA identification takes precedence) and the SOFTE will find some extra low energy electrons. Whilst this is useful in multi-electron final states (as one electron may be of low energy and use of the package increases efficiency), in this channel it just tends to decrease purity with little increase in efficiency. Therefore only the EGAMMA electrons are used.

Next there is an isolation cut, requiring no greater than 15 GeV of energy in a ΔR cone of size 0.45 surrounding the electron, which serves to remove electrons that are really part of jets. Finally a bit-wise cut method called 'isEM' [58] is used to clean the sample further. There are four cluster based cuts, such as energy in sampling layers and energy identified as hadronic in nature. Then three track based bits are set depending on e.g. number of silicon hits compared to the impact parameter and the energy-momentum ratio, 'EoverP'. The net result is that 0.9 % of electrons pass all cuts and of the remaining sample, 99 % are the ones which came from the W-boson decay, as shown in fig. 6.7(a).

For muons one can again apply some simple cuts to reduce the excess coming from soft b-decays and other backgrounds. As before one first cuts on the transverse momentum value, to simulate the trigger which reduces the number of muons by nearly 90%, see table 6.3. This still leaves an average of 1.5 muons per event, when one expects 0.5 (as the W-boson decays to an electron half the time). A further reduction is made by cutting on χ^2, which is a measure of how well the extrapolated muon chamber tracks and inner detector tracks are matched. This still leaves a

Electrons			
Cut	N_{ElEC}	Rel. ϵ	Abs. ϵ
-	539540	-	-
$E_T \geq 25$ GeV, $\|\eta\| < 2.5$	132814	24.61%	24.6%
"author = Egamma"	21988	16.61%	4.1%
Isol ($\Delta R < 0.45$) $E_T^{ISOL} < 15$ GeV	6414	29.2%	1.2%
isEM(calo) 0x7FF	5271	82.1%	1.0%
isEM(track) 0x7FF	4955	93.9%	0.9%
Muons			
Cut	N_{MUON}	-	
-	206530	Rel. ϵ	Abs. ϵ
$E_T \geq 20$ GeV, $\|\eta\| < 2.5$	23604	11.4%	11.4%
$\chi^2/NDOF < 20$	21801	92.2%	10.6%
Isol ($\Delta R < 0.3$) $E_T^{ISOL} < 50$ GeV + Rel. Isol > 0.6	7331	33.6%	3.6%

Table 6.3: *Cut flow for selecting trigger candidates for 20k ttH(120) events. For electrons there are kinematic cuts on E_T and η and an isolation cut on the transverse energy, E_T^{ISOL}, in a ΔR cone of size 0.45. The electrons are taken only from the* EGAMMA *package (clusters looking for a matched track), whilst ones from the* SOFTE *package (tracks looking for a matched cluster) are discarded. There is a final bit-wise cut called 'isEM' which cuts on shower shape variables in the calorimeter sampling layers and track variables, such as number of inner detector hits. For muons similar kinetmatic cuts are applied followed by a cut on the $\chi^2/NDOF$ to ensure the muon track is a good fit. The isolation cut is more complex than for the electron, requiring both a flat E_T cut in a ΔR cone of size 0.3 and a cut that ensures the muon has sufficient energy relative to the isolation energy (see fig. 6.8).*

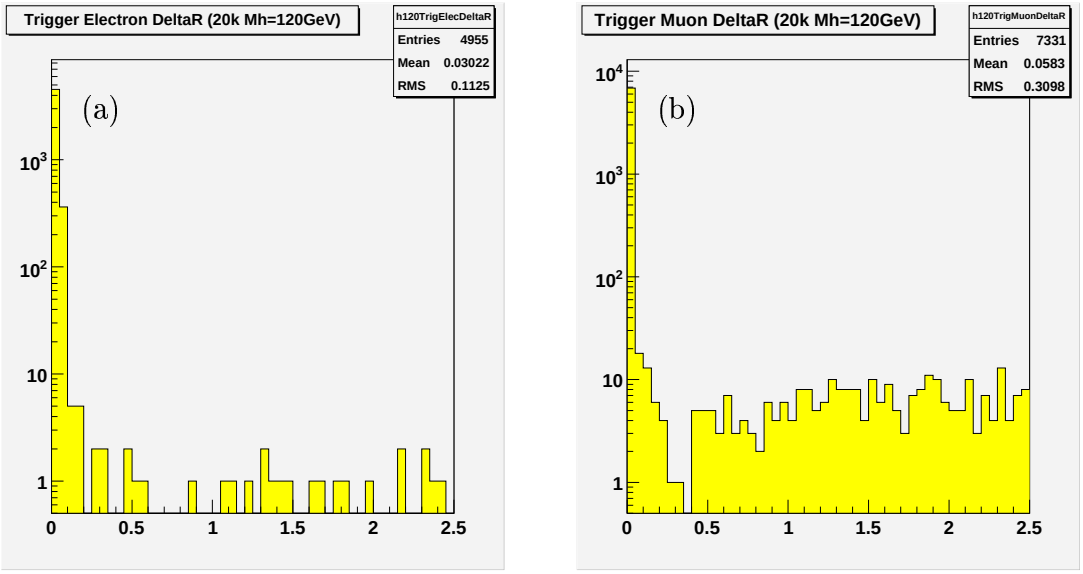

Figure 6.7: ΔR *between the high* p_T *lepton trigger candidate and the true lepton in 20k* $t\bar{t}H, H \to b\bar{b}$ *events. The left-hand side shows electrons and the right-hand side muons, with both plots haing a logarithmic scale.*

large excess which are very likely to be muons originating from jets. Therefore one looks at the muon energy as a fraction of the isolation energy (the energy in a cone surrounding the muon), see fig. 6.8. In this plot all muons found after the χ^2 cut are tested against the true muon (assuming the W-boson decayed to a muon), to see if it is genuine. From this one can see that no simple cut on isolation energy, as was applied for electrons, would eliminate a large fraction of background muons without removing excessive fractions of correct signal muons. Instead we apply a relative isolation cut at 0.6 (together with a flat cut for Isol $E_T < 50$ GeV within a $\Delta R = 0.3$ cone), to select the best region. From the results in fig. 6.7(b), one can see that excellent purity is once again achieved, though not quite to the level of the electron (of the remaining 3.6 %, about 95 % are the correct one). Note however, that muon efficiency is much higher, which is probably a result of the slightly more generous p_T cut and no equivalent of the 'isEM' cut. The final aspect which needs to be dealt with is events where, even after all these cuts are applied, where both an

electron and a muon are found. As the plots in fig. 6.7 suggest, electrons are of the higher purity and if one looks at the events where both are found (only 1 % of events, see fig. 6.9) one sees it is usually correct to take the electron.

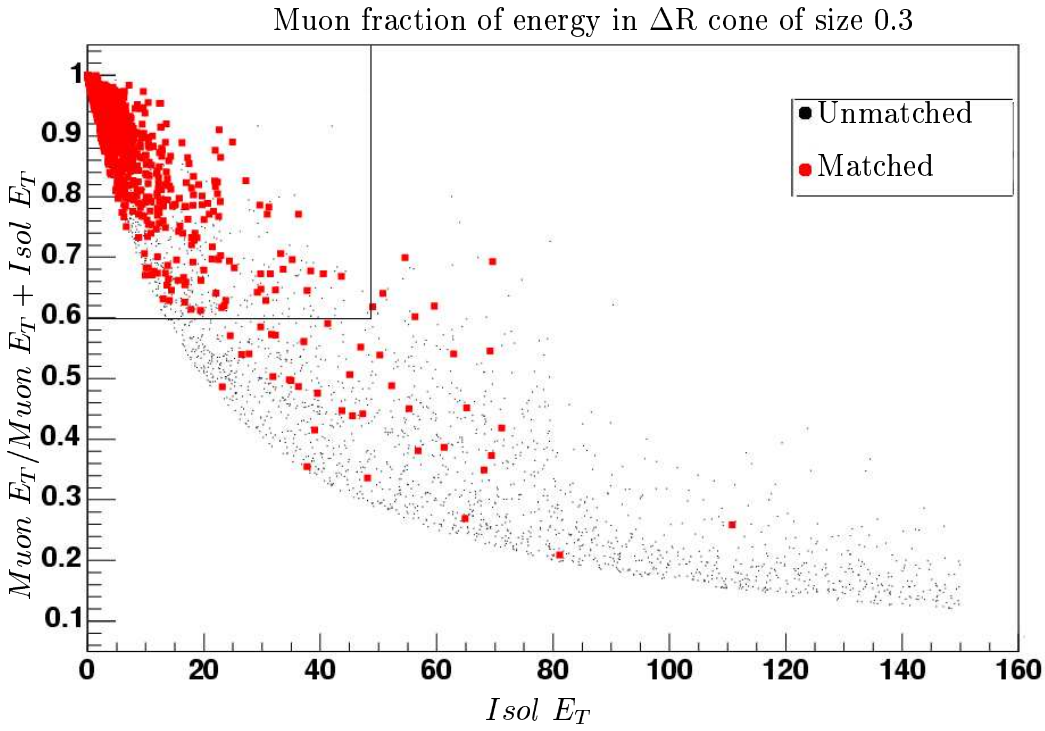

Figure 6.8: *Muon transverse momentum as a function of the transverse momentum in a surrounding cone. The x-axis is the transverse energy in a ΔR cone of size 0.3, whilst the y-axis is the fraction of the muon transverse energy over the sum of muon and isolation energy. Candidates which are matched in a ΔR cone of size 0.1 to the trigger muon are shown separately from those that are spurious i.e. unmatched. To cut the spurious muons, a region is selected (shown in the box in the top left) corresponding to isolation $E_T < 50$ GeV and muon fraction > 0.6.*

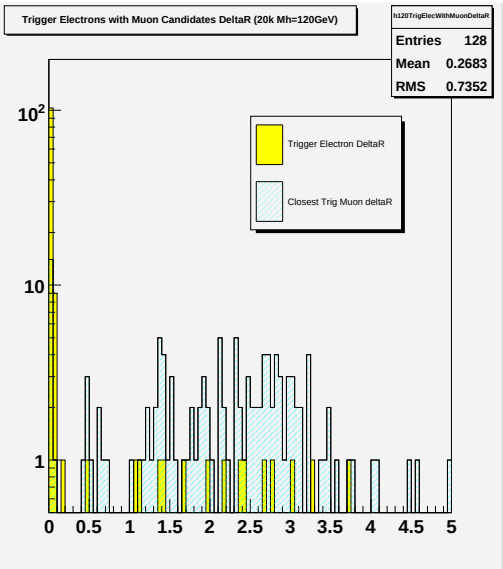

Figure 6.9: *ΔR from the high p_T lepton trigger candidate to the true lepton in $t\bar{t}H, H \to b\bar{b}$ events where both an electron and muon are found.*

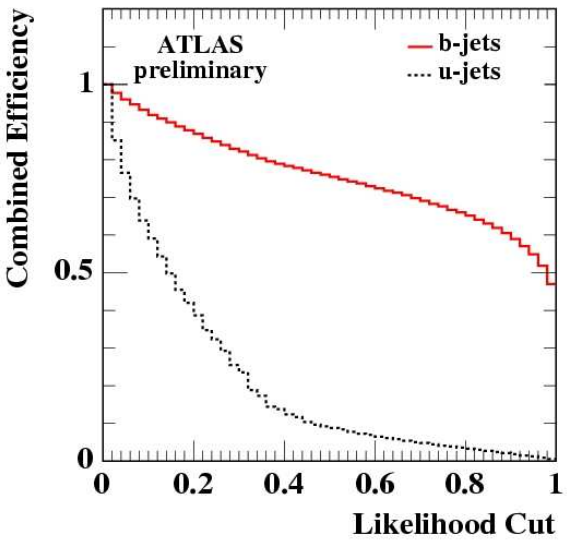

Figure 6.10: *Jet tagging efficiencies as a function of the combined likelihood cut*

The next stage in pre-selection is jet selection. This only comprises kinematic cuts, largely to remove spurious jets created by the underlying event and beam fragments, and a likelihood cut to divide the collection into b-jets and light jets.

- a jet requires $E_T > 20$ GeV and $|\eta| < 2.5$
- a b-jet requires a tagging likelihood > 0.9
- the remainder are classed as light jets, but may excluded if overlapping with other objects e.g. electrons

The background removal (in pre-selection) is largely achieved via cutting on the number of b-jets, because four are required for complete event reconstruction. In the full simulation, jet tagging is the convolution of a number of different taggers, each of which returns a likelihood between 0 and 1 (of the jets probability of originating from

a b-quark). The result is called the combined likelihood (lhd) and depending on where one cuts on this function, one can achieve different rates of efficiency for correct b-jet identification and light jet rejection (see fig. 6.10 or [59], noting that detailed analysis of this function lies outside the scope of this work). In the fast simulation, jets are initially perfectly tagged, then randomly mis-tagged according to a chosen scheme, which should reflect the rates achievable by the full simulation. In ATLAS, this is usually set to a random b-jet efficiency (ϵ_B) of 0.6, with a c-jet rejection factor (R_C) of 10 and light jet rejection factor (R_L) of 100. Looking at fig. 6.10, one sees that a likilihood cut at 0.9 would achieve numbers similar to this, for the signal events and AcerMC backgrounds.

The results for the signal events are shown in figs. 6.11 and 6.12, showing the number of b-jets passing cuts for increasing generated Higgs mass and for the cone and k_T jet algorithms. As expected, the higher Higgs mass results in higher energy jets across the board. Also one notes the mean number of b-jets found is largely in line with an average efficiency of 0.6, with some allowance for kinematic losses. This can be seen by summing the probabilities for a given number of jets e.g. the fraction of events with all all four correctly tagged b-jets should be $0.6^4 = 0.13$. Comparing the jet algorithms, one sees the k_T algorithm has a higher mean number of jets, probably because it is more efficient at collecting swept-out energy depositions, which would not be large enough to be a seed for a cone jet.

Fig. 6.13 shows the background results, compared with the signal (at a Higgs mass of 120 GeV/c^2). One sees the number of jets is higher in the signal, by as much as an average whole extra jet over the $t\bar{t}jj$. However that sample is actually an inclusive collection where there may not be six final state partons as in the signal sample. This is not the case in the $t\bar{t}b\bar{b}$ sample, but recall that in fig. 6.2 c), e) the parton energies are lower compared to the signal. In particular, the b-jets from the Higgs boson have a much harder p_T spectrum than the additional ones in the AcerMC sample. This has a dramatic effect on the b-jet efficiency in Fig. 6.13, with far fewer jets in the

$t\bar{t}b\bar{b}$ sample passing the likelihood cut. Of course, with only two genuine b-jets, the mean number is even lower in the $t\bar{t}jj$ sample. The overall pre-selection efficiencies are shown in table 6.4. The result is that (in e.g. k_T) 5% of the signal sample remains and is eligible for reconstruction, compared with 1.9% of the $t\bar{t}b\bar{b}$ and just 0.043% of the $t\bar{t}jj$ samples.

Channel	Cut	rel. efficiency (%)		abs. efficiency (%)	
		Cone4	Kt	Cone4	Kt
$t\bar{t}H(120)$	$N_{LEP} \geq 1$	60.16	60.16	60.16	60.16
	$+ N_{JET} \geq 6$	54.57	66.89	32.78	40.17
	$+ N_{BJET} \geq 4$	11.77	12.54	3.86	5.00
$gg \to t\bar{t}b\bar{b}$	$N_{LEP} \geq 1$	61.55	61.55	61.55	61.55
	$+ N_{JET} \geq 6$	39.73	49.53	24.45	30.48
	$+ N_{BJET} \geq 4$	5.98	6.22	1.46	1.90
$t\bar{t}jj$	$N_{LEP} \geq 1$	55.0	55.0	55.0	55.0
	$+ N_{JET} \geq 6$	35.84	37.52	19.72	20.81
	$+ N_{BJET} \geq 4$	0.166	0.207	0.033	0.043

Table 6.4: *Pre-selection efficiencies for signal and background. Here N_{LEP} is the no. of isolated leptons as defined in table. 6.3. N_{JET} and N_{BJET} are those jets included by the kinematic cuts above, separated by their jet tagging likelihood value.*

6.3.3 Trigger Selection and Jet Corrections

As was shown in the previous section, it is possible that one can end up with several trigger candidate leptons after all cuts. It was also shown that it is usually correct to take the electron if both an electron and muon are present. However, if more than one good quality muon is left passing the pre-selection cuts there is no obvious way

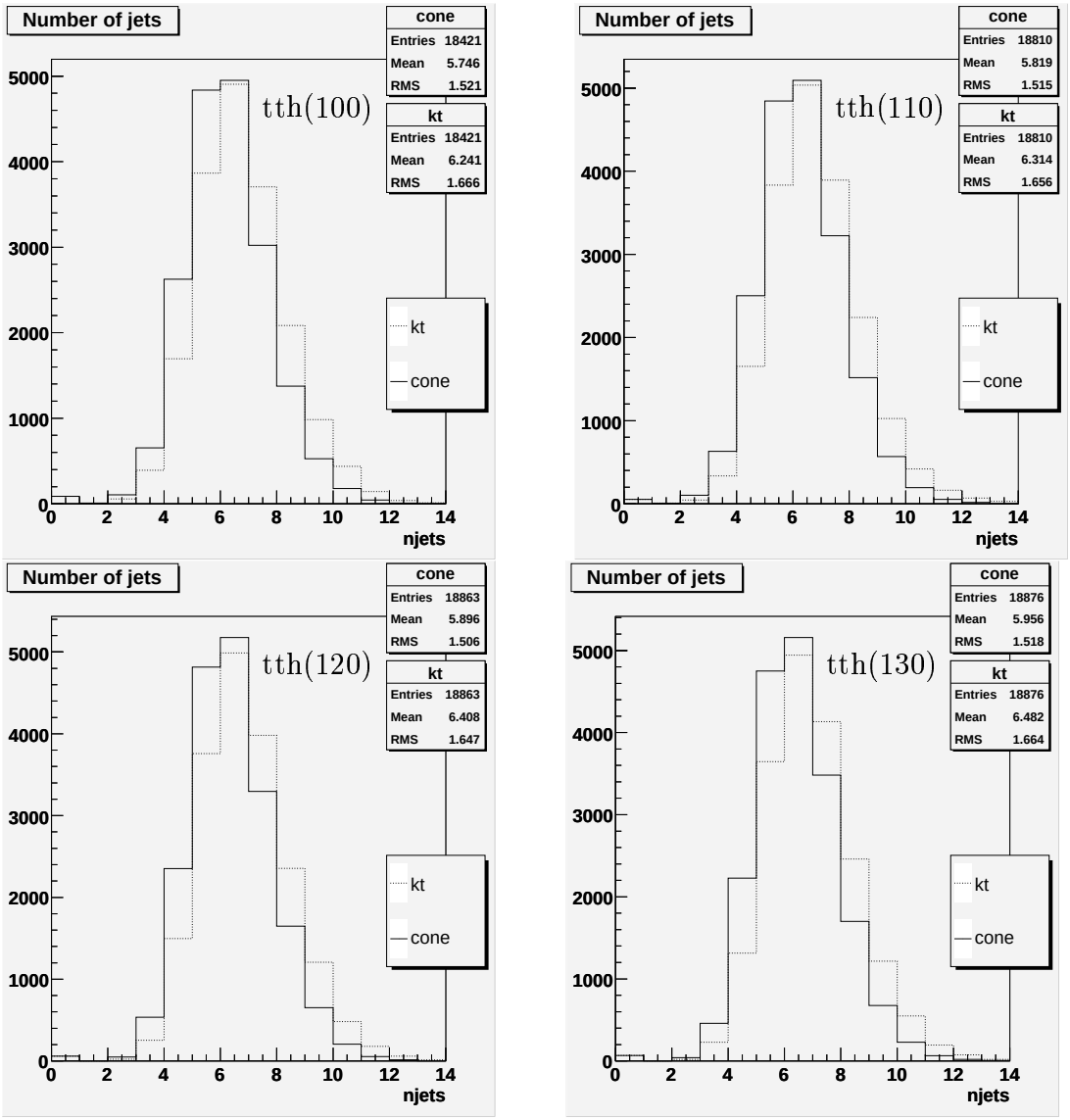

Figure 6.11: *Number of jets in the signal passing threshold cuts. One sees higher means as the Higgs mass increases and that the k_T algorithm has higher jet multiplicities than the cone algorithm.*

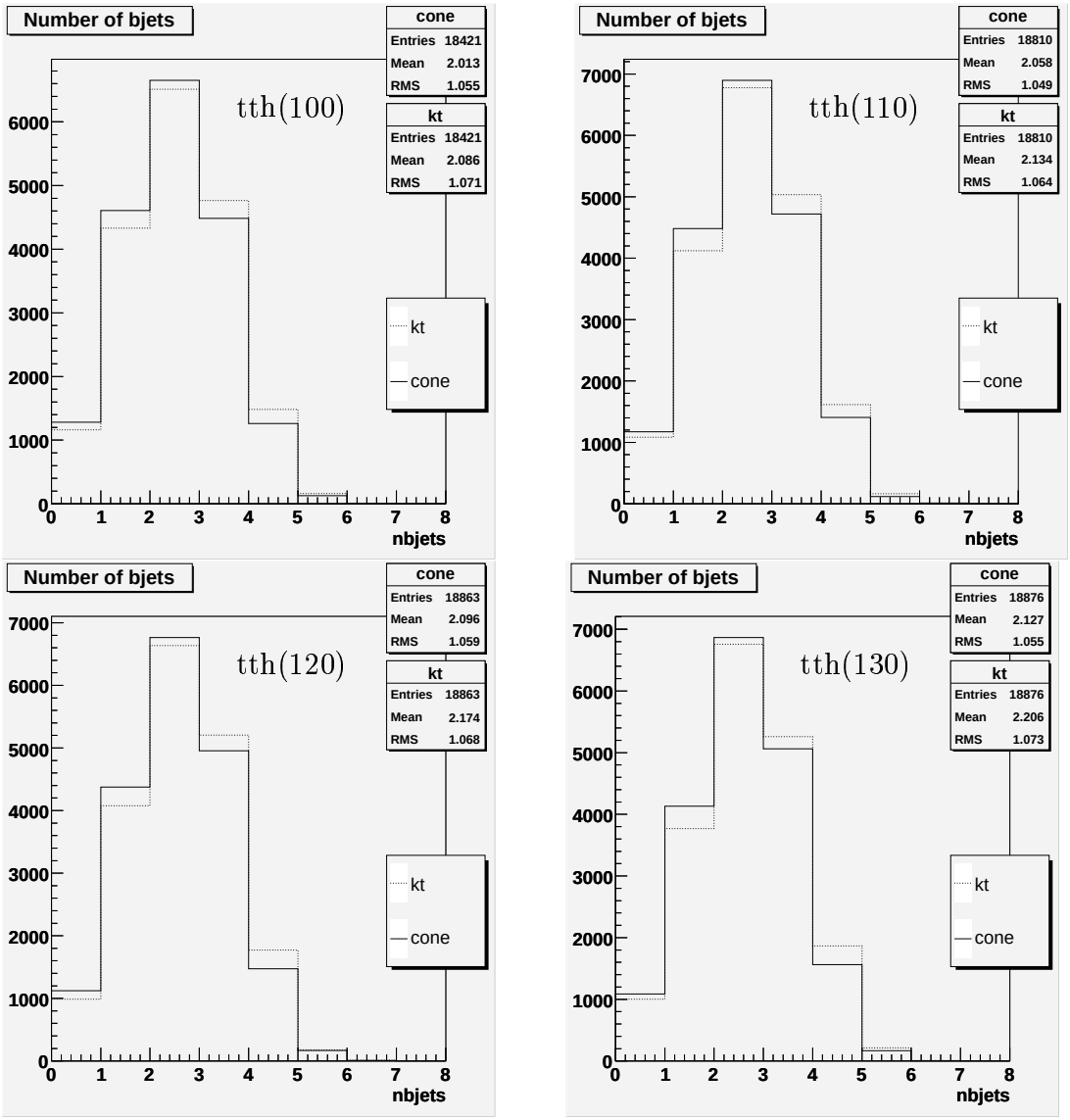

Figure 6.12: *Number of b-jets in the signal passing threshold cuts. The numbers are broadly in line with those expected assuming an average efficiency of 0.6 and some reduction for kinematic cuts.*

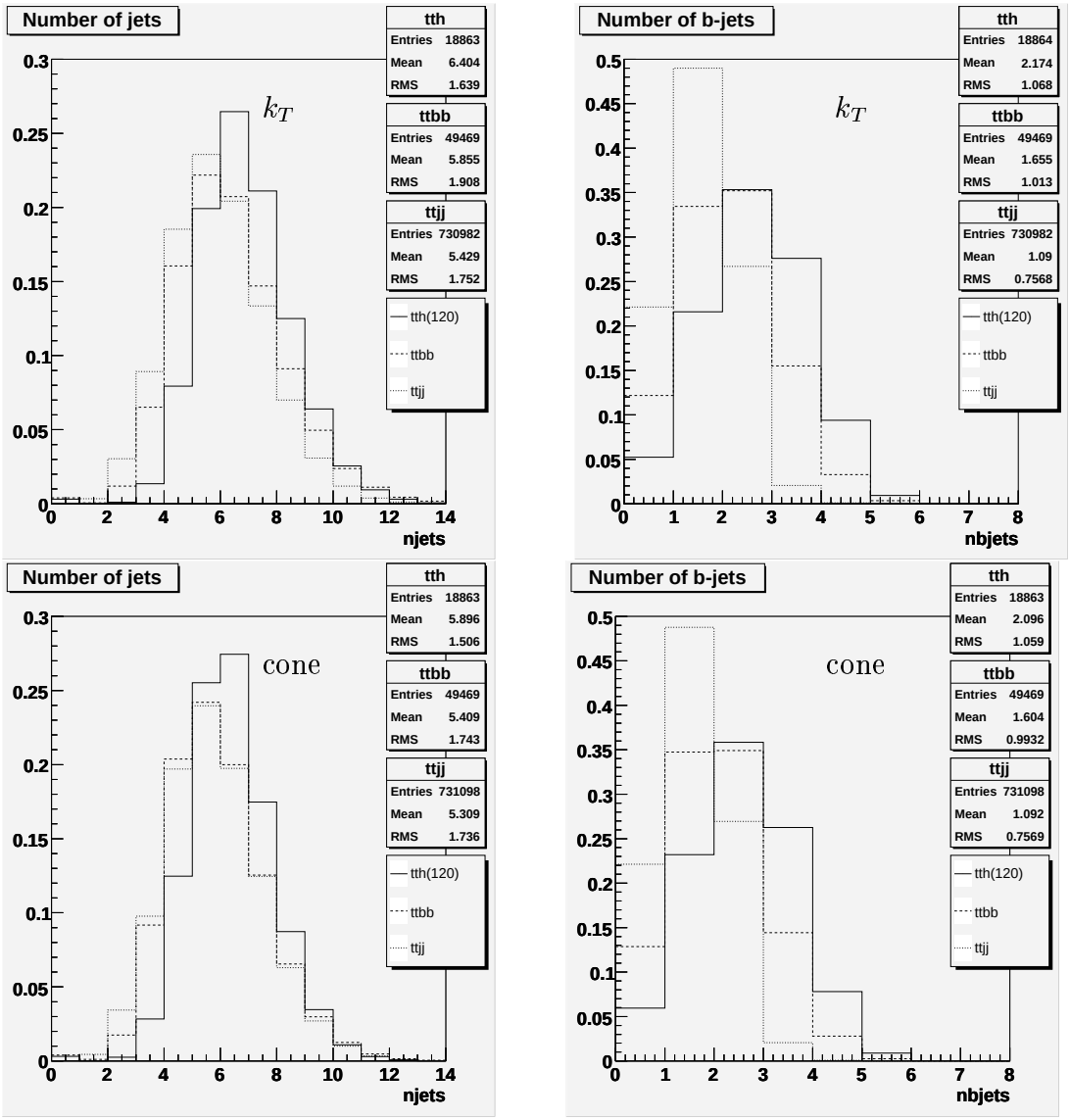

Figure 6.13: *Number of jets in the signal and backgrounds passing threshold cuts. The most striking aspect is that few $t\bar{t}b\bar{b}$ events have a b-jet multiplicity comparable to the signal.*

to choose which is correct. In this case the EventView framework (see §5.4) allows the analysis to split into multiple streams, in which each muon is considered to be the trigger. Naturally the other muon(s) must have a source, so (in the stream where it is not considered to be the trigger) it is either spurious, or part of a jet from one of the quarks. Recalling in §6.2.4 (and in particular fig. 6.4) we saw that in a large number of events much of the jet energy is lost in semi-leptonic b-decays. Although this could happen as part of the decay chain of a light quark, it is more likely this would occur in jets containing B-mesons i.e. b-jets from the t-quarks or Higgs boson (see figs. 6.5 and 6.6). With this is mind, muons which are not the trigger in a given stream are tested to see if they are within $\Delta R < 0.4$ of a b-jet and if so are added to the jet's energy. If they are within range of multiple b-jets, the muon(s) are added to the closest. However, it is not just non-trigger (in an event stream) muons to which this applies, all (or a large fraction) of the muons previously cut can be considered for this. The cuts for these b-decay candidates are much looser (5 GeV energy requirement, $\chi^2/NDOF < 50$ and no isolation cuts) because the aim is only to exclude spurious muons which are not part of the event. Fig. 6.14 shows the effect of adding in these muons, for both the cone and k_T algorithms.

Figs. 6.14 a), c) show the raw reconstructed jet and figs. 6.14 b), d) show those with muons added. One sees a shift in the mean of about 0.04 with a slight improvement in RMS. Note that the k_T algorithm has a better starting point because it is less likely to miss particles due to the 'out of cone' effect. Of course the muon is (on average) only one part of the energy lost in the semi-leptonic b-decays, the rest being in the neutrino. Some effort was made to find a way to correct for the neutrino. First note that the actual missing energy measured in the event is assumed to be from the neutrino in the hard process. This will likely be of higher energy than those from subsequent semi-leptonic b-decays. There is therefore no way to directly estimate the soft neutrino momentum (although if it could be found another way, it may

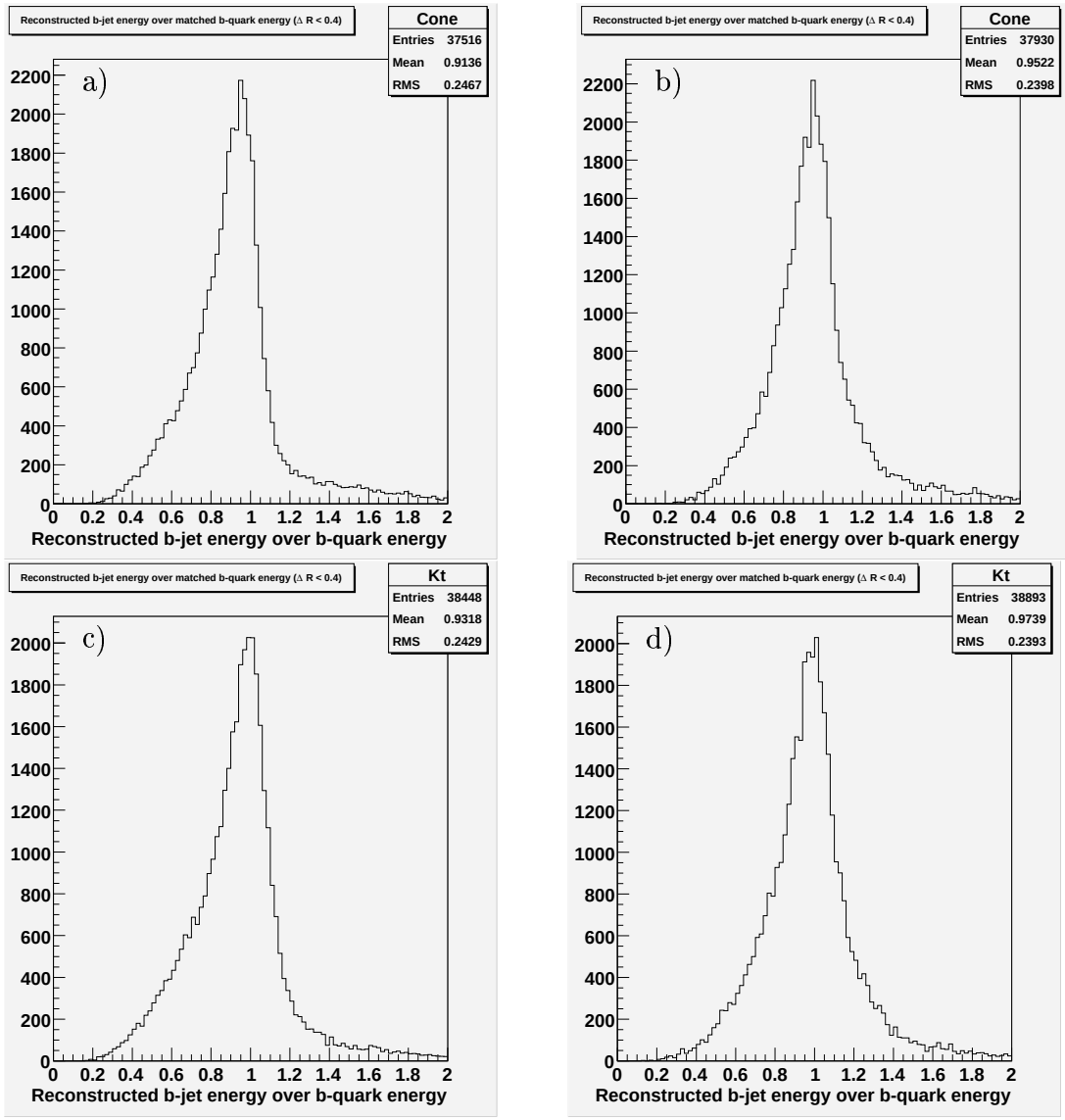

Figure 6.14: *Energy resolution of reconstructed b-jets over b-quarks from the hard process, having been matched in a ΔR cone of 0.4. The left hand side shows the raw jets, while the right shows those with muons added to improve the resolution.*

improve resolution for the hard process neutrino). A viable approach is to look for a correlation between the muon and neutrino energy. True muon and neutrino pairs are matched (within $\Delta R = 0.2$) and the ratio of their energies is plotted. However the ratio turns out to be unpredictable to a large extent, although the peak is at 1, which would allow the crude approximation of setting the neutrino energy to equal the muon energy. The justification for and results of doing this are shown in fig. 6.15, where one sees that whilst the mean of the ratio of energies increases, the overall effect is really just to push entries into the higher tail (note the RMS is not as good as in fig. 6.14 d)). Another technique which was attempted relied on knowledge of the shower-initiating quark's mass. If a b-quark fragments into a jet and one correctly collects and measures all the particles, the invariant mass of the jet will be slightly above the B-meson mass (≈ 5.3 GeV/c^2). Of course we do not expect to have collected the invisibles, so the jet 4-momentum will be reduced by the neutrino 4-momentum. Added to this constraint, the neutrino is assumed to be close to the muon (and jet centroid), so the ratio of neutrino to muon momentum should be the same for each of the 4-momentum components. One solves then for a constant term to scale the muon momentum by, such that the resultant neutrino (when added to the jet) returns the expected jet mass. Unfortunately, this method was ill-behaved i.e. it was subject to very large shifts in predicted neutrino energy for very small changes in input parameters and therefore proved unworkable. Given the lack of success of the above approaches, no correction for the neutrinos is made in future results.

This concludes the preparatory stage of the analysis. The purpose of this was to identify a clean lepton trigger and correctly identify the jets associated with the hard process quarks. Comparisons between cone and k_T jet clustering algorithms were made during the course of this and between the acceptance expected for signal and background. Corrections are also made to b-jets to account for energy lost in semi-leptonic decays. The next sections begin to reconstruct the event, starting with the W-bosons and to begin the one which decays leptonically.

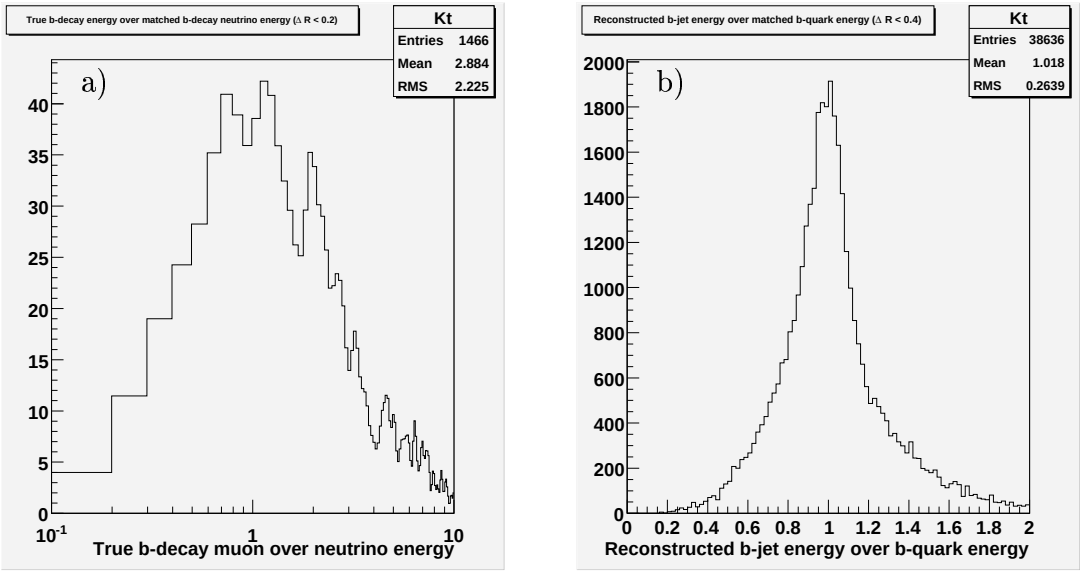

Figure 6.15: *The left hand side shows the energy ratio of the muon and neutrino from a semi-leptonic decay within a b-jet. The right hand side shows b-jets with muons added twice based on the justification that the peak of the left-hand plot is close to 1.*

6.3.4 Leptonic W

The first step on the way to reconstructing the t-quarks is W-boson reconstruction and we start with the leptonically decaying W-boson. This is a two body decay, one of which is a neutrino which will not be seen. However, as all other objects in the event are known (assuming no other neutrino producing decays) we can attribute the measured missing transverse energy to this neutrino. Given the very good missing E_T resolution of ATLAS, one can assign the x and y components with a degree of confidence. The problem is that missing P_z is not measurable as energy is lost down the beam-pipe, so this component of the neutrino's momentum cannot be measured directly. Fortunately the W-boson pole mass and lepton 4-momentum are known and the neutrino energy can be written solely in terms of its momentum components (assuming it is massless). This allows one to solve for the longitudinal component of

the momentum (see e.g. [39], section 19.2.4.3). This 'W mass constraint' method to determine P_{ν_z} is explained next:

$$\begin{aligned} M_W^2 = E_W^2 - \underline{P}_W^2 = (E_l + E_\nu)^2 - (\underline{P}_l + \underline{P}_\nu)^2 \\ = (E_l + E_\nu)^2 - (P_{\nu_x} + P_{l_x})^2 - (P_{\nu_y} + P_{l_y})^2 - (P_{\nu_z} + P_{l_z})^2 \end{aligned} \tag{6.1}$$

$$\begin{aligned} M_W^2 + (P_{\nu_X} + P_{l_X})^2 + (P_{\nu_Y} + P_{l_Y})^2 = E_l^2 + E_\nu^2 + 2E_l E_\nu - P_{l_Z}^2 - P_{\nu_Z}^2 - 2P_{l_Z} P_{\nu_Z} \\ = E_l^2 - P_{l_Z}^2 + P_{\nu_X}^2 + P_{\nu_Y}^2 + 2(E_l E_\nu - P_{l_Z} P_{\nu_Z}) \end{aligned}$$

$$i.e.\ \frac{M_W^2 + (P_{\nu_X} + P_{l_X})^2 + (P_{\nu_Y} + P_{l_Y})^2 - E_l^2 + P_{l_Z}^2 - P_{\nu_X}^2 - P_{\nu_Y}^2}{2} = (E_l E_\nu - P_{l_Z} P_{\nu_Z})$$

All quantities on the LHS can be measured or inferred. To simplify we assign the LHS as β such that

$$\beta = (E_l E_\nu - P_{l_Z} P_{\nu_Z})$$

$$\rightarrow\ \beta + P_{l_Z} P_{\nu_Z} = E_l E_\nu,\ \text{ so } (\beta + P_{l_Z} P_{\nu_Z})^2 = E_l^2 E_\nu^2 = E_l^2 (P_{\nu_X}^2 + P_{\nu_Y}^2 + P_{\nu_Z}^2)$$

this is just a quadratic in P_{ν_Z} and manipulation gives:

$$P_{l_Z}^2 - E_l^2) P_{\nu_Z}^2 + 2\beta P_{l_Z} P_{\nu_Z} + (\beta^2 - E_l^2 (P_{\nu_X}^2 + P_{\nu_Y}^2) = 0 \tag{6.2}$$

Eqn. 6.2 is solved in the standard way i.e.

$$P_{l_Z} = \frac{-b \pm \sqrt{\Delta}}{2a} \text{where } \Delta = \mathrm{b}^2 - 4\mathrm{ac},\ \mathrm{a} = (\mathrm{P}_{\mathrm{l_Z}}^2 - \mathrm{E}_\mathrm{l}^2),\ \mathrm{b} = 2\beta \mathrm{P}_{\mathrm{l_Z}},\ \mathrm{c} = -\mathrm{E}_\mathrm{l}^2 (\mathrm{P}_{\nu_\mathrm{X}}^2 + \mathrm{P}_{\nu_\mathrm{Y}}^2) \tag{6.3}$$

to give zero, one, two solutions for P_{ν_Z} (although one solution is unlikely in practice). Typically the equation has two real solutions in around 70% of signal events, with a neutrino P_Z resolution shown in fig. 6.16, the best solution being highlighted in the shaded histogram. Fig. 6.17 is the P_Z distribution for the true neutrino, the shaded

section being for those cases where the quadratic had real roots. Note the remainder of events tend to be at the lower end of the $|P_Z|$ spectrum. In the case of no real solutions, one could choose to cut the event or make an approximation. As a major percentage of events are already lost through other cuts, it is not desirable to remove another 30%. There are several approximations one can use to keep these events. Firstly one can allow the W-boson mass to 'run', which is to say vary it within a mass window and try again to solve the quadratic. Another possibilty is to use the 'collinear approximation' (as in [55]); this assumes the charged lepton and neutrino are travelling in the same direction. As the charged lepton 4-momentum is known one can assign its P_Z to the neutrino. Alternatively one can neglect the imaginary term in the quadratic which gives rise to the complex solution (i.e. set $\Delta = 0$).

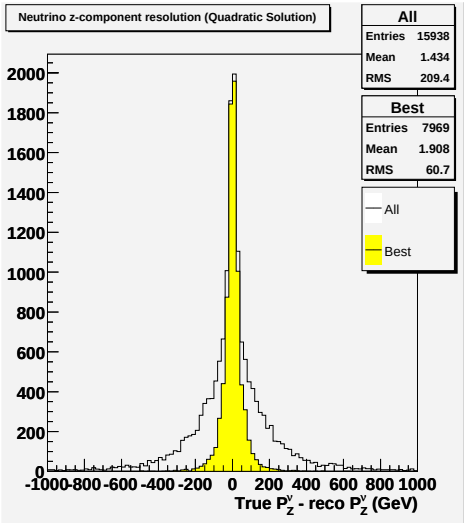

Figure 6.16: *P_Z resolution when the quadratic has real roots. Shown are all solutions and the best solution.*

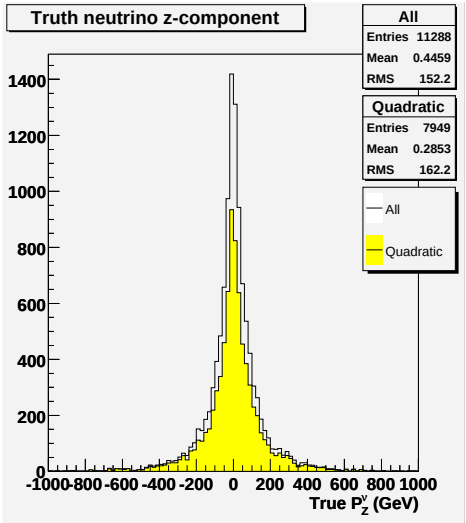

Figure 6.17: *P_Z distribution for the true neutrino. The shaded section is the best quadratic solution from fig. 6.16.*

For the remaining 30% which failed the W mass constraint method, each of these methods was tried and the results are shown in fig. 6.18. Fig. 6.18(a) shows the P_Z

resolution for the running W mass technique (The W mass is increased in steps of 1 GeV/c^2 from the pole mass up to 20 GeV/c^2 above this ($\approx$ 100 GeV/c^2) to try to make the imaginary component real), with the shaded section being the better of the two solutions. Figs. 6.18(b) and (c) show the P_Z resolution for the collinear approximation and $\Delta = 0$ respectively (there is only one solution from each of these). It can be seen that the running W mass solution is the best of these as it has a smaller RMS, particularly when the best of its two solutions is highlighted. It is successful in 60% of relevant cases (or 18% of the total events with a candidate lepton). Fig. 6.18(d) shows the P_Z distribution of the true neutrino, overlaid with the cases where the running W mass technique was successful. Just as was the case for the W mass constraint, it can be seen that the unsolvable cases have low $|P_Z|$. For this last problematic group the average $|P_Z|$ is becoming so low that it is reasonable to wonder whether it is worth simply approximating it to zero. Fig. 6.19 shows the P_Z resolution for the $\Delta = 0$, collinear approximation and $P_Z = 0$ (note as this is a resolution this is simply the true neutrino P_Z) in the remaining 12% of events. From the figure, it is clear that the $\Delta = 0$ approximation performs slightly better than setting $P_Z = 0$, with an RMS of 88 as opposed to 90. Note that the resolution is now much worse than for the P_X component in fig. 6.20 which was approximated from the missing transverse momentum.

The effect of the different leptonic W reconstruction methods can be seen in fig. 6.21, which shows the ΔR from the true W and the transverse energy ratio (here we define $\alpha = E_T^{W,reco}/E_T^{W,truth}$). The cases where the quadratic solution has real roots (fig. 6.21 a), b)), are by far the closest to the true W parameters. For the events where the running W technique is used (fig. 6.21 c), d)), there is a degradation in results. However, in this case the W mass will not be equal to the pole mass as is the case when $\Delta > 0$. The momentum of the neutrino can be rescaled (we could also rescale the trigger lepton, but the 4-momentum of this will be relatively well measured) so that the W pole mass is again achieved, to correct for inaccuracies

(mainly in the missing momentum measurements) and assumptions. Both α and ΔR to the true W are improved by this rescaling (see fig. 6.21 e), f)). For the remaining 12% of events which require the $\Delta = 0$ approximation the results are again slightly poorer (see fig. 6.22). When the rescaling is applied to these events an improvement is again seen in the ΔR separation, but it causes systematic deviation of α from 1. Whilst the RMS is improved an energy bias is introduced at the same time. Ideally we would like to keep the improved ΔR separation and better RMS of the W-boson energy resolution, whilst removing the bias introduced. Possible correlations between e.g. the W-boson energy and the scaling factor previously applied, were looked for with no success. The only solution is to apply a constant factor, f, to the entire W 4-momentum based on the ratio between the original mean and rescaled mean, i.e. $f = \frac{<\alpha_{\Delta=0,\ rescaled}>}{<\alpha_{\Delta=0}>} \approx 1.125$ This factor is actually only calculated over the central region of the distribution 0.6 - 1.0, otherwise the low-side tail tends to make the correction too large. A compromise then is shown as 'corrected' in fig. 6.22, where the majority of events are now in the close to 1.

This concludes the section on leptonic W-boson reconstruction. A clear path has been established, first solving for the neutrino P_Z using the W mass constraint, second allowing the mass to vary in the running W mass technique and finally setting the Δ term to 0. For the latter two which return a W mass off the pole mass, the 4-momentum of the neutrino is rescaled which results in a W closer in ΔR space to the true W-boson.

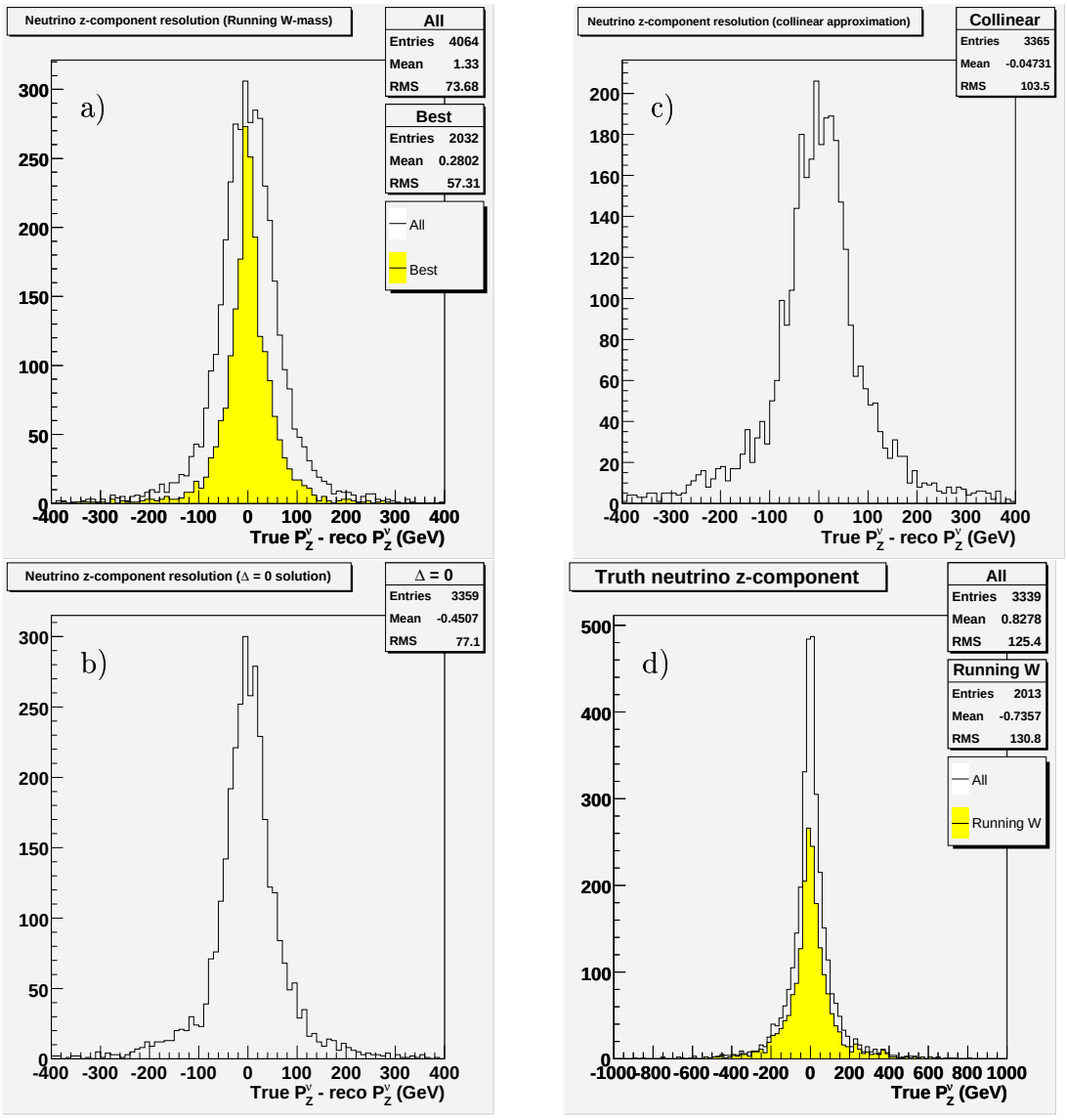

Figure 6.18: *Resolutions for the reconstructed neutrino P_Z to the true P_Z for events where the quadratic solution failed (approximately 30% of events). a) shows the ruuning W-mass technique, b) shows the collinear approximation and c) the $\Delta = 0$ approximation. One sees that the running W-mass provides the solution with the smallest RMS and this should be used preferentially. d) shows that it is only successful in $\approx 60\%$ of events, increasingly failing as the true momentum gets closer to 0.*

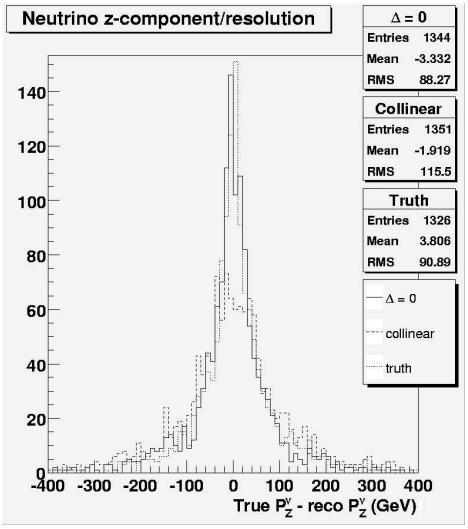

Figure 6.19: *Resolutions for the events where the quadratic and running W techniques failed*

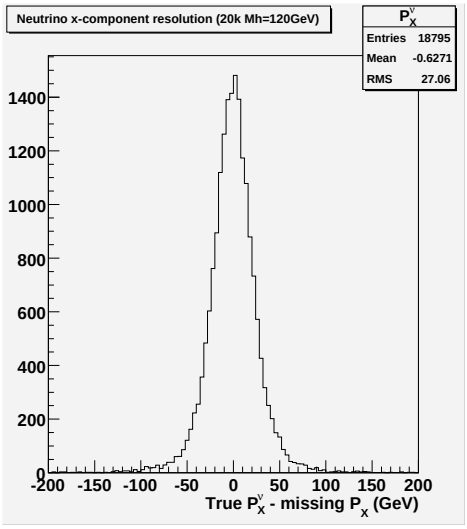

Figure 6.20: *Neutrino P_X resolution based on measured missing momentum.*

6.3.5 Hadronic W

In the decay of W-bosons to two (or more) light jets there are no quantities which are intrinsically 'unknowable' as in the previous section, but there are other uncertainties. Firstly one must identify the correct jets, which requires that they be correctly reconstructed by the jet algorithms and that they are not mis-tagged as b-jets. Assuming the correct jets are found, one has to measure the energies precisely. To do that one must find all the decay products of the decayed hadron, which is difficult due to e.g. invisible particles or out of cone effects. Due to the difficulty in identifying the correct jets, all candidates (formed from pairs of non b tagged jets) that combine to form a W candidate, within 25 GeV/c^2 of the nominal W mass are kept. Each of the these candidate Ws may then be rescaled to the pole mass, to account for the losses mentioned above and errors when determining the jet energy scale. The rescaling is done by multiplying the entire W candidate 4-momentum by a constant term. The ΔR separation and energy ratio with respect to the true W-boson are shown in fig. 6.23. One

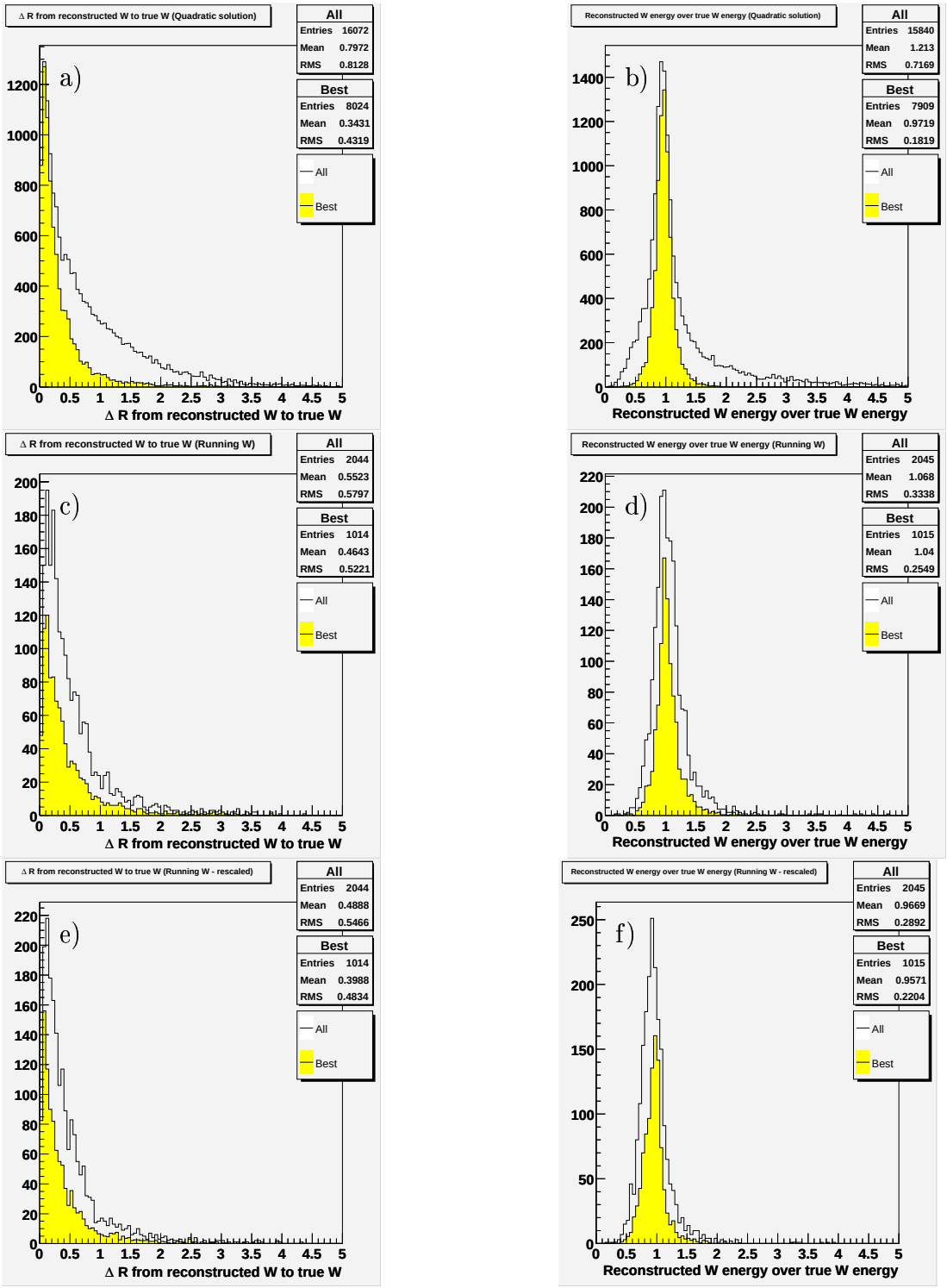

Figure 6.21: *ΔR between the reconstructed leptonic W to the true W is shown on the left and the energy ratio of the reconstructed leptonic W over the true W on the right. a) and b) are from the W mass constraint method, c) and d) are from the running W mass method, e) and f) are from the running W mass method with neutrino momentum rescaling.*

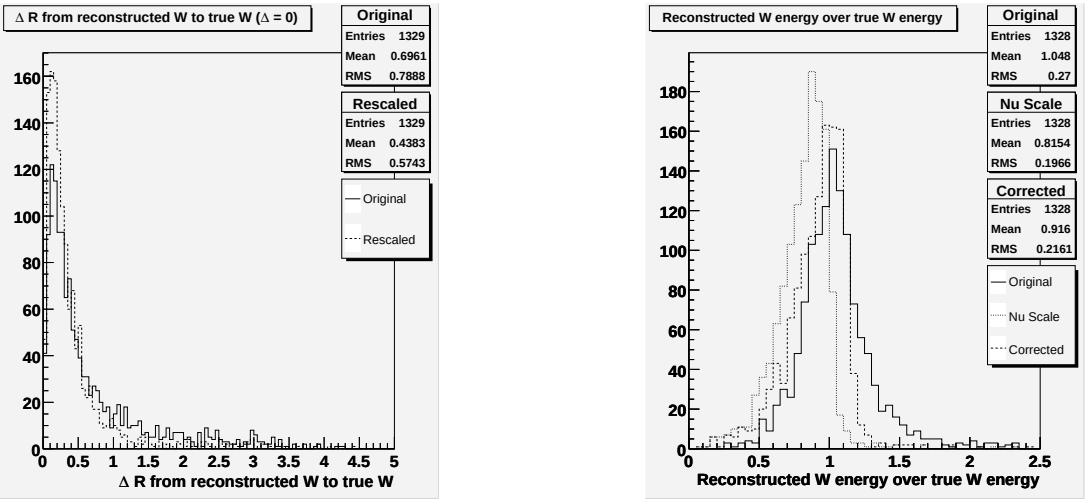

Figure 6.22: *ΔR between the reconstructed leptonic W and the true W is on the left and the energy ratio of the reconstructed leptonic W over the true W on the right for the remaining 12% events where one has set $\Delta = 0$.*

first notes that compared to the leptonic W-boson, the correct hadronic W-boson is found in a much smaller percentage of entries (see fig. 6.23 a)). This is partly because there is no equivalent of the isolated charged lepton which is readily identifiable with a high degree of purity. However also note that the number of entries is much higher as an average of 2.5 candidate W-bosons are found per event, at most one of which could be the correct one. If one only looks at the 'best' W-boson (the one closest in ΔR space to the true W-boson) one sees much improvement in the resultant ΔR and energy ratio plots, (see fig. 6.23 c)). One concludes from fig. 6.23 that the true W-boson is well reconstructed, but is often amongst combinatoric background. Fig. 6.24 shows the reconstructed mass of all light jet pairs, then of those within a 25 GeV/c^2 window of the W-boson pole mass and finally the best (i.e. closest matched) in each event which passes the window cut. One sees that a large proportion of the di-jet masses are within the region we are interested in, which means there are liable to be a number of incorrect combinations carried forward to the next stage of reconstruction. Note that the mass resolution is more or less independent of whether the jet pair is

close in ΔR space to the W or not, as a broad distribution is seen in both. This is why the rescaling above is an important step, because even when one identifies the correct jet pair the mass (and correspondingly energy) will be wrong in many cases. For the 120 GeV/c^2 Higgs boson sample, the efficiency for finding at least one jet pair within the required mass range is 83.6 %.

6.3.6 t-quarks

As previously discussed, t-quark reconstruction is vital in this channel, so that the correct b-jets can be readily assigned to the Higgs boson. At this point in the analysis, there must be at least one leptonic W-boson and one hadronic W-boson (though there may be more of either) and four b-jets. Thus there are a minimum of twelve possible $bW_{lep}\,bW_{had}$ combinations. Any combination which reconstructs both t-quark candidates within a mass window of 25 GeV/c^2 from the generated top mass of 175 GeV/c^2 is considered a 'good' combination. One now needs to decide which of these combinations is the best, in order to choose which b-jets should form the Higgs boson (note this is only relevant for candidate combinations which use different b-quarks, not for example if they only have a different leptonic W boson). Three methods were considered:

- Method 1: The 'masses' method uses the quality of the mass reconstruction by minimizing the quantity $\delta^2 = (m_{bjj} - m_t)^2 + (m_{bl\nu} - m_t)^2$
- Method 2: The 'thad pt' method chooses the combination which maximises the value of the transverse momentum of the hadronic top
- Method 3: The 'thad+tlep pt' method chooses the combination which maximises the value of the scalar sum of transverse momenta of the hadronic top and leptonic top

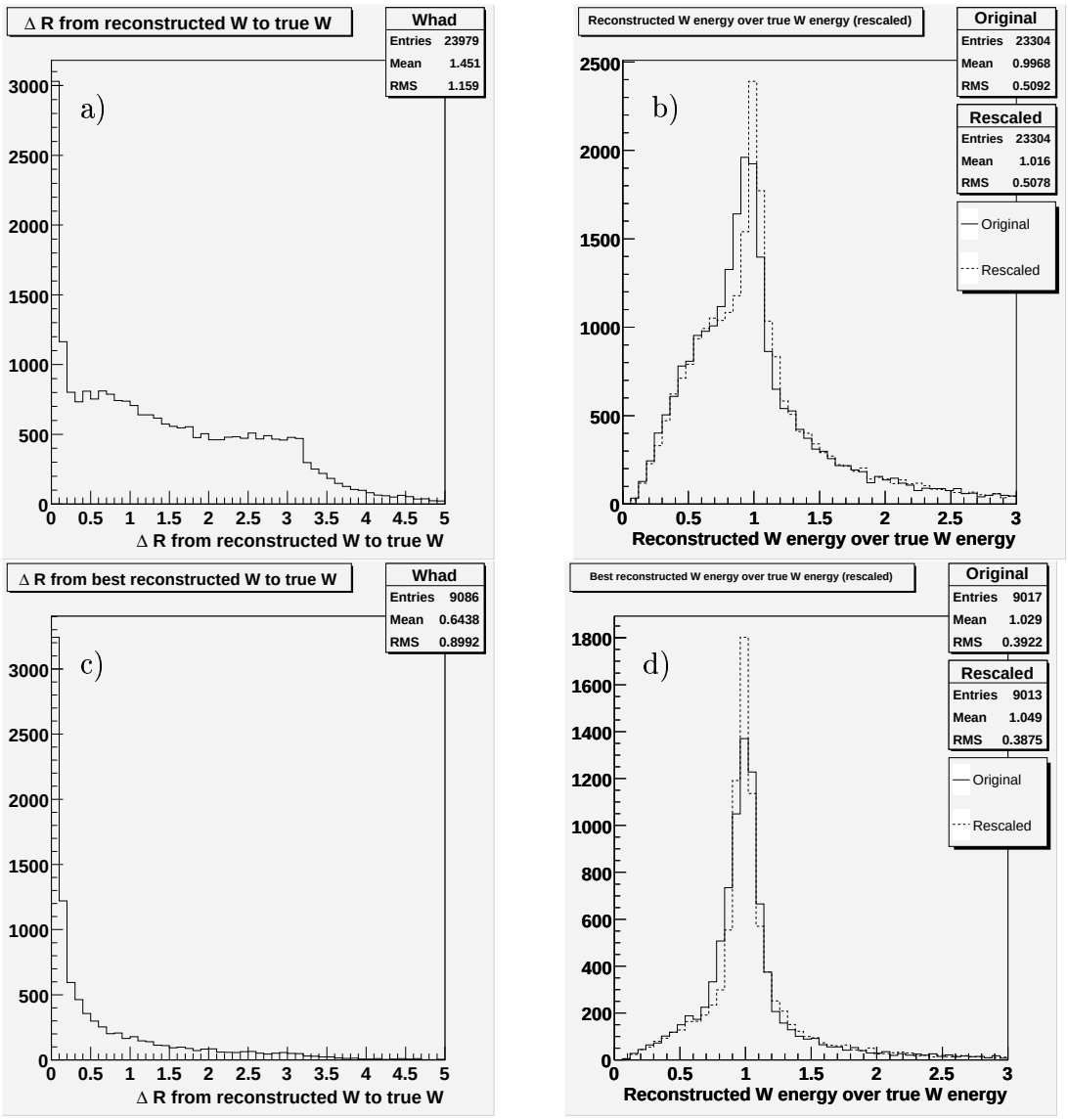

Figure 6.23: *ΔR and energy ratio of the reconstructed hadronic W candidate to the true one. c) and d), the 'best' plots, are a subset of plots a) and b) containing only the W candidate closest to the true W in ΔR in each event.*

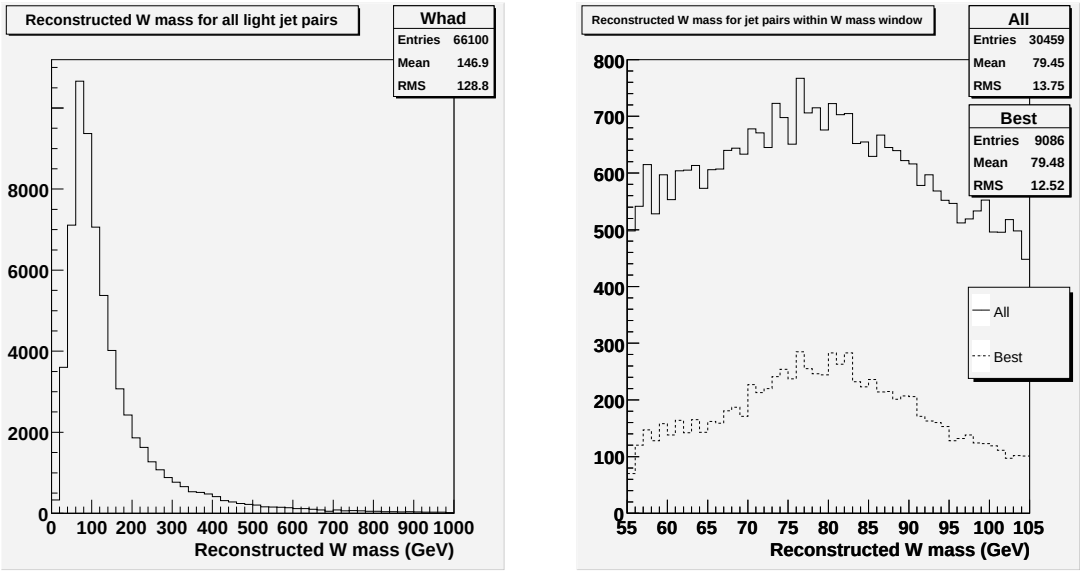

Figure 6.24: *Reconstructed mass of the hadronically decayed W-boson. The left hand side is for all light jet pairs whilst the right hand side shows only those within 25* $\mathrm{GeV/c^2}$ *of the nominal W mass. On the right the solid line is all pairs within the mass window, whilst the dashed line is the pair closest in* ΔR *space to the true W.*

The masses method has merit because in a very well measured event one would expect to get very close to the correct mass, allowing for decay width. However the event will typically not be this well measured and it is perfectly possible that a random combination will have a mass closer to the generated mass than the correct combination. The other two techniques rely on the event constituents typically being of high transverse momentum. Reference [60] suggests that the combination which has the hadronic top candidate with the highest p_T is, most likely, the correct combination. As a variation on this, we also tried selecting the combination which maximising the scalar sum of the transverse momenta of both hadronic and leptonic t-quarks.

The results, in terms of how close in ΔR space the reconstructed quarks are to the true quarks, are shown in fig. 6.25. One sees from figs. 6.25 a) and c) that method 1 is overall the poorest for reconstructing both the hadronic and leptonic t-quarks. Although it reconstructs the hadronic top better than method 3, the situation is

reversed (and to a larger degree) for the leptonic top. This is of small importance anyway as method 2 outperforms both of these. Method 2 is by far the best for reconstructing the hadronic top and is only slightly poorer than method 3 when reconstructing the leptonic top. This is particularly evident in fig. 6.25 b) (which is just the subset of fig. 6.25 showing those combinations which are reasonably well matched), which shows method 2 has a 20% advantage with respect to method 3 in terms of the selected combination being closer to the true hadronic top quark (in $0 \leq \Delta R \leq 1$). There is no corresponding drop in the number of entries when going from fig. 6.25 b) to fig. 6.25 d), although method 3 maintains its slight advantage in mean and RMS. Overall, method 2 is clearly the best and is therefore adopted for the remainder of the analysis.

This concludes the section on top quark reconstruction. Three methods were investigated for choosing the correct combination of W-bosons and b-jets. It was found that the method where the hadronic top quark's p_T is maximised, on average found the correct solution most often. The next section continues by reconstructing the Higgs boson from the remaining b-jets.

6.3.7 Higgs boson Reconstruction

After the best $t\bar{t}$ combination has been selected, the remaining two b-jets are assumed to be the Higgs decay products. In the cases where five or more b-jets were found in the event, one must first identify the best b-jet pair. The Higgs mass cannot be used as a constraint, instead the p_T of the jets is used as a discriminant. Assuming the correct jets have been assigned to the top quarks, any extra jets must be from the underlying event and should therefore be of lower p_T than the jets from the Higgs boson decay. Accordingly the two b-jets with the highest p_T are assigned to the Higgs bboson decay. Note that these events with excess b-jets are relatively rare anyway. The distribution of the invariant mass of the two Higgs candidate jets, m_{bb}, for the signal and signal

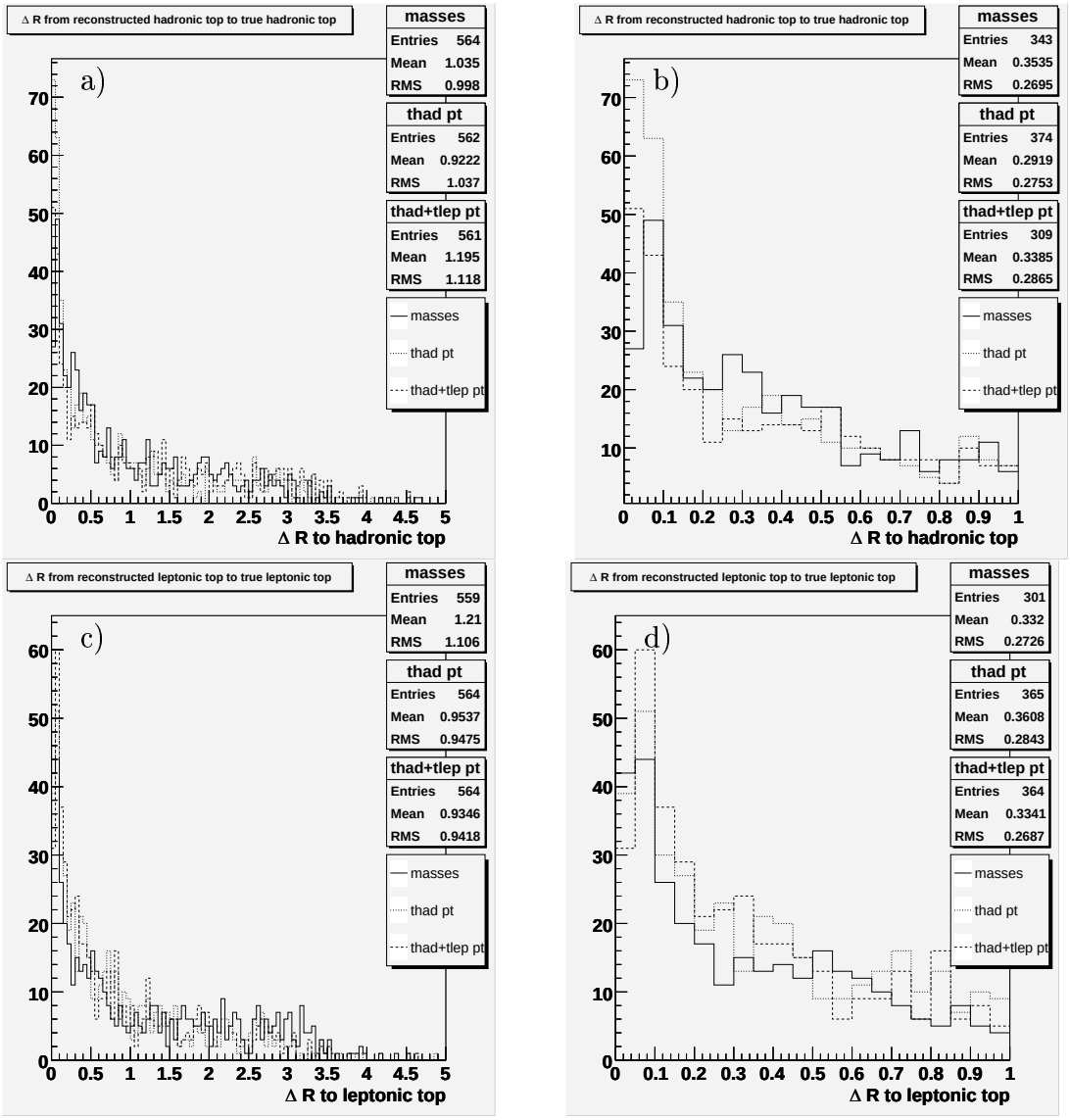

Figure 6.25: ΔR *between the reconstructed top quark and the true top quark, over the entire range on the left and the range* $0 \leq \Delta \mathrm{R} \leq 1$ *on the right, for three different methods for selecting the best combination. The upper plots, a) and b), show the results for the hadronic top and the lower, c) and d), show the results for the leptonic top.*

with background are shown in fig. 6.26 for cone and k_T jet algorithms. The results shown have been normalised for 30 fb^{-1} of data, the amount nominally expected to be collected in the first three years of data taking. The number of entries is indicative of the statistics in each sample, while the histograms themselves show expected number of events.

The results for the signal are shown in fig. 6.26 a) and b) for the cone and k_T jets respectively. Looking first at the plots as a whole one observes the invariant masses peak systematically lower than the true Higgs boson mass. This is unsurprising as in §6.2.4 it was shown that the constituent jets are systematically mis-measured usually as a result of missed energy. Whilst efforts to correct for muon spectrometer losses improved this, the energy lost from invisibles is still missing (as discussed in §6.3.3). The results show the cone results having lower peaks and means (the 120 GeV/c^2 sample seems to deviate from this, though not significantly) than the k_T results. This is exactly as expected as the k_T individual jets were closer to the parton energy in §6.2.4 as they are less subject to 'out of cone' effects. Moving across the Higgs mass range one sees the number of events falling with input mass. The two factors of falling cross-section and falling $H \rightarrow b\bar{b}$ branching ratio being the cause of this. Fig 6.26 c) and d) show the same signal results with background added.

Before the backgrounds are discussed it should be pointed out that the events shown for the $t\bar{t}jj$ background have been created with an altered light jet rejection factor. Recalling that the fast simulation rejection factor is on the order of 1 in 100 for light jets, the 'correct' run produced very low end results statistics. The histograms from this run made the background's shape hard to determine. Given that, in fast simulation, the rejection factor is essentially completely random, a modified run was created with a light jet rejection factor of 1 in 10. This produced smoother results which were then normalised to the number predicted by the original sample (with a light jet rejection of 1 in 100). Due to the high statistical error in the m_{bb} invariant masses from the events passing all event selection and reconstruction steps, the altered

run is scaled to the number of events where at least 4 b-jets were found (beyond this stage the samples follow a similar cut efficiency). Both the $t\bar{t}jj$ and irreducible $t\bar{t}b\bar{b}$ background were normalised to the same integrated luminosity (30 fb^{-1}) as the signal. Comparing the background and signal invariant mass peaks, one sees that the $t\bar{t}b\bar{b}$ background peaks at a similar value to the signal while the $t\bar{t}jj$ background peaks at a lower value. This is a reflection of the fact that for the combinations where the top quarks are reconstructed correctly, the remaining jets in the backgrounds will be softer (than the b-jets from the top or from the Higgs boson in the signal). However, even though the background is falling, it is still close enough to the search region (irrespective of choice of jet clustering algorithm) that the signal peak will be difficult to observe directly. Before the significance is calculated, a final cut is applied to select events in the Higgs mass peak region i.e. $\mathrm{m_H} - 30\mathrm{GeV/c^2} \leq \mathrm{m_{bb}} \leq \mathrm{m_H} + 30\mathrm{GeV/c^2}$.

At this point we summarise the acceptance of the cut flow throughout the whole event selection and reconstruction procedure for the cone and k_T jet algorithms in tables 6.5 and 6.6 respectively.

The final numbers of expected events and the significance are shown in tables 6.7 and 6.8, for the cone and k_T algorithms respectively. This shows the expected events for three years of data and the significance expected when using this analysis. One first observes that the results indicate a significance well below the level required for potential observation. We conclude that the integrated luminosity will need to be higher to observe this particular channel with this particular analysis. As part of a combined Higgs boson search the results still have merit, especially as the mass region searched for here is difficult for some of the 'cleaner' search channels (such as $H \to ZZ \to llll$ which would be able to observe the Higgs boson on their own. In addition, better analyses than presented here should certainly be prepared before and over the course of data taking. One result of note is that the significance is actually very similar for both jet algorithms. This was something of a surprise as

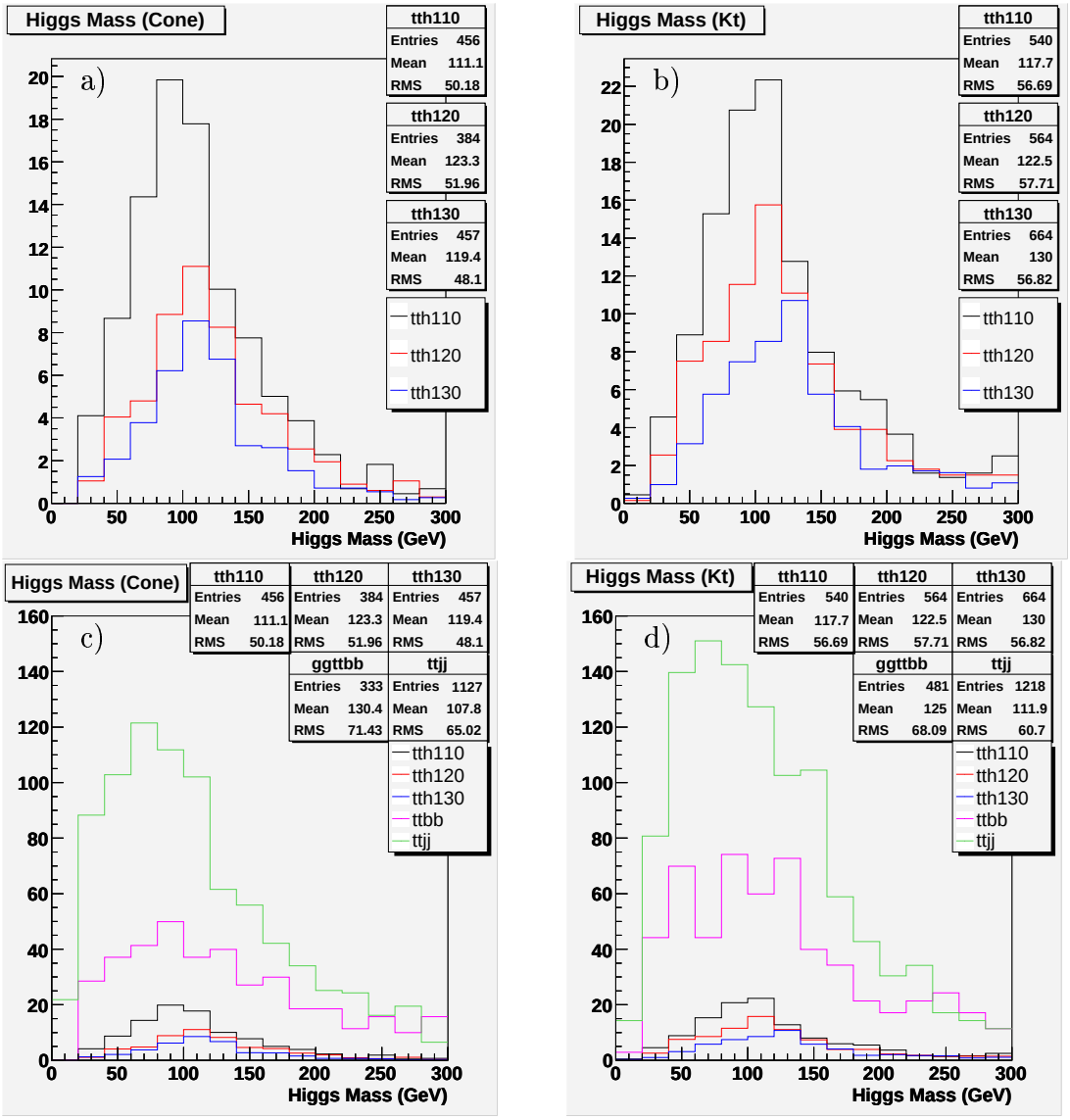

Figure 6.26: *Invariant mass of the two $b\bar{b}$ pairs assigned to the Higgs boson for the signal and background. The plots have been normalised to the expected number of events for 30 fb^{-1} of data. It can be seen that the signal events peak systematically lower than the true Higgs boson mass, more so in the cone than k_T jets. The backgrounds peak in a region similar to the signal thus making the peaks difficult to observe.*

Cut	$t\bar{t}H(110)$	$t\bar{t}H(120)$	$t\bar{t}H(130)$	$t\bar{t}b\bar{b}$	$t\bar{t}jj$
$N_{LEP} \geq 1$	59.63%	60.16%	60.80%	61.55%	55.0%
$N_{JET} \geq 6$	32.11%	32.78%	33.24%	24.45%	19.72%
$N_{BJET} \geq 4$	3.24%	3.86%	4.15%	1.46%	0.033%
$N_{WLEP} \geq 1$	3.24%	3.86%	4.15%	1.46%	0.033%
$N_{WHAD} \geq 1$	2.56%	3.05%	3.27%	1.13%	0.026%
$N_{t\bar{t}} \geq 1$	1.54%	1.83%	1.96%	0.60%	0.016%
m_{bb} window	1.11%	0.095%	1.06%	0.16%	0.006%

Table 6.5: *Event selection efficiencies for signal and background at each stage of the analysis using the cone jet algorithm. Here N_{LEP} is the no. of isolated leptons as defined in table. 6.3. N_{JET} and N_{BJET} are those jets included by the kinematic cuts defined in §6.3.2. N_{WLEP}, N_{WHAD}, $N_{t\bar{t}}$, m_{bb} are the efficiences for finding the leptonic W (100% with approximations), hadronic W, top quarks and Higgs boson within their respective mass window.*

the k_T algorithm has always held something of an advantage at each step of the analysis (all results tending to be $\approx 25\%$ higher, which would lead to an increase of around 10% in significance). This advantage appears lost in the end result, possibly because the scaling used when using a false light jet rejection factor affects the jet algorithms differently (The final cone numbers are scaled down by 19, whilst the k_T only by 16.5, to account for this. This may be because the k_T algorithm has a higher jet multiplicity and therefore the effect of applying an incorrect mis-tag rate will be more pronounced). We should remember however, that the k_T algorithm produced better centred energy ratio plots for the jets and should therefore predict more accurate masses.

Cut	$t\bar{t}H(110)$	$t\bar{t}H(120)$	$t\bar{t}H(130)$	$t\bar{t}b\bar{b}$	$t\bar{t}jj$
$N_{LEP} \geq 1$	59.63%	60.16%	60.80%	61.55%	55.0%
$N_{JET} \geq 6$	39.65%	40.17%	41.92%	30.48%	20.81%
$N_{BJET} \geq 4$	4.8%	5.0%	5.1%	1.90%	0.043%
$N_{WLEP} \geq 1$	4.8%	5.0%	5.1%	1.90%	0.043%
$N_{WHAD} \geq 1$	3.98%	4.15%	4.23%	1.48%	0.033%
$N_{t\bar{t}} \geq 1$	2.3%	2.43%	2.53%	0.88%	0.018%
m_{bb} window	1.3%	1.3%	1.47%	0.28%	0.007%

Table 6.6: *Event selection efficiencies for signal and background at each stage of the analysis using the k_T jet algorithm. Here N_{LEP} is the no. of isolated leptons as defined in table. 6.3. N_{JET} and N_{BJET} are those jets included by the kinematic cuts defined in §6.3.2. N_{WLEP}, N_{WHAD}, $N_{t\bar{t}}$, m_{bb} are the efficiences for finding the leptonic W (100% with approximations), hadronic W, top quarks and Higgs boson within their respective mass window.*

Higgs Mass	Signal events	$t\bar{t}b\bar{b}$ events	$t\bar{t}j\bar{j}$ events	B_{TOT}	$\sigma_{SIG} = \frac{S}{\sqrt{B_{TOT}}}$
110 GeV	48	129	276	405	2.4
120 GeV	27	113	230	343	1.5
130 GeV	18	104	220	334	1.0

Table 6.7: *Event yield and significance for three Higgs masses for 30 fb^{-1} of data using the cone algorithm, after all cuts (see table 6.6). The signal and $t\bar{t}b\bar{b}$ background are calculated to leading order, whilst the $t\bar{t}b\bar{b}$ background is calculated at next-to-leading order, however no K-factors are used.*

Higgs Mass	Signal events	$t\bar{t}b\bar{b}$ events	$t\bar{t}j\bar{j}$ events	B_{TOT}	$\sigma_{SIG} = \frac{S}{\sqrt{B_{TOT}}}$
110 GeV	56	207	372	579	2.4
120 GeV	38	198	359	557	1.6
130 GeV	25	187	334	521	1.1

Table 6.8: *Event yield and significance for three Higgs masses for 30 fb^{-1} of data using the k_T algorithm, after all cuts (see table 6.6). The signal and $t\bar{t}b\bar{b}$ background are to leading order, whilst the $t\bar{t}b\bar{b}$ background is at next-to-leading order, however no K-factors are used.*

6.3.8 Systematics

Several systematic effects were investigated. Specifically these concern trigger thresholds, input masses and mass windows. The first of these is very important as triggers are always subject to possible change, as experimental needs are balanced against computational capabilities. Usually this is in the form of raising trigger thresholds, which has already happened once for the triggers used for this channel. The trigger requires a single isolated energetic lepton ($p_T \geq$ 20 GeV/c muon or $p_T \geq$ 25 GeV/c electron) within the central region ($|\eta| < 2.5$). The effect of increasing the transverse momentum requirement by 5 and 10 GeV/c for each lepton flavour was investigated. This is known to be a steeply falling quantity from fig. 6.2(a). The combined effect of raising each threshold by 5 GeV/c ($p_T \geq$ 25 GeV/c muon or $p_T \geq$ 30 GeV/c electron) causes around 9% of signal events to be lost. The number appears similar for the $t\bar{t}jj$ and around 12% for the $t\bar{t}b\bar{b}$ background. As the $t\bar{t}jj$ is by far the dominant background the significance is reduced by approximately 5%. If the thresholds were raised by 10 GeV/c, the levels lost increase proportionally to 20% and the significance falls by 10% from the current values. Clearly increasing trigger thresholds would not be a sensible intentional cut and if forced by experimental restictions will be detrimental to this channel.

The input mass refers to the numbers for the pole masses of the W-boson and t-quark. It should be checked that when one looks for di-jet or tri-jet combinations at these numbers, one is indeed finding the correct object and not an artifact. One can search for example for a W-boson of 75 or 85 GeV/c^2 and a t-quark of 165 or 185 GeV/c^2. When one then looks at the eventual Higgs boson cases one sees that in general several events are lost from each sample. This indicates real objects are found at the correct mass. However the fact that the effect is relatively small (on the order of a few percent), suggests the analysis is not strongly dependent on very precise knowledge of the pole mass.

The most obvious mass window one might vary is that around the final Higgs mass, chosen initially as ± 30 GeV/c^2. It was found that increasing the window improved significance and decreasing it worsened significance. However, for a 10 GeV/c^2 alteration i.e. $30 \rightarrow 20$ or 40 GeV/c^2, the improvement for the larger window was negligible, whereas the smaller window lost 10% of the significance. Thus 30 GeV/c^2 seems an adequate choice to isolate the desired region as much as possible without overly impacting on significance. Along similar lines, we investigated varying the window around the pole masses of the other particles in the event (t-quarks and W-bosons). The results are shown in table 6.9. One sees that narrowing the mass windows causes a drop in significance and is thus a poorer choice. Increasing the windows does slightly increase the significance and so is on the face of it a potential improvement. However the increase is somewhat marginal and loosening requirements may allow some unconsidered backgrounds to enter the frame. For instance, the W+jets background has a cross-section many times that of even $t\bar{t}$, but was not simulated because it should be very efficiently rejected. In part this is achieved by light jet rejection, as four mis-tagged jets are required, but mass reconstruction would also play a part. Additionally, the Higgs mass peak would be expected to broaden, as more incorrect pairings are found making the exact mass more difficult to measure.

Mass	Orig	$W \rightarrow 15$ GeV	$W \rightarrow 35$ GeV	Top$\rightarrow$15 GeV	Top$\rightarrow$35 GeV
110 GeV	2.4	2.1	2.6	2.0	2.5
120 GeV	1.6	1.4	1.7	1.4	1.7
130 GeV	1.1	0.9	1.2	1.0	1.2

Table 6.9: *Systematic effect of mass windows on significance for three Higgs masses using the k_T algorithm. The original windows are 25* GeV/c^2 *for both the hadronic W-boson and the t-quarks*

Another systematic effect which should be considered is b-jet tagging, because it is very important in signal acceptance and background rejection. The rule of thumb numbers used in fast simulation are that 60% b-jet tagging efficiency can be achieved with a light jet rejection factor of 100. The numbers for the fully simulated samples should be of this order, but will depend on other factors (such as p_T) as real taggers are used. Because the probability of finding four b-jets scales as a power of four, very small increases would have a large effect on yield. Increasing the b-jet efficiency from 0.6 to 0.65 for example, should increase signal throughput by over 30%. Alternatively doubling light jet rejection should reduce the dominant background to a quarter of the size indicated. It is possible both of these scenarios (though not simultaneously) will be achievable by the time data runs begin. One final issue is that the (dominant) $t\bar{t}jj$ background is generated at Next to Leading Order (NLO), whilst the signal and semi-irreducible $t\bar{t}b\bar{b}$ background are only LO. This is simply because no NLO generators were available at the time. As an alternative, one can calculate the K-factor - the ratio of the NLO cross-section to the leading order cross-section. One can then multiply the expected event total by this number, to get an approximate value that would be achieved with a real NLO generator. For the signal at LHC energies the cross-section variation with mass is shown in fig. 6.27 a) and with renormalisation scale, μ, in fig. 6.27 b) [61]. In the central region $\mu = \mu_0$, where $\mu_0 = (2m_t + m_H)/2$

was the scale used in generation, the k-factor is approximately 1.2. Even if one also assumes this value for the $t\bar{t}b\bar{b}$ background (bearing in mind it is only approximately one third of the total background, $\sqrt{B_{TOT}}$ only increases by a few %), one expects an increase in significance of close to 20%.

6.3.9 Comparison with other studies

In the ATLAS experiment, the $t\bar{t}H, H \rightarrow b\bar{b}$ channel was analysed for the physics TDR [39], sec 19.2.4.3. For a 120 GeV/c^2 Higgs boson that study expected 40 signal and 127 background events for an integrated luminosity of 30 fb^{-1}. The significance was 3.6, more than twice the number in the present study. Some of this was explained when the same study was carried out with new simulated data [55]. Differences there were found to be from new parton distribution functions (PDF's) and the more accurate matrix element decription of the $t\bar{t}b\bar{b}$ background. Respectively, this resulted in lower signal cross-sections and higher jet multiplicities/energies in the $t\bar{t}b\bar{b}$ background. Additionally, trigger thresholds were lower than for later studies. When one compares the present study with the 'TDR-like' study in [55] one finds the signal prediction is broadly as predicted in the present study, as is the $t\bar{t}b\bar{b}$ background. However the number of $t\bar{t}jj$ events is radically different - as much as 5 times higher in the present study. There are several reasons for this. Firstly the cross-section for $t\bar{t}jj$ used in the present study is around 750 pb as opposed to 490 pb (this is the most pessimistic scenario at NLO). Secondly, because matrix element generators produce higher p_T jets, more events will pass kinematic cuts and in addition the invariant mass of a '$b\bar{b}$' pair will be larger and so closer to the Higgs mass. Finally the number of events with 4 b-jets is approximately 2.5-3 times higher, because the matrix element generator produces higher average jet multiplicities and as stated above they tend to be harder.

Results compared to the 'TDR-like' study in [55] are therefore also poorer though

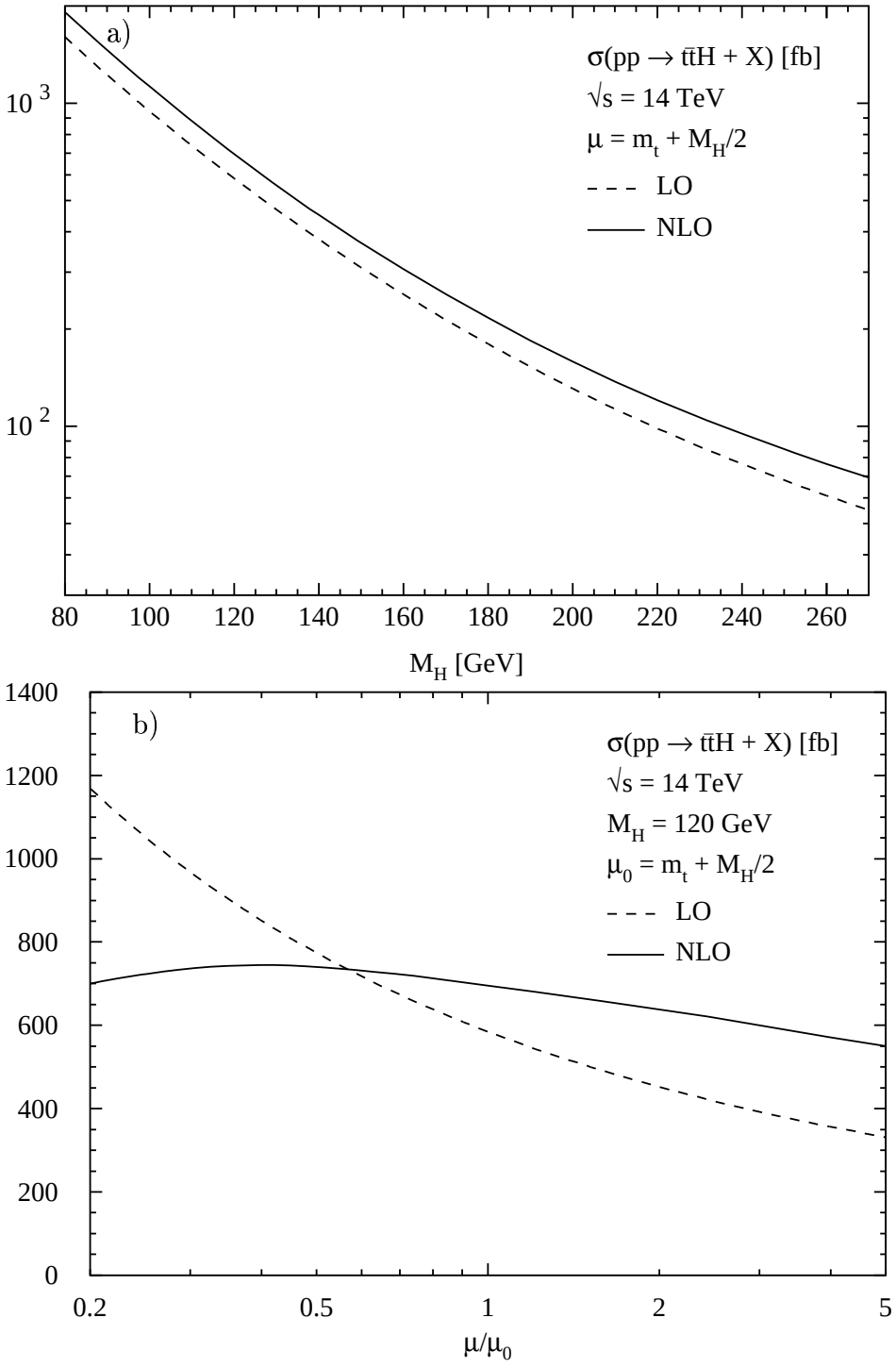

Figure 6.27: *Higgs mass and renormalisation scale dependence of the $t\bar{t}h$ cross-section for leading and next to leading order at the LHC. [61]*

not to the same degree (for a 120 GeV/c^2 Higgs boson, a significance of 1.5 as opposed to 2.0). The analysis in [55] also employed a sophisticated likelihood analysis to improve the jet pairing (reducing signal combinatorics) and remove background. For a 120 GeV/c^2 Higgs boson, a significance of 2.9 was found, again nearly twice the number in the present study and this does not include any K-factor for the signal which increases the significance further. Whether the values in [55] can be reached will depend on the quality of the real b-jet tagging, given the larger than anticipated effect of the $t\bar{t}jj$ background.

The most recent calculations for the other LHC general purpose detector, CMS, were also compared [62]. For 60 fb^{-1} the significance is 1.6 for each lepton flavour, so is about the same as the present study. However the older PDF's were used for the signal and a different (leading order) matrix element generator for the $t\bar{t}$+jets background, which leads to a cross-section half the (somewhat conservative) value used in the present study. CMS will in general find the channel more challenging than ATLAS as the same b-tagging rate cannot be achieved for an equivalent light jet rejection.

Chapter 7

Conclusion

The aim of this work was to study reconstruction of the full GEANT4 simulation of the $t\bar{t}H, H \to b\bar{b}$ Higgs boson search channel. In particular comparison of the cone and k_T jet algorithms and the effect of next-to-leading (NLO) generation of the $t\bar{t}jj$ were investigated. The conclusion for the first of these aims is that the k_T algorithm tends to find higher jet multiplicity and better energy resolution, but that this may not necessarily yield a higher significance.

The NLO simulation of the reducible $t\bar{t}jj$ has led to a change of thinking on this channel. It had been thought that the semi-irreducible $t\bar{t}b\bar{b}$ would dominate, but the higher cross-section than formerly predicted (≈ 750 pb compared to 500 pb), coupled with the generally higher energy jets one gets from matrix element generators (as opposed to parton showering generators) means that the $t\bar{t}jj$ background is now the largest. Effective b-jet tagging and light jet rejection will thus be even more important than previously thought.

There is some difficulty in achieving good energy resolution on fully simulated b-jets. This is largely a physics, not a detector effect, because the reconstructed and truth jets show good agreement. Attempts were made to correct for energy lost in the semi-leptonic decay of b-jets, with some success. However, jet resolutions are still poorer than those from fast simulation corrections, which at present seem optimistic.

Nevertheless, at some point physics effects from hadronisation place a final limit on mass resolution.

The final significance for 30 fb^{-1} of data is poorer than previously anticipated, the changes in background estimation being largely responsible for this. Because the mass resolution is so smeared, the channel will be an exercise in counting and good knowledge of background cross-sections will be vital. Jet tagging provides the final limitation on the channel and viability depends greatly on whether light jet rejection can be improved. Nevertheless, the channel should form a vital part of the ATLAS search for a low mass Higgs boson.

References

[1] S.Glashow, Nucl. Phys. **22**, 579 (1961).

[2] S.Weinberg, Phys. Rev. Lett. **19**, 1264 (1967).

[3] A.Salam, in "Elementary Particle Theory", W. Svartholm, Almquist and Wiksell, Stockholm, 1968.

[4] H.D.Politzer, Phys. Rev. Lett. **30**, 1346 (1973).

[5] D.J.Gross and F.E.Waltzed, Phys. Rev. Lett. **30**, 1343 (1973).

[6] D. Decamp *et al.*, Phys. Lett. **B235**, 399 (1990).

[7] B. Adeva *et al.*, Phys. Lett. **B275**, (1992).

[8] W.-M. Yao *et al.*, J.Phys. G **33**, (2006).

[9] P.W.Higgs, Phys. Rev. Lett. **13**, 508 (1964).

[10] F.Englert and R.Brout, Phys. Rev. Lett. **13**, 321 (1964).

[11] G. W. E.Gross and B.A.Kniehl, Z.Phys. **C63**, 417 (1994).

[12] U.Egede, *The search for the Standard Model Higgs boson at the LHC and electron identification using transition radiation in the ATLAS tracker*, PhD thesis, Lund University, 1998.

[13] M.Sapinski, Ph.D. thesis, Academy of Mining and Metallurgy Krakow, 2001.

[14] C.B.W.Lee and H.B.Thacker, Phys. Rev. **D16**, 1519 (1977).

[15] L. G.P.N.Cabibbo and R.Petronzio, Nucl. Phys. **B158**, 295 (1979).

[16] G.Altarelli and G.Isidori, Phys. Rev. **B337**, 141 (1994).

[17] M.J.G.Veltman, Acta Phys. Polon. **B8**, 475 (1977).

[18] CDF Collaboration, prelim., 2007, cDF note 8665.

[19] Tevatron ElectroWeak Working Group, TEVEWWG/2007-01, 2007, hep-ex/0703034v1.

[20] R.St. Denis, *On the brink of revelation and revolution: Electroweak symmetry breaking in 2008/2009*, GLAS-PPE/2007-05, 2007.

[21] LEP ElectroWeak Working Group, Winter 2007 Update, http://lepewwg.web.cern.ch/LEPEWWG/.

[22] R. Barate *et al.*, Phys. Lett. **B565**, 61 (2003), hep-ex/0306033.

[23] A.Heister *et al.*, Phys. Lett. **B526**, 191 (2002).

[24] TeV4LHC Higgs Group , http://maltoni.home.cern.ch/maltoni/TeV4LHC/SM.html.

[25] S.Asai *et al.*, *Prospects for the Search for the Standard Model Higgs Boson in ATLAS using Vector Boson Fusion*, SN-ATLAS-2003-024, 2004.

[26] S. Weinberg, Phys. Rev. **D13**, 974 (1976).

[27] S. Weinberg, Phys. Rev. **D19**, 1277 (1979).

[28] L. Susskind, Phys. Rev. **D20**, 2619 (1979).

[29] J. Wess and B. Zumino, Nucl. Phys. **B70**, 39 (1974).

[30] J. Wess and J. Bagger, *Supersymmetry and supergravity*, Princeton, USA:Univ. Press, 1992.

[31] R. C.D.Froggatt and I.G.Knowles, Nucl. Phys. **B386**, (1992), 63.

[32] LHC Collaboration, CERN/AC/95-05 (1995).

[33] ATLAS Collaboration, CERN-LHCC-94-43 (1994).

[34] CMS Collaboration, CERN/LHCC/94-38 (1994).

[35] LHCb Collaboration, CERN/LHCC/98-04 (1998).

[36] ALICE Collaboration, CERN/LHCC/95-71 (1995).

[37] LEP ElectroWeak Working Group, LEPEWWG/2005-01, hep-ex/-511027.

[38] F. Carminati *et al.*, *ALICE: Physics Performance Report*, http://stacks.iop.org/JPhysG/30/1517, 2004.

[39] ATLAS Collaboration, CERN-LHCC-2003-022 (2003).

[40] C. J. S. Damerell, Nucl. Instr. and Meth. **A501**, 308 (2003).

[41] ATLAS Collaboration, CERN-LHCC-98-14 (1998).

[42] ATLAS Collaboration, CERN/LHCC 99-14 (1999).

[43] https://twiki.cern.ch/twiki/bin/view/Atlas/InDetGeometryVersions.

[44] S.Agostinelli *et al.*, Nucl. Instr. and Meth. **A506**, 250 (2003).

[45] ATLAS Collaboration, CERN-LHCC-2005-22 (2005).

[46] E. Richter-Was *et al.*, *ATLFAST 2.0 A fast simulation package for ATLAS*, ATL-PHYS-98-131, 1998.

[47] http://www.hep.ucl.ac.uk/atlas/atlfast/.

[48] Comp. Phys. Comm. **153/1**, 85 (2003).

[49] https://twiki.cern.ch/twiki/bin/view/Atlas/Eventview.

[50] CDF Collaboration, Phys. Rev. Lett. **D72**, (2005).

[51] T. Sjöstrand *et al.*, Comp. Phys. Comm. 135 (2001) 238 (LU TP 00-30, hep-ph/0010017).

[52] B. Kersevan and E. Richter-Was, Arxiv preprint hep-ph/0405247 (2004).

[53] S. Frixione and B. Webber, JHEP **0206**, (2002), hep-ph/0204244.

[54] P. N. S. Frixione and B. Webber, JHEP **0308**, (2003), hep-ph/0305252.

[55] J. Cammin, *Study of a light standard model Higgs boson in the t anti-t H0 channel with ATLAS at LHC and decay mode independent searches for neutral Higgs bosons with OPAL at LEP*, BONN-IR-2004-06.

[56] https://twiki.cern.ch/twiki/bin/view/Atlas/ElectronGamma.

[57] https://twiki.cern.ch/twiki/bin/view/Atlas/ElectronGammaSoftElectronID.

[58] https://twiki.cern.ch/twiki/bin/view/Atlas/ElectronGammaIsEM.

[59] S. Corread *et al.*, *B-tagging with DC1 data*, ATL-PHYS-2004-006.

[60] J. A.-I.Etienvre, J.-P.Meyer, ATL-PHYS-INT-2005-002 (2005).

[61] W.Beenakker *et al.*, Phys. Rev. Lett. **87**, (2001).

[62] S.Cucciarelli *et al.*, *Search for* $H \to b\bar{b}$ *in association with a* $t\bar{t}$ *pair at CMS*, CMS NOTE 2006/119, 2006.